Computational and Experimental Investigations into the Factors Influencing Hole Mobility in Tuneable Small-Molecule Organic Hole Transporters

Miriam Helen Fsadni

A Thesis Submitted to

Newcastle University

School of Natural and Environmental Sciences

For the degree of Doctor of Philosophy

March 2024

Abstract

Perovskite solar cells (PSC) are widening the scope of photovoltaics (PVs) to applications beyond the effective capabilities of conventional silicon-based PVs. In these devices the organic hole transport material (HTM) plays a major role in controlling the overall performance and cost of PSCs. Charge recombination at the HTM/perovskite interface remains a challenge, as is the cost of producing standard HTMs, such as spiro-OMeTAD, limiting the viability of these devices. Recently, inexpensive tuneable small-molecule organic HTMs have been developed using condensation chemistry, some of which show promising charge transport properties. A better understanding of the factors governing mobility in these materials could help us move away from the conventional trial-and-error approach and enable us to design HTMs with a higher mobility.

In this thesis I explored the properties of small molecule organic HTMs relevant to charge transport. In amorphous (disordered) systems such as these, where charges are localised on energetically discrete sites (molecules), charge transport has been conceptualised as a hopping process which may be described by Miller-Abrahams and Marcus rate equations. Initial quantum mechanics calculations on single molecules revealed that the best charge transport properties were exhibited by HTMs with high dipole moments. This is rather surprising, as correlated energetic disorder has been shown to scale with the dipole moment in amorphous materials and quench mobility. This led us to look further into the effects of the size and ordering of molecular dipoles on mobility using an in-house kinetic Monte Carlo code. While it has been suggested that higher dipole moments might drive favourable self-assembly during film formation and reduce the width of energetic disorder, our simulations show that mobility is rapidly quenched even at low levels of disorder. We find that increasing the dipole moment reduces the number of energetically available hopping sites, resulting in inefficient charge percolation through the film.

High levels of global order are unlikely to be achieved in solution processed thin films. However, crystal structures of HTMs reveal closely packed dimers which orient antiferroelectrically in some cases. The presence of these stable supramolecules, with a zero-dipole moment, might reduce the overall energetic disorder in an otherwise disordered film. Molecular dynamics simulations show that our systems based on high performing molecules have a greater proportion of these dimers and in kMC simulations the mobility increases sharply with the population of zero dipole dimers.

While these results suggest that it may be beneficial to design molecules with a low dipole moment, polar HTMs may be better at binding to and passivating the perovskite layer, which would increase the power conversion efficiency (PCE) and long-term stability of PSCs. In addition, it has been shown that suitable alignment of dipoles generates a giant surface potential (GSP) across organic semiconductor films, which could be exploited to enhance charge extraction and transport. Based on

our insights, we set out to control disorder in high dipole HTMs via dimer formation by developing and synthesising a series of HTMs with different H-bonding capabilities. These consisted of both symmetric and asymmetric secondary and tertiary amides, as well as a urea compound. The intermolecular interactions and charge transport properties of these molecules was investigated. Results show that molecules with highly available H-bonding sites readily form H-bonded dimers in the crystal structure and in solution, by proton NMR spectroscopy. These molecules also show favourable charge transport properties when compared to the methylated derivative which is unable to dimerise via intermolecular H-bonding.

Our results indicate that it may be possible to use bonding to tune the width of the energetic disorder in high dipole amorphous HTM films. This could be achieved by the formation of short-range ordered domains with quenched dipoles, made up of closely packed favourably oriented monomers, and to a lesser extent through better ordering of dipoles in the film as a whole.

Acknowledgements

Firstly, I would like to thank my supervisors Thomas Penfold, Pablo Docampo and Elizabeth Gibson for the opportunity to carry out this work, and from whom I have learnt so much. The encouragement, support, and guidance they provided throughout my PhD have been invaluable to me.

My sincere gratitude goes to Thomas Pope, Dumitru Sirbu, Benjamin Vella and Eman Alkhudhayr for all their work during our enjoyable collaborations.

A special thanks goes to Penfold group members past and present, for the chats, company and all the help during these last four years: Julien Eng, Thomas Pope, Yvelin Giret, Conor Rankine, Tudur David, Clelia Middleton, Shawana Ahmad, Luke Watson, Sneha Verma, Marwah Madkahli, Yang Cao and Josh Littlefair. Julien, Tom and Conor, thanks for your unwavering patience with all my questions, and for all the conversations and coffee breaks.

I would also like to thank members of the Energy Materials group past and present: Susana Iglesias Porras, Natalie Flores Diaz, Amy Nield, Ella Fidment, Abigail Seddon, Lawrence Bruce, Mashaer Alharbi, Abdulaziz Aljeldah, Matar Almutari, Linah Alqahtani, Iacopo Benesperi, David Bradford, Cathal Burns, Heather Flint, Richard James, Rishan Kappattu, Joshua Karlsson, Timo Keller, Harvey Morritt, Bening Muhammad, Matthew Royle, Kezia Sasitharan, Zhongjin Shen, Giovanni Spinelli. Susana, Natalie, Amy, Ella, Abigail, and Lawrence, thank you for creating a nice atmosphere in the lab, and for making our lunches and travel so much fun.

Furthermore, I would like to thank past members of the perovskite group, including Dumitru Sirbu, Nathan Hill, Ivan Shmarov, Naseem Alsaif, and members of the Docampo and Cooke groups at Glasgow University, especially Marcin Giza, Namrata Pant and Michele Cariello, for showing me the ropes and being so kind and welcoming at the start of my PhD, and during my stay in Glasgow. Thanks also to Valentina Gauci for the laughter, the dinners, and the sanity checks. I am so glad our paths crossed somehow.

I would also like to extend my gratitude to Cristina Navarro and James Dawson for their encouragement and feedback during or panel meetings, to Owen Woodford for being so helpful with my last-minute experiments, to Micheal Hall for always being available for advice, and to Carolyn Hunter, Laura McCorkindale and Niall Straughan who have always been ready to provide any help they could when I needed chemicals and equipment.

To my two oldest friends Anna and Ada, thank you for being my biggest cheerleaders; sharing in my joys, carrying me through the hard times and never letting me lose sight of myself or the bigger picture. You mean more to me than words can express. Last but by no means least, I would like to thank my family, and especially my partner Mats who patiently walked by my side and never stopped believing in me.

To my family

Declaration

This thesis is submitted to Newcastle University in support of my application for the degree of Doctor of Philosophy. It has been composed by myself, and contains no material that has been accepted for the award of any other qualification at any other Institution or University. The work described in this thesis was carried out between September 2019 and March 2024, at Newcastle University (School of Chemistry, Bedson Building, Newcastle University, NE1 7RU) and at the University of Glasgow (School of Chemistry, Joseph Black Building, Glasgow G12 8QQ). The work presented was carried out by me, except where due reference has been made in the text, and below.

Miriam Helen Fsadni, March 2024

Kinetic Monte Carlo and Classical Molecular Dynamics experiments were carried out in collaboration with Dr Thomas Pope (Newcastle University) and Dr Yvelin Giret (Université de Lille). Optoelectronic and electrochemical experiments were performed in collaboration with Benjamin Vella (University of Glasgow). High resolution atomic mass spectroscopy (HRAM) was performed by the EPSRC UK National Mass Spectrometry Facility (NMSF) at Swansea University. X-ray crystallography and structure elucidation of TPA-BT was performed by Dr Paul Waddell at Newcastle University. Figures **6a-c** in *Chapter 3*, and **13**-**18** in *Chapter 4* were generated by Dr Thomas Pope.

Part of this work has been published:

- T. Pope, Y. Giret, M. Fsadni, P. Docampo, C. Groves and T. Penfold, *Org. Electron.*, 2023, **115**, 106760.
- E. A. A. Alkhudhayr, D. Sirbu, M. Fsadni, B. Vella, B. T. Muhammad, P. Waddell, M. R. Probert, T. J. Penfold, T. Hallam, E. A. Gibson and P. Docampo, *ACS Appl. Energy Mater.*, 2023, **6**, 22, 11573.
- B. Vella, M. Fsadni, T. Pope, M. Giza, F. J. Angus, I. Shmarov, P. L. Lalaguna, M. Cariello, C. Wilson, M. Kadodwala, T. J. Penfold, P. Docampo and G. Cooke, *J. Mater. Chem. A*, 2024 (*accepted*).

Other published work:

- N.S. Hill, M.V. Cowley, N. Gluck, M. H. Fsadni, W. Clarke, Y. Hu, M. J. Wolf, N. Healy, M. Freitag, T. J. Penfold, G. Richardson, A. B. Walker, P. J. Cameron and P. Docampo, *Adv. Mater.*, 2023, **35**, 2302146.
- N. Mitschke, G. Eruçar, M. H. Fsadni, R. R. Roberts, M. M. Sadeghi, B. T. Golding, J. Christoffers and H. Wilkes, *Eur. J. Org. Chem.*, 2021,3854.

Table of Contents

Abbreviations

AIMD	*ab initio* molecular dynamics
AMBER	Assisted Model Building with Energy Refinement
B3LYP	Becke, 3-parameter, Lee-Yang-Parr: hybrid density functional
BO	Born-Oppenheimer
br	broad
CV	cyclic voltammetry
d	doublet
DCM	dichloromethane
DFT	density functional theory
DMF	dimethylformamide
DOS	density of states
dt	doublet of triplets
eq	equivalent
h	hour
FF	force field
HPLC	high performance liquid hromatography
FT	Fourier transform
GGA	generalised gradient approximation
H-bonding	hydrogen bonding
HF	Hartree-Fock
HOMO	highest occupied molecular orbital
HRMS	high resolution mass spectrometry
HTM	Hole transport material
Hz	hertz
IR	infrared
J	coupling constants
kMC	Kintetic Monte Carlo
KS	Khon-Sham
LC-MS	liquid chromatography-mass spectrometry
LDA	lithium diisopropylamide
LiTFSI	lithium bis(trifluoromethylsulfonyl)azanide
LUMO	lowest occupied molecular orbital
m	multiplet
M	molar concentration
Me	methy

MC	Monte Carlo
MP	melting point
MD	Molecular dynamics
mol%	mole percentage
MM	molecular mechanics
m/z	mass/charge ratio
NMR	nuclear magnetic resonance
PES	potential energy surface
PBE	Perdew-Burke-Ernzerhof: density functional
PBE0	Perdew-Burke-Ernzerhof: hybrid density functional
Pd/C	palladium on carbon
OPV	organic photovoltaic
ppm	parts per million
q	quartet
PSC	perovskite solar cell
QC	quantum chemical
QM	quantum mechanics
quan	quantitative
rt	room temperature
s	singlet
SCF	self consistent field
SD	Slater determinant
SWV	square wave voltammetry
t	triplet
td	triplet of doublets
THF	tetrahydrofuran
TLC	thin layer chromatography
TMS	trimethylsilane
UV/VIS	ultraviolet-visible
vDW	van der Waals
v/v	volume fraction
w/w	mass fraction
XC	exchange-correlation

List of Figures

List of Tables

List of Schemes

1 Introduction

1.1. Solar Energy

Renewable energy is expected to play a major role in reaching our target to end the UK's contribution to global warming by the year 2050.[1] The sun is an immense renewable energy resource and yet in 2023 only 4.9% of our electricity was generated by solar power (5.5% globally).[2,3] Over the decade between 2011 and 2021 global PV installations achieved a 30% compound annual growth rate.[4] In 2022 energy generation by solar PV represented the largest absolute growth of all renewable technologies and is now classified as "on track" for achieving Net Zero Emissions by 2050, with growth expected to accelerate further.[3] Crystalline silicon (c-Si) solar cells still dominate the market, accounting for ~95% of photovoltaic (PV) devices being produced, with established manufacturing infrastructures and significant reductions in energy payback times realised over the last decades.[4,5] However, PV technologies need to be developed further to meet our growing energy needs.

In 1839 Edmond Becquerel first observed the photovoltaic (or Becquerel) effect in an electrochemical cell, made up of platinum or gold plates in a conductive solution.[6] Exposing this to solar radiation generated an electric current. Research into the photoconductivity of selenium, first observed by Willoughby Smith in 1873 eventually led to the development of the first solar cell by Charles Fritts in 1883, made up of gold coated selenium wafers.[7,8] Despite their low efficiency and high cost, interest in these devices steadily grew, and by the late 1800s inventors started to register the first patents for solar cells in the USA.[9] In 1954, research into solar cells at Bell Labs led to the invention of the first practical silicon solar cell by Gerald L. Pearson, Daryl M. Chapin, and Calvin S. Fuller, and this breakthrough renewable energy technology was launched into space and into the minds of the general public.[10,11,12]

A shift to renewable technologies comes with a variety of new opportunities and challenges.[13] PV production is highly concentrated in Asia, with mainland China producing 75% of c-Si modules, while Europe, the United States and Canada together contribute just 4%.[4] With respect to other key stages in PV panel manufacturing, China's contribution is even higher, at 80%, and expected to grow over the

coming years.[14] This contrasts with the percentage of cumulative installations realised worldwide, with Europe representing 22% and China 37%.[4] While China's investments have been crucial to lowering the cost and increasing deployment of photovoltaics, the monopoly of global supply chains poses an obvious risk to energy security, which will only increase as our reliance on these technologies grows.[14]

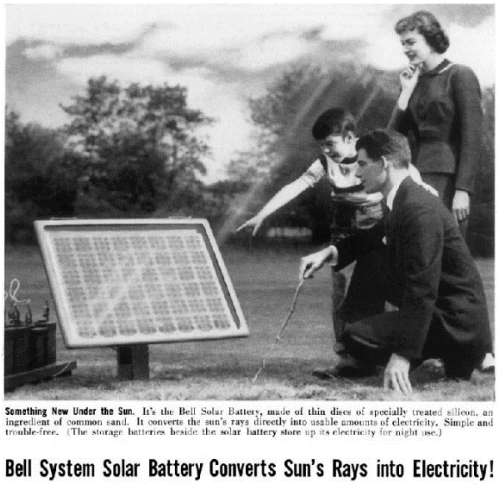

Something New Under the Sun. It's the Bell Solar Battery, made of thin discs of specially treated silicon, an ingredient of common sand. It converts the sun's rays directly into usable amounts of electricity. Simple and trouble-free. (The storage batteries beside the solar battery store up its electricity for night use.)

Bell System Solar Battery Converts Sun's Rays into Electricity!

Figure 1.1 Clip of Bell Labs' advertisement for the first practical solar cell which, "a forward step in harnessing the limitless power of the sun" which appeared in Look Magazine in 1956.[12]

While the energy payback time (EPT) for European produced PV systems is estimated to be just over 1 year in Northern Europe, Dhimish and Badran found thermal defects in 36.5% of the 3.3 million UK installed PV modules studied, suggesting that actual EPTs are significantly higher.[4,15] Another key issue that we can expect to face in the near future is the treatment and recycling of an ever-growing number of modules approaching their end-of-life.[16] Therefore, going forward, PV production should be more geographically diversified and move from a linear to a circular economy approach. To achieve this, new low-cost technologies must be developed in which potential recyclability is a key design element.

Second generation PV technologies, including chalcogenide (CdTe, CIGS, CIGSS) thin films, have demonstrated comparable efficiencies to conventional c-Si solar cells. However, issues related to the scarcity, cost and safety profiles of their constituent materials, as well as the market dominance of silicon-based solar panels, currently reduce the competitiveness of these technologies.[13,17] Meanwhile, third generation PV technologies, are widening the scope of PV to applications beyond the effective capabilities of conventional c-Si.

1.2. Third generation photovoltaic technologies

Emerging thin-film technologies, such as organic photovoltaics (OPV) and perovskite solar cells (PSC), are able to operate under low light conditions and can be printed easily and cheaply as lightweight-flexible devices, making them suitable for integration within indoor and portable systems, amongst others.[18] Reported efficiencies have been steadily climbing over the years, with further growth expected. This, along with their advantageous use of cheap, naturally abundant raw materials has led to an ever increasing research interest since their advent in the early 1990s.[19]

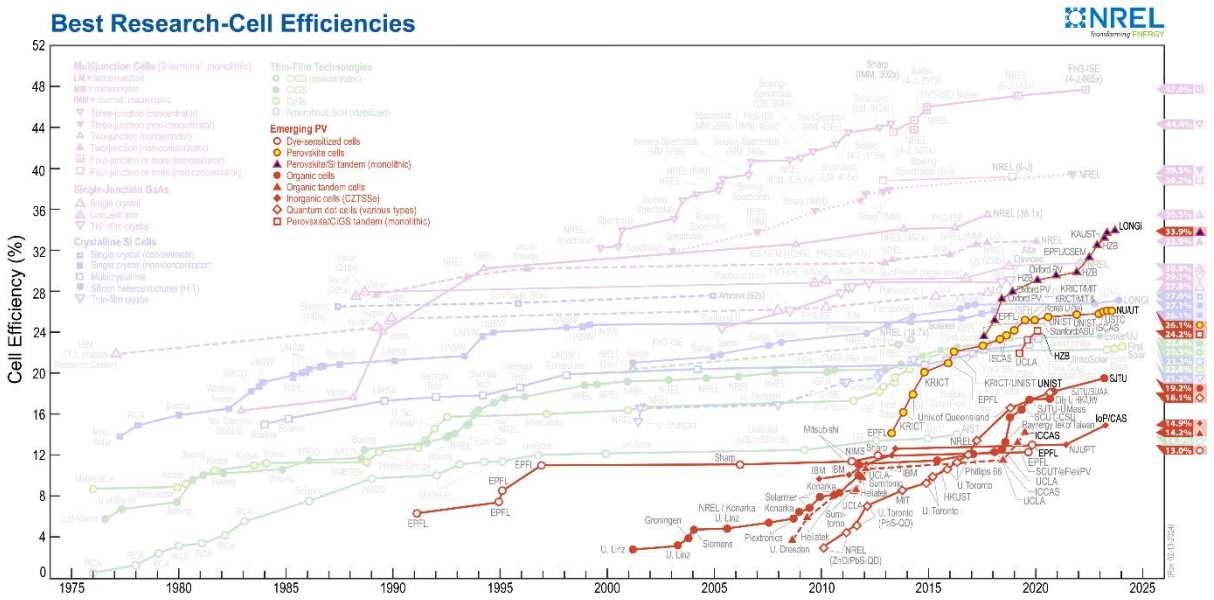

Figure 1.2 NREL chart comparing champion photovoltaic device efficiencies, with emerging PV highlighted.[17]

1.2.1. Small-molecule and polymer organic photovoltaics (OPVs)

Organic solar cells utilise conductive organic small molecules or polymers for light absorption and charge transport, with polymer solar cells being the most commonly used type in this category.[20] The photoelectric properties of organic materials have been explored for over a century, with Pochettino, and later Volmer, working on the photoconductivity of anthracene in the early 1900s.[21,22] After Calvin and Kearns reported on the photovoltaic effect of magnesium phthalocyanines in 1958, the field took off with biomolecules and organic dyes, including porphyrins, eventually incorporated into working OPV devices by the 1970s.[20,23] Heeger, MacDiarmid and Shirakawa were awarded the 2000 Nobel Prize in Chemistry, 23 years after first reporting their work on the highly conductive doped polyacetylene,

leading to greater recognition of the field and increased research interest into conductive polymers.[20,24] These materials have high extinction coefficients, enabling the production of thin, light-weight (and flexible) devices, while solution processing allows for simple and scalable fabrication.[25,26] While efficiencies have been increasing over the years, polymer-based devices are prone to photo-induced oxidation and morphology changes.[27] Further, attempts to design organic polymers which do not suffer from the typically limited absorption range, often results in a trade-off between PCE and stability.[27]

1.2.2. Dye-sensitised solar cells (DSSCs)

Taking inspiration from photosynthesis, Grätzel and coworkers invented the dye-sensitised solar cell, first reported in a 1991 Nature article.[28] In a typical cell, electrodes sandwich the semiconductor layer, consisting of a photoabsorbent dye attached to a mesoporous nanoparticle electron transport layer and a hole transporting electrolyte, which regenerates the dye and closes the circuit.[29] PCEs of over 13% have been achieved under full sun illumination.[30] This increases to 34% under artificial light conditions, where the efficiency ceiling is also higher than AM1.5 since there are no spectrum losses from IR photons.[31] DSSCs have several advantages, from their efficient production to their adaptability with respect to a range of deployment scenarios. Their indoor applications are envisaged to become increasingly relevant as Internet of Things (IoT) devices proliferate.[13] Research is being carried out to tackle efficiency limits and stability issues, such as those that arise from the use of liquid electrolytes, and organic dyes have been developed that outperform the less sustainable early ruthenium dyes.[29]

1.2.3. Perovskite-based solar cells (PSCs)

Perovskite solar cells represent a recent breakthrough in thin-film PV technologies. The light-absorbing layer in these devices has a "perovskite" ABX_3 crystal structure, in which both cations A and B bind to the typically halide, X, counterion. Lead methylammonium triiodide ($CH_3NH_3PbI_3$) is the most used perovskite in these devices, due to its favourable charge-carrier lifetime, extraction and mobility properties.[29,32,33] Kojima et al, and later Im et al., first used perovskite absorbers within DSSC type devices, however these were found to be highly unstable and of low efficiency.[34,35] Lee et al. made crucial breakthroughs in the field by replacing the corrosive liquid electrolyte with the solid-state hole transporter spiro-OMeTAD, and later eliminating the mesoporous TiO_2 electron extraction layer.[29] This resulted in the first functional thin film PSCs, which achieved efficiencies above 10%.[36,37] Since then, the efficiencies of PSCs have increased rapidly, reaching 26.1% and breaking the 30% mark at 33.9%

within silicon-based tandem cells.[17] Perovskite solar cells are a rapidly-developing emerging thin-film PV technology with great potential, mainly due to their high efficiencies and low cost.[36] In addition, PSCs make use of naturally abundant, low-cost starting materials and are compatible with printing technologies making them intrinsically low cost in the long-term.[38]

Planar n-i-p heterojunctions, they are comprised of a transparent conducting oxide (TCO) cathode, an n-type electron transport material (ETM), a perovskite absorber layer, a p-type organic hole transport material (HTM), and a metal anode. When incident light hits the perovskite absorber, electrons are excited to a higher energy level leaving behind a positively charged 'hole'. The functions of the HTM and ETM are to shuttle holes and electrons to the respective electrodes, blocking charge recombination, creating a charge gradient and generating a current (Figure **3**).[39] PSCs still face numerous challenges that limit their performance and commercial viability. Research into different perovskites, which replace the highly toxic water-soluble Pb^{2+} with different metal cations such as tin and germanium, is ongoing. However reported efficiencies of such devices have yet to catch up with those achieved using lead methylammonium triiodide.[17] The HTM is another crucial research avenue.[38]

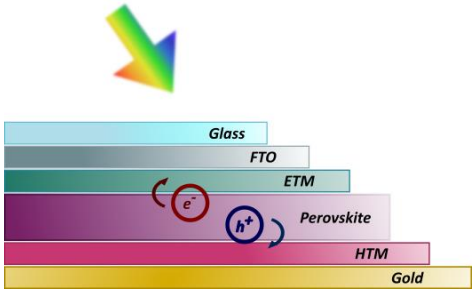

Figure 1.3 Charge transfer in a conventional n-i-p perovskite solar cell.

1.3. HTMs for perovskite solar cells

The HTM plays a major role in controlling the overall performance and cost of these devices.[38] The hole mobility, μ_h, refers to the average velocity (i.e. the drift velocity, v_d) of a charge carrier travelling through a material in response to an applied electric field, E, and is given by,

$$\mu_h = \frac{v_d}{E} \tag{1.1}$$

The conductivity of a device is proportional to the mobility of the hole transport layer (and the mobility of the electron transport layer), given by,

$$\sigma \propto n_i q \mu_h \tag{1.2}$$

where, n_i is the charge density and q is the electric charge.

Charge recombination, due to charge build-up at the HTM/perovskite interface, limits the efficiency of the solar cell and remains a challenge. In addition, state-of-the-art HTMs, such as spiro-OMeTAD, are expensive and difficult to synthesise, requiring expensive transition metal catalysts, inert reaction conditions and arduous purification procedures.[38] Novel HTMs, based on aromatic amide, azomenthine and hydrazone backbones, have been developed at a fraction of the cost of conventional materials, employing simple condensation chemistry.[38,40,41] Their synthesis can be carried out under ambient conditions, without the need for metal catalysis, and trivial isolation techniques furnish these products in high yields and purities. By combining different cores and side groups, structures may be tuned to optimise performance. However, hole mobilities and thus power conversion efficiencies of their devices remain rather low.

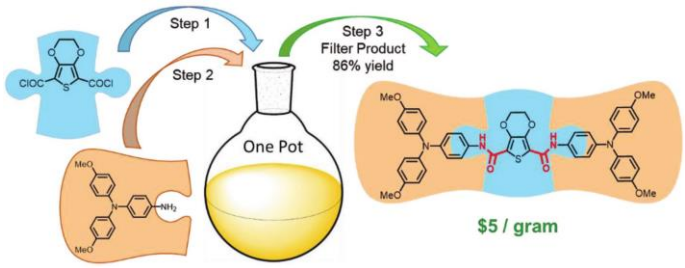

Figure 1.4 One pot synthesis of EDOT-Amide-TPA, reproduced from Petrus, et al. (2018).[38]

Spiro-OMeTAD itself has an intrinsically low mobility due to its propellor-like structure, which results in large intermolecular distances. While the use of dopants, typically bis(trifluoromethane)sulfonamide lithium salt (LiTFSI) and 4-*tert*butylpyridine (*t*BP), substantially improve the performance of Spiro-OMeTAD-based PSCs in the short-term, they undermine long term stability.[42] In organic semiconductors (p-type) doping involves the chemical oxidation the semiconductor to its radical cation. The energy of the singly occupied molecular orbital (SOMO) of the doped semiconductor is slightly lower than the HOMO of the pristine material.[43] This provides an energetic driving force for charge hopping through the semiconductor and increases charge extraction and reduces charge recombination at the perovskite-HTM interface. Therefore, doping results in increased mobility, conductivity and a higher device fill factor (FF).[43] LiTFSI accelerates the oxygen-induced oxidation of spiro-OMeTAD, by stabilising the spiro radical cation, spiro-OMeTAD$^{+\cdot}$, with the TFSI$^-$ anion and forming a complex with the metal cation (spiro-OMeTAD$^{+\cdot}$TFSI$^-$ Li_xO_y).[42] Cobalt (III) complexes, like FK209, are thought to effect p-doping via a similar mechanism.[42] *t*BP, commonly used in conjunction with dopants like LiTFSI, has multiple roles but is primarily thought to improve the morphology of dopant containing films by preventing agglomeration of LiTFSI and phase segregation.

The hygroscopic and deliquescent properties of LiTFSI result in accelerated moisture-induced degradation of the perovskite as well as the spiro-OMeTAD HTL.[44] Further, its use results in a gradual weakening of the adhesion between the HTL and perovskite.[45] *t*BP interacts with the perovskite and spiro-OMeTAD layers, resulting in the formation of PbI_2 complexes and the uncontrolled growth of large crystalline HTM domains, leading to a deterioration in both the performance and stability of devices over time.[46,47] Another problem is the gradual diffusion of *t*BP out of unencapsulated devices. Since the first reported PSC, there has been considerable research interest in developing low-cost dopant-free alternatives to spiro-OMeTAD, as this would be instrumental in increasing the real-world viability of these devices.

1.3.1. HTM design rules

HTMs within PSCs need to obey a number of design rules. Frontier orbital energies must be compatible with the perovskite absorber; alignment (<0.5 eV) of the highest occupied molecular orbital (HOMO) with perovskite valence band (-5.43 eV) minimise losses, while a high lowest occupied molecular orbital (LUMO) compared to the perovskite conductance band (-3.93 eV) ensures that the HTM serves as an effective electron blocking layer.[40] High charge carrier mobilities ($>10^{-5}$ cm^2 V^{-1} s^{-1}) and high conductivities ($>10^{-4}$ S cm^{-1}) are required for good device efficiency.[40] In addition HTMs must be intrinsically stable under device operation conditions, and preferably also lend stability to the perovskite layer, by acting as barriers to air and moisture.[40] Finally, inexpensive and facile large-scale synthesis would make these materials commercially attractive.[40] Identifying structural properties of the HTM that predict performance, would enable the rational design of more efficient, stable and cost-effective alternatives to state-of-the-art materials.

Structural properties that relate to film quality, stability and hole mobility must be considered. These include the degree of conjugation and planarity of HTMs, as well as potential intermolecular interactions like π–π stacking and hydrogen bonding (H-bonding) within the HTL and with the perovskite layer. For large-scale solution processing, high solubility in non-polar perovskite-compatible common organic solvents is desired. High glass transition temperatures mitigate thermal stress, preventing the uncontrolled formation of thermodynamically stable crystalline domains which may result in an increase in trap sites.[48] While crystalline materials have an intrinsically higher charge carrier mobility than amorphous materials, the alignment of molecules with respect to the direction of charge transport and grain boundaries at the perovskite HTL interface may be problematic.[42] Furthermore, large-scale reproducible devices are not as easily achieved as with amorphous HTMs.[49]

HTMs also need to be adapted to the type of PSC developed. Inorganic materials that require sol–gel processing in polar solvents and annealing are not suitable for n-i-p applications, while the impact of the HTM properties such as hydrophilicity on perovskite crystallisation needs to be considered in inverted p-i-n structures.[42]

In finding the best trade-off between efficiency, stability and cost, amorphous organic materials have been the most widely studied as HTMs in conventional PSCs. Many of these are triphenylamine- (TPA) based donor-acceptor-donor D-A-D materials. TPA serves as a good donor unit, since the central nitrogen moiety is readily oxidised, and its bulky structure prevents aggregation and improves solubility.[42,50] Other organic HTMs include donor-π-acceptor (D-π-A) structures, which may be easier to tune and have higher intrinsic hole mobilities due to increased planarity which enhances π-π stacking interactions.[42] What follows is an overview of some of the best performing organic, organometallic, and inorganic HTMs reported in the literature.

1.3.2. TPA-Based Spiro-type HTMs

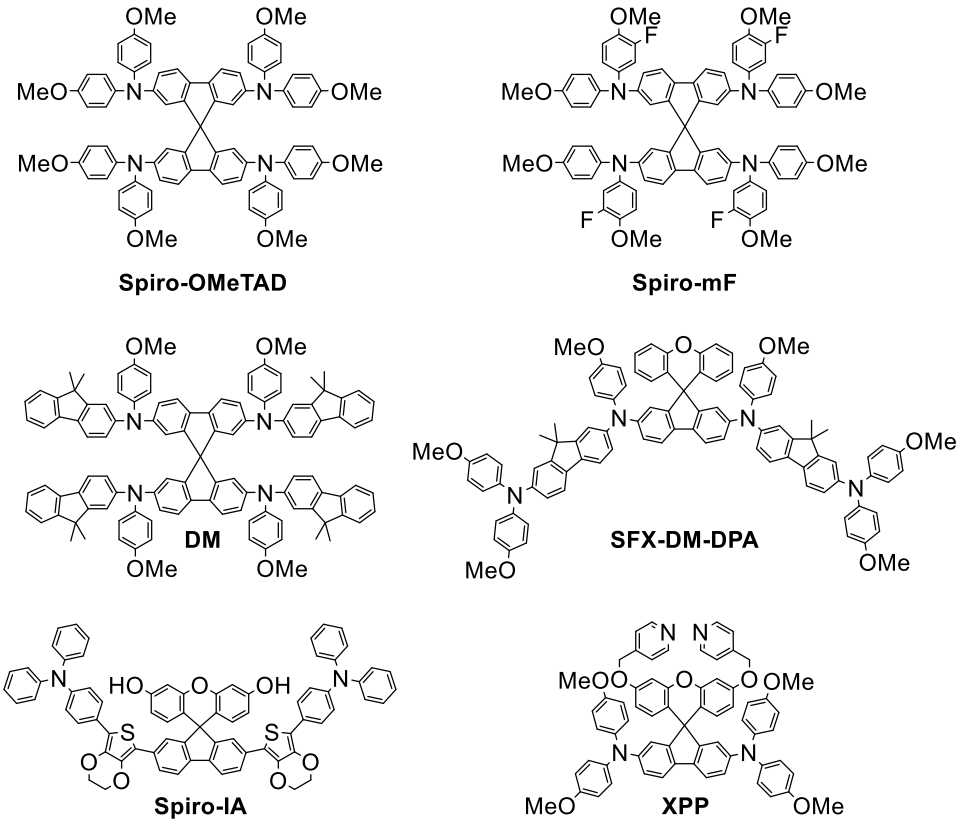

Figure 1.5 TPA-based spiro-type HTMs.[42,51-55]

The use of a spirobifluorene (SBF) core, consisting of two perpendicular π-conjugated systems connected via a tetrahedral sp3 hybridised carbon atom, gives rise to rigid bulky molecules that are less prone to aggregation and tend to form stable amorphous solids.[42] Their structure also gives rise higher solubility in common organic solvents and higher thermal stability, which are all desirable features in HTMs. [42] Spiro-OMeTAD remains the state-of-the art HTM used in Per-SCs, however, other spiro-type HTMs have now been developed. Spiro-mF, which has a certified PCE of 24.64%, is a fluorinated analogue of Spiro-OMeTAD, with a high pristine hole mobility (μ = 7.4748 × 10^{-3} cm^2 V^{-1} s^{-1}).[51] The improved F-induced intermolecular interactions lead to denser film packing and increased hydrophobicity, resulting in high long-term stability in wet conditions without encapsulation (87% efficiency retention after 500 hours). Reducing the need for additives to increase stability, a dopant-free Spiro-IA PSC (surface area = 1.02 cm^2) was reported with 15.66% PCE, comparable to Li-doped Spiro-OMeTAD, as well as the spirofluorene-xanthene (SFX) tBP-free HTM XPP (device efficiency of 19.5%).[52,53] Based on the spiro[fluorene-9,9'-xanthene] (SFX) core, SFX-DM-DPA has extended π-conjugation and an efficiency of 22.7%.[54] The HTM DM, a fluorene-terminated spiro-OMeTAD derivate, benefits from a deep HOMO energy due to the absence of the electron donating methoxy groups.[55] While the mobility of DM is comparable to that of spiro-OMeTAD, the HOMO energy level tuning results in a high V_{OC} which contributes to DM-based devices demonstrating high efficiency (23.2% and 21.7% for 0.09 and 1 cm^2 active area, respectively). The devices also show impressive thermal stability, due to the rigidity of the fluorines which give rise to a high glass transition temperature up to 161 °C. Despite recent advances, dopant-free, spiro-linked TPA-based HTMs have an intrinsically low mobility arising from the high intermolecular distances and weak interactions due to the bulky perpendicular spiro core and the propellor-like TPA moieties.[42]

1.3.3. TPA-based Linear HTMs

Since the development of spiro-OMeTAD as a solid-state HTM, many other linear HTMs have been designed, with structures comprising one core and two TPA side units. This structure allows for easy synthesis while providing good intermolecular π–π interactions, giving rise to higher mobilities. Various HTMs have been developed with thiophene, carbazole and EDOT derivatives commonly employed as cores.[42] The thiophene-based hole transporter Z26 was shown to have an efficiency of 20.1%, with a mobility of 1.34 × 10^{-4} cm^2 V^{-1} s^{-1} (spiro-OMeTAD, μ = 4.32 × 10^{-4} cm^2 V^{-1} s^{-1}).[56] High mobility was attributed to the planarity of this material, while the thiophene sulfur readily interacts with the perovskite iodine leading to high interfacial coupling with the perovskite. This allows the material to form a smooth protective hydrophobic layer over the perovskite which may explain the

increased stability of Z26 devices over those constructed using spiro-OMeTAD, despite the low glass transition temperature of Z26 of 98 °C.

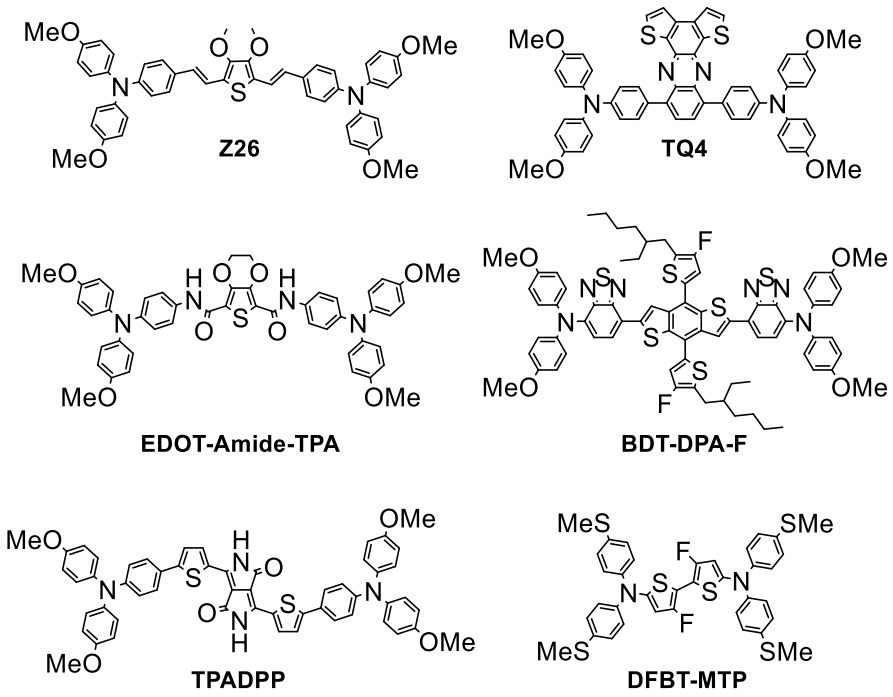

Figure 1.6 TPA-based linear HTMs.[38,56-60]

The development of dopant-free HTMs is crucial to advancing the field of PSCs. DFBT-MTP, a planar fluorinated dopant-free HTM, was used in p–i–n PSCs achieving 20.2% PCE.[57] The high efficiency and stability of n-i-p structured PSCs fabricated with dopant-free TQ4 (over 21 %) was attributed to the quinoxaline core of the HTM.[58] Its coplanar π-extended structure enables close packing, with a strong face-to-face orientation, resulting in a hole mobility of 2.08×10^{-4} $cm^2\,V^{-1}\,s^{-1}$. TPADPP, designed to undergo intermolecular H-bonding, was found to have a hole mobility of 3.09×10^{-4} $cm^2\,V^{-1}\,s^{-1}$, and when used in PSC resulted in 21.62% without the use of dopants.[59] The role of packing is also evident in dopant-free BDT-DPA-F based PSCs, which were reported to have a record breaking certified PCE of 22.48 % and a module PCE of 20.17 % (15.64 cm^2).[60] The HTM self-assembles into a fibril network, resulting in reduced energetic disorder, improved hole mobility (2.05×10^{-3} $cm^2\,V^{-1}\,s^{-1}$), and T80 lifetimes over 1200 h, under continuous operation or thermal aging (85 °C) conditions.

While these materials show remarkable improvements in efficiency for dopant-free HTMs, their synthetic cost presents a challenge. Petrus et al synthesised a series of HTMs with costs as low as \$4 g^{-1}.[38,40,41,61] Hydrazone, azomenthine and amide linkers were used to connect commercially available core and TPA units, using simple condensation chemistry. Close molecular packing led to thin (~50 nm compared to 250 nm for spiro-OMeTAD) hydrophobic pinhole-free films, resulting in high stability.[38,40,41] Their best performing HTM, EDOT-Amide-TPA outperforms Spiro-OMeTAD, with stabilised power conversion efficiencies up to 20.0% and a mobility of up to 2.1×10^{-4} cm^2 V^{-1} s^{-1} upon addition of LiTFSI.[38] The amide bond leads to intermolecular H-bonding and is thought to coordinate to the Li-additive, mitigating ion migration and increasing stability of the doped device.[38,61] Balancing materials cost with device efficiency is crucial for future design.

1.3.4. TPA-based star shaped HTMs

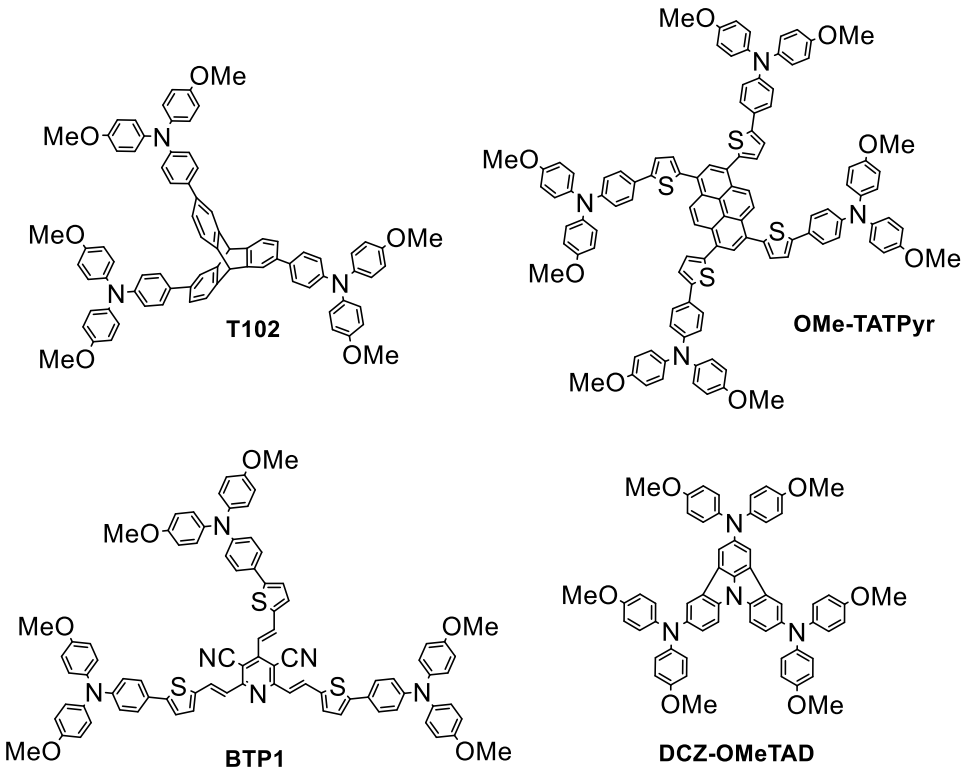

Figure 1.7 TPA-based star shaped HTMs.[62-65]

One disadvantage of linear structures is that strong π–π interactions result in lower solubility and a tendency to agglomerate.[42] Star shaped HTMs, which consist of a core and 3 or more arms, tend to

have higher solubilities, thermal stabilities a more stable amorphous character.[42] Since the development of the first star-shaped HTMs in 2014, including triptycene-based T102 (12.24% efficiency), efficiencies have increased significantly.[62] The pyrene-based OMe-TATPyr, which was shown to have a higher mobility than Spiro-OMeTAD (μ = 2.28× 10^{-4} cm^2 V^{-1} s^{-1} vs 1.11 × 10^{-4} cm^2 V^{-1} s^{-1}) and gave rise to a high efficiency (20.6%) device, which was attributed to the high delocalisation and intermolecular stacking interactions afforded by its rigid, planar structure.[63] The Pb–S interaction is thought to passivate the defects at the HTL/ perovskite interface, contributing to its high stability (60 days). One of the highest reported efficiencies of star-shaped, TPA-based HTMs in conventional n-i-p PSCs was obtained with the fused carbazole-based DCZ-OMeTAD, at 21.6%.[64] Inverted PSCs using the HTM BTP1 (BTP1 μ = 1.66 × 10^{-4} cm^2 V^{-1} s^{-1}; Spiro-OMeTAD $\mu \cong$ 2 × 10^{-5} cm^2 V^{-1} s^{-1}) processed by the green solvent of 2-methylanisole (2MA) yielded high PCEs of 24.34 %, an efficiency which was maintained to over 98 % for 1000h in an N_2 atmosphere under 1 sun illumination.[65]

1.3.5. Other Small Molecular HTMs

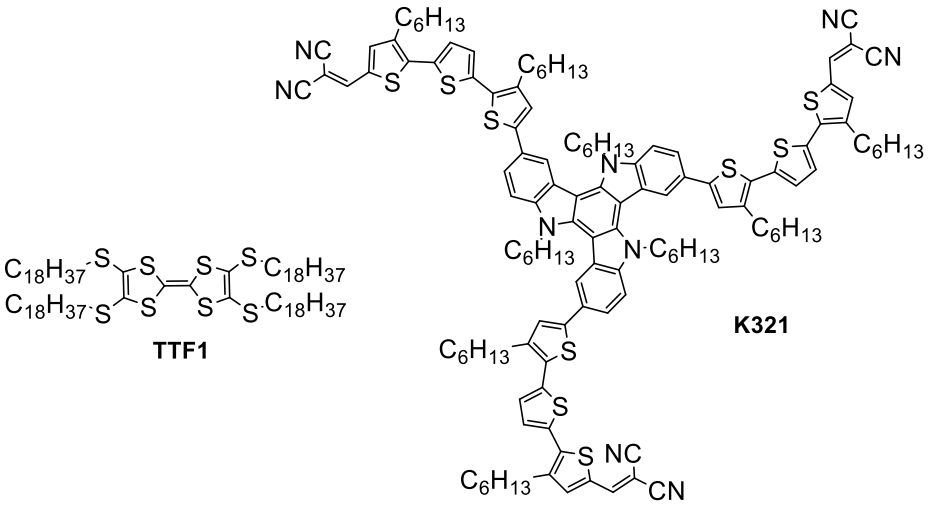

Figure 1.8 HTMs TTF1 and K321.[66,67]

Other small organic molecules that do not make use of TPA side arms, have been developed as HTMs. Planar linear D-A and discotic structures are amongst the most successful dopant-free types, with many featuring π–π stacking, extended conjugation and S–Pb HTM-perovskite interactions, which are favourable from a charge transport and stability perspective.[42] Since the development of the first small

organic dopant-free HTM, TTF-1 (11.03% efficiency) in 2014, efficiencies and stabilities have continued to rise.[66] The star-shaped HTM KR321, which contains a triazatruxenecore and thiophene rings as π-bridges, exhibited an efficiency of 19.03% without the use of any dopants.[67] The increased conjugation length, raises the HOMO level, while the face-on orientation lends itself to a high mobility (2.6×10^{-4} cm^2 V^{-1} s^{-1}). The dopant-free KR321 device maintained 60% of its initial efficiency after 650 h, while efficiency dropped to 20% of the initial efficiency in the doped spiro-OMeTAD device.

1.3.6. Polymeric HTMs

Polymeric HTMs have a number of advantages over small organic molecules. While charge transport in small molecules occurs via slow intermolecular charge transport, the long conjugated pathways in polymers enable rapid intramolecular charge transport which enhances the overall hole mobility of the material. Their flexibility allows for the use of thinner HTLs within devices, which further increases mobility.[42] TPA-based polymers, polytriarylamine (PTAA) and its functionalised derivatives have been widely explored.[68] Undoped HTM-P1 devices were able to achieve 17.2% efficiency due to their high hole mobility (1.6×10^{-4} cm^2 V^{-1} s^{-1}) and retained over 80% initial efficiency after 30 days in ambient conditions (30% RH) without encapsulation.[69]

D–π–A type amorphous conducting polymers have been received much interest due to their easily tuneable structure, enabling favourable face-on orientation packing, improved electronic properties, and the formation of a hydrophobic surface which prevents perovskite degradation.[42] The first reported dopant free D–π–A-type conducting polymer was PCBTDPP, which showed 5.55% of efficiency in PSCs which was maintained without any appreciable losses over 1000 h.[70] Since then a number of advances have been made. Nonencapsulated asy-PBTBDT devices, processed using the green solvent 2-methoxyanisole (2-MA), and were found to have a high efficiency (18.3%), which fell by only 10% after 30 days at 50–75% RH.[71] The impressive hole mobility (1.13×10^{-3} cm^2 V^{-1} s^{-1}), hygrophobicity and high glass transition temperature of this HTM contributed to the high PCE and stability of devices.

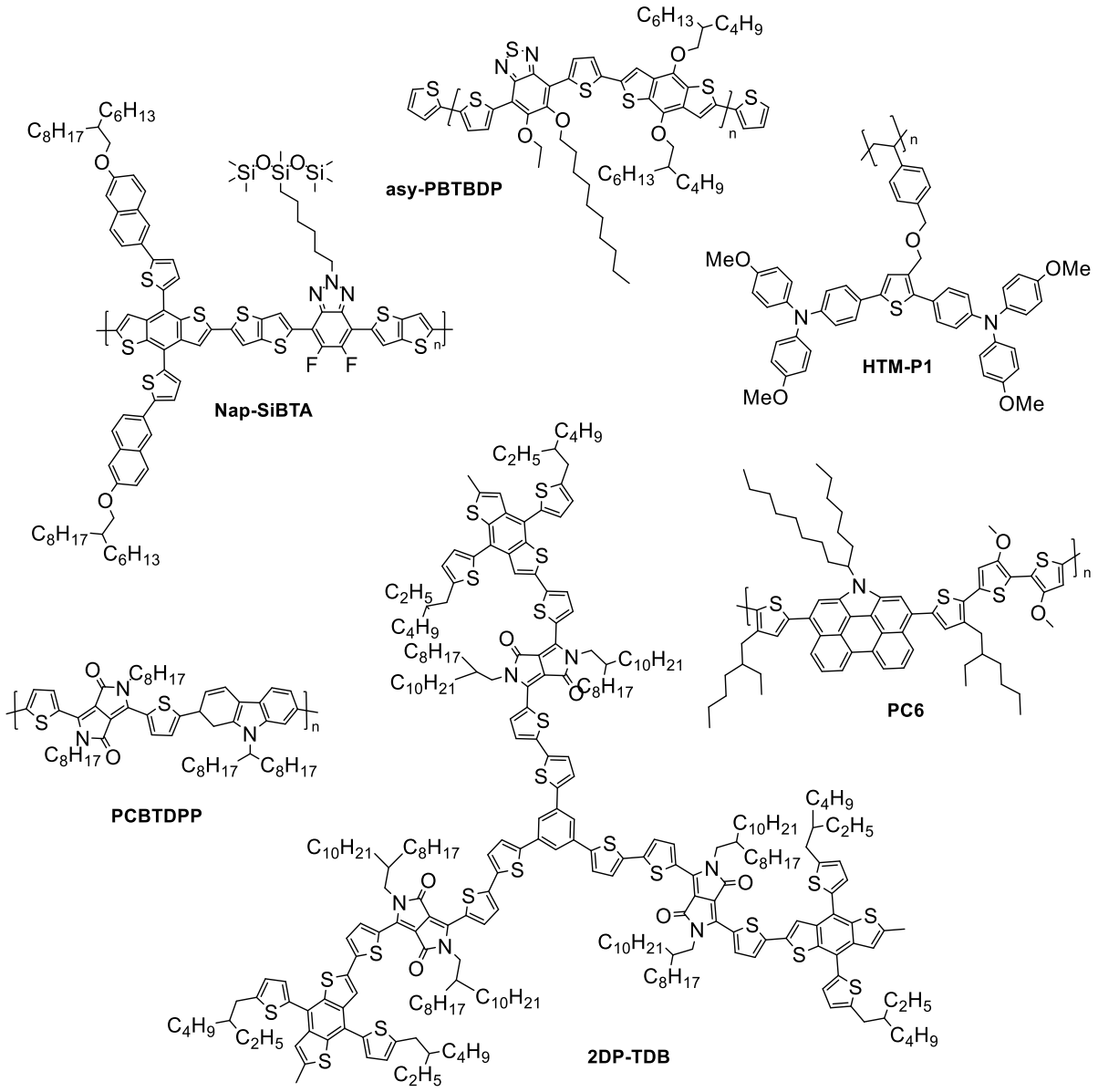

Figure 1.9 Polymeric HTMs.[69-74]

A PSC employing PC6, a phenanthrocarbazole-based dopant-free polymeric HTM (μ = 8.2 × 10^{-4} cm^2 V^{-1} s^{-1}), exhibited high efficiency (22.2%) and stability.[72] The S–O interactions are thought to fix the molecular geometry, reducing the reorganisation energy, the broad planar PC backbone improves π–π stacking interactions, enhancing mobility, and oxygens are able to bind to and passivate the perovskite surface. The two-dimensional polymer HTM 2DP-TDB exhibits extended π-electron delocalisation into the two-dimensions. PSCs employing a formamidine-based spacer and the dopant-free 2DP-TDB HTM (μ = 2.1 × 10^{-4} cm^2 V^{-1} s^{-1}) achieved PCE of up to 22.17%.[73] The dopant-free polymer

Nap-SiBTA-based PSC were shown to have a high efficiency (23.07%) and high fill factor (80.85%).[74] The thienothiophene groups are thought to give rise to a high degree of planarity and promote face-on orientation, resulting in good packing which improves stability and charge transport behaviour, with a hole only device mobility of 2.36×10^{-3} cm^2 V^{-1} s^{-1}. The non-encapsulated device was found to maintain 93% of its initial efficiency after 1000 h. While conductive polymers are promising HTMs, issues like batch-to-batch variation and challenges with purification still make them challenging from to commericalise.[42]

1.3.7. Organometallic HTMs

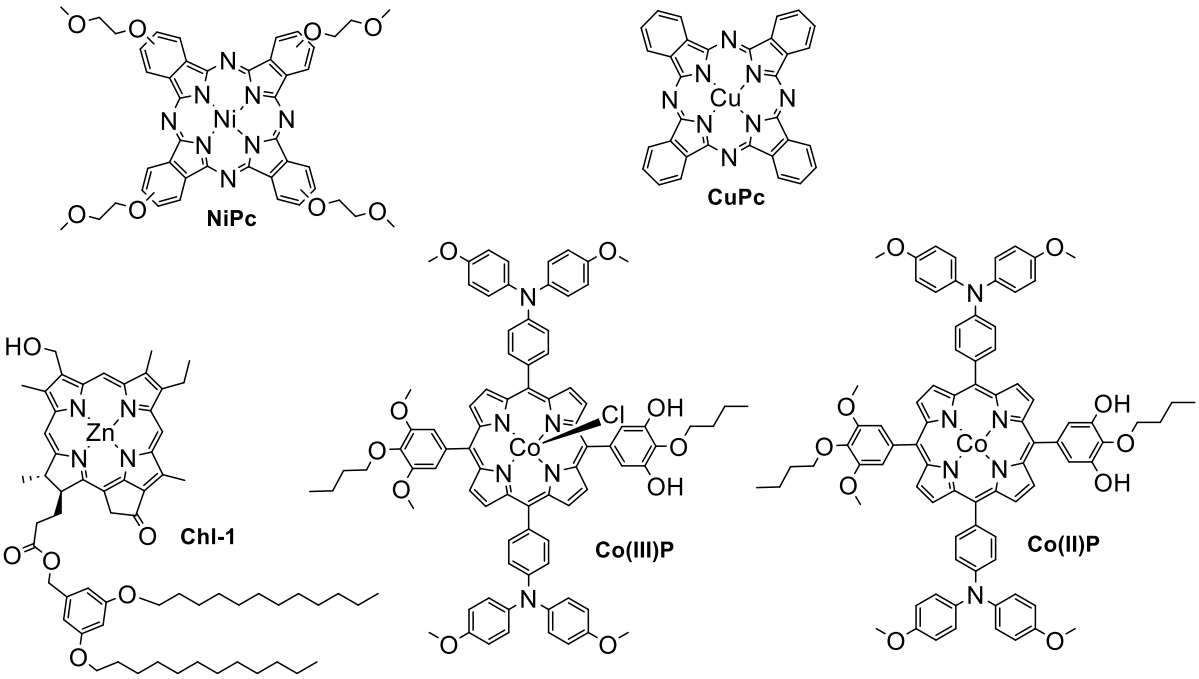

Figure 1.10 Organometallic HTMs.[75-78]

Taking inspiration from nature, organometallic derivatives of chlorophyll, phthalocyanines and porphyrins have been developed as dopant-free HTMs, with various metal ligands explored. These compounds benefit from high mobilities due to strong π–π stacking and good chemical stabilities. PSC devices employing copper phthalocyanine (CuPc) have been shown to obtain efficiencies over 20%, remaining stable at 85 °C for 2000 h.[75] Despite their light-harvesting abilities, natural chlorophylls (Chls) were shown to be suitable for use in PSCs, with a device using Chl-1 achieving 11.44% efficiency,

in part due to the high mobility (6.49×10^{-3} cm^2 V^{-1} s^{-1}) of the HTM.[76] A PSC device employing a dopant-free mixed Co(II) and Co(III) porphyrins has recently been reported to achieve 20.5% of efficiency with high thermal stability.[77] The porphyrin device retained over 90% of its initial efficiency after 1000 h, in contrast with 20% in the doped spiro-OMeTAD device. PSCs with a Ni phthalocyanine (NiPc) dopant-free HTMs were found to achieve a certified efficiency of 21.03%, with excellent stability to moisture, heat, and light-induced degradation.[78] While organometallic HTMs are interesting candidates with favourable properties, like polymeric HTMs, their cost remains prohibitive for large scale commercial deployment.

1.3.8. Inorganic HTMs

Inorganic HTMs benefit from low cost, suitable band alignment, as well as high stabilities and hole mobilities. CuI was the first reported inorganic HTM, and was incorporated by spray deposition in a Na-doped, TiO_2 mesoporous device shown to yield 17.60% of efficiency with over 90% maintained after 90 days at 40–50%RH.[79,80] CuSCN was found to exhibit high a mobility of 1.2×10^{-3} cm^2 V^{-1} s^{-1} (spiro-OMeTAD $\mu = 1.4 \times 10^{-6}$ cm^2 V^{-1} s^{-1}) and thin CuSCN HTLs deposited by spin-coating gave a device of high efficiency (18.0%), which increased when combined with a graphene oxide spacer (20.4%) and gave excellent operational stability for 1000 h under 1 sun illumination at 60 °C.[81] Other inorganic HTMs, such as $Cu_{2-x}GeS_3$, $CuGaO_2$ have also been found to give highly stable efficient devices.[82,83] An all-perovskite tandem inverted (p-i-n) PSC using NiO_x nanocrystals with Me-4PACz self-assembled monolayers achieved 26.3% certified PCE, maintaining at 86% after 500 h of operation.[84] Processing issues, including poor solubility in common organic solvents, as well as the requirement of cumbersome deposition methods and thermal annealing, limit the suitability of most inorganic HTMs for conventional n-i-p PSCs, especially at a large scale.[42]

1.3.9. Designing high mobility HTMs

As we have seen, various types of HTMs have been investigated, with dopant-free HTM-based devices now achieving some of the highest reported efficiencies. Amorphous organic small molecule HTMs seem to have the most advantages in terms of versatility, efficiency, stability and cost, as well as reproducibility of their devices. From some of the examples above, we can see that high hole mobilities do not necessarily lead to the highest device efficiencies, and vice versa. The stability of HTL films and their interaction with the perovskite layer also play a major role in long term performance.

Nevertheless, mobility and efficiency are intrinsically linked, and designing with high mobility in mind, while balancing cost and stability, is crucial for developing better performing HTMs.

1.4. Understanding hole mobility in amorphous small-molecule organic semiconductors

The mobility of an HTM is dependent on the interplay of various properties, including molecular properties, like the electronic structure, dipole moment and polarisation character, as well as its packing behaviour.[85,86] Compared to most inorganic and crystalline semiconductors, organic amorphous HTMs suffer from low charge carrier mobilities, due to the underlying mechanism governing charge transport.[87] Mobilities are typically five to ten orders of magnitude lower than those of inorganic semiconductors, limiting device efficiencies. In disordered small molecule organic semiconductors, charge carriers are localised on energetically discrete sites (i.e. individual molecules), and move through the material via a thermally assisted hopping process, as parameterised by the Miller-Abrahams and Marcus rate equations.[88,89] The Marcus hopping rate between two sites, *i* and *j*, is given by,

$$k_{ij} = \frac{2\pi}{\hbar}\left|J_{ij}\right|^2 \frac{1}{\sqrt{4\pi\lambda_{ij}k_B T}} \times exp\left(-\frac{\left(\lambda_{ij} + \Delta G_{ij}\right)^2}{4\lambda_{ij}k_B T}\right) \tag{1.3}$$

where $\hbar$ is Plank's constant, k_B is Boltzmann's constant, T is the temperature, and J_{ij}, λ_{ij} and ΔG_{ij}, are the electronic coupling, the reorganisation energy, and the change in Gibbs free energy, respectively.[88] The assumption of the small polaron model, applied in Marcus theory, holds for weakly coupled systems with comparatively larger reorganisation energies.[90] Much work has been done to accurately quantify the influence of molecular parameters on mobility.[91,92] Crucially, the rate equation indicates that mobility, μ, is highly dependent on the energetic disorder, σ, of the material as given by,

$$\mu \propto exp\left(-C\left(\frac{\sigma}{k_B T}\right)^2\right). \tag{1.4}$$

Where C is a fitting parameter.[93] The level of energetic disorder in amorphous small molecule systems itself depends on the distribution of conformations and relative orientation of molecules in the film, and therefore relates to the interplay between intrinsic molecular properties and bulk properties.

Developing novel materials involves the exploration of a vast and complex chemical landscape, which is difficult to navigate using an experimental trial and error approach alone. Various computational methods, including multiscale and artificial intelligence models, are increasingly being used to screen key properties and design new materials.[94,95] Multiscale models have demonstrated accurate

predictions of experimental mobilities over ten orders of magnitude.[92] While computationally demanding, they have been a key to identifying structure-property relationships and elucidating design rules. They have been used to characterise various amorphous semiconductors, including the charge transport properties of Alq_3 and its derivatives.[92] DFT has been used to design and characterise 2.3 million novel molecules, the results of which provides a database for organic semiconductor research.[96] Experimental results provide feedback and validation of in silico design protocols.[97] Synthetic accessibility is another essential aspect of materials design. Retrosynthesis is a common approach, and systems like CAS SciFinder® and Reaxys® have been developed to aid synthetic chemists with planning reaction pathways.[98,99] However, these systems are not intended for high throughput screening applications. Developing automated reaction planning procedures and integrating these within computational material design and screening procedures, would further materials discovery.[94]

1.4.1. DFT predictions of HTM properties

Accurate electronic structures and related single molecule properties, essential for calculating charge carrier mobility, such as the energetic disorder, electronic coupling, as well as optical properties like absorption spectra are readily obtained using DFT methods.[92,94,100] However, thin semiconductor films are large complex disordered systems, containing charge carriers and a distribution of electronic structures. For conformationally restricted molecules in an amorphous matrix, an energetic trade-off exists between achieving minimum energy conformations and favourable intermolecular interactions. Neglecting conformational restrictions, may lead to an overestimation in the width of the energetic disorder of a material. Obtaining a representative measure is particularly important, since small changes in the disorder of the material results in large shifts to the calculated mobility.[94] Friederich *et al.* found that only when reorganisation energies were obtained from conformationally restricted molecules, via the dihedral angle, were mobilities obtained that agreed well with experimental data.[92] The complexity of HTLs results in prohibitively high costs for obtaining representative electronic structures by DFT alone.[94] Hybrid methods are often employed, such as using DFT in conjunction with polarisable force fields to approximate the effect of the molecular environment, including the film matrix and interfaces.[101] In the absence of molecule-specific experimental data, required for the parametrisation of force fields, generalised force fields such as GROMOS and GAFF come into play.[102,103] Artificial neural networks, such as ANI-1 used to predict DFT energies, are also increasingly being used.[104]

1.4.2. Multiscale models for accurate predictions of charge transport properties

The charge carrier mobility of organic semiconductors stems from interdependent molecular, micro- and mesoscale properties, including the arrangement and morphology of molecules on the micro and mesoscale which may result in the formation of ordered domains and percolation pathways.[92,85,94,105,106] Therefore, the accurate prediction of charge carrier mobility, relies on computing effects that occur in the material over different length and time scales, and combining these into a reliable workflow.[94]

Multiscale models that are able to handle single molecule and mesoscale properties, rely on careful passing of outputs between the different steps in the process to arrive at material and device properties.[94] Models must be fine-grained enough to capture the distribution of electronic structures, and related molecular properties, characteristic of disordered systems like amorphous solid HTLs. [92] At the same time, accurate morphologies are required to model mesoscopic charge transport phenomena. These may be obtained by simulating film formation, occurring over long time and length-scales, which depends on the intermolecular interactions of millions of molecules.[94] Mesoscale simulations of charge transport may be parameterised with energetic disorder, coupling and reorganisation energy values.[94] Previously, these parameters were commonly obtained from experimental data, however, for the design of novel materials a first principles approach must be used.[85c]

The morphology of amorphous solid small molecule organic semiconductors is usually kinetically controlled and highly dependent on the processing method. Small changes, like different solvents or spin speeds during spin coating, may give rise to different morphologies.[94] Film formation is a complex process, and accurate atomically resolved simulations are computationally demanding. Coarse graining (CG) techniques may be used to overcome the long time and length-scale challenges of full atomistic simulations.[107] The level of approximation with these methods varies; at the small scale molecular functional groups can be combined, while on a broader scale thin films can be represented by a discretised lattice of groups of molecules.[108,109] The interactions between lattice voxels over the film formation simulation time-scale must be carefully parameterised using the relevant equations or molecular simulations.[94] While most CG methods struggle with nonequilibrium properties, recent work has been done to generate kinetic properties that match an atomistic model. Molecular dynamics simulations can be used to model film growth to obtain properties such as molecular directionality during vapour deposition.[110] However, MD simulations only provide a limited approximation since the large time and length scales involved pose a challenge. Monte Carlo annealing

algorithms overcome this issue by sampling molecular properties, such as molecular position and orientation, as each layer is deposited while constraining preceding layers.[111]

Mesoscale phenomena in organic semiconductors include the formation of morphological domains during film processing and over the device lifetime, as well as charge transport including percolation processes. Kinetic Monte Carlo (kMC) and Master Equation (ME) models are used to calculate mesoscale processes, such as charge hopping between sites using quantum-mechanical or the semiclassical Miller-Abrahams or Marcus rate expressions.[85c,112] In kMC inter-site interactions are treated explicitly, resulting in a higher level of accuracy but also higher computational cost, whereas ME models make use of a mean field to approximate these effects. Using the generalised effective medium model (GEMM), microscopic materials characteristics are used as inputs and the mobility is found by solving a master equation (ME).[113] ME simulations come at a lower computational cost, but struggle with high charge carrier concentrations and low electric field strengths.[114]

Advances in kMC, such as parallelisation, have helped make simulations much faster.[112,115] Early kMC simulations used a cut-off for long-range Coulomb interactions which may result in errors.[114,116] For kMC charge transport simulations, materials are often approximated by a cubic lattice in which the points correspond to the hopping sites and parameterised using experimental data.[112] Coarse-graining enables us to access bigger systems to allow more accurate treatment of phenomena, like percolation effects, that occur over larger length scales taking energetic disorder into account by using e.g., correlated disorder models (CDM).[117,118]

In work by Friederich et al., material morphologies were generated with force fields, parameterised with the outputs from single molecule calculations, and charge carrier mobilities were calculated.[92] A first-principles multi-scale "Quantum Patch" method was used to calculate the hole mobilities of a range of common small molecule amorphous and crystalline organic semiconductors, including Alq_3 and α-NPD, and varying in mobility over ten orders of magnitude.[92] Morphologies were generated using quantum mechanical (QM) procedure and mobility parameters were extracted and fed into the mobility expression. In the Quantum Patch[119] method used, molecules in the system were embedded within an environment of partial charges and optimised until the total energy was converged. Molecular dynamics simulations were used to generate atomically resolved morphologies of the amorphous solids, while crystalline structures were obtained from the literature. The molecules within the matrix were characterised to obtain electronic couplings, reorganisation energies and energetic (polarisation and conformational) disorder, which feeds into the inter-site energy differences. Reorganisation energies obtained from vacuum calculations may be inaccurate for molecules in a solid

matrix in which dihedral angles, and therefore overall conformational degrees of freedom, are largely constrained.[92]

1.4.3. Elucidating structure-property trends for HTM screening

Since accurate predictions are computationally expensive, much work has been done to quantify the influence of various molecular parameters on hole mobility and facilitate HTM screening.[92] Friederich et al. demonstrate that mobility is determined by two key single molecule properties, the conformationally dependent orbital energies, and the dipole-induced polarisation, which relate to the energetic disorder of a material.[92] Energetic disorder, which quenches mobility, has an intrinsic component, due to conformational disorder of molecules, and a polarisation component, which arises from their electrostatic interaction with the matrix.[92,120,121] Friederich et al. found that amongst the 9 HTMs studied, the molecular dipole moment was the most important molecule specific factor influencing the mobility.[92] Friederich et al. showed that high dipoles (>6 Debye), such as in Alq_3, give rise to a high induced polarisation which quenches the mobility.[92] In amorphous materials with a small dipole moment (1.5–4 Debye), the effect of intrinsic disorder on mobility dominates, with polarisation effects being a minor component.[92] It is worth noting that dihedral rotations come at a low energetic cost but can result in significant conformational and HOMO energy changes. In the molecules pFFA and NNP, which have comparable microscopic parameters, the 21% higher intrinsic disorder in the latter accounts for its order of magnitude lower mobility.[92] Electronic coupling and reorganisation energy parameters only dominate mobility in crystalline materials, where the energetic disorder is vanishingly small.[92] Therefore, screening for the dipole moment and intrinsic disorder may be an inexpensive selection procedure.

1.5. Outline of Thesis

Recently, inexpensive, tuneable small molecule organic HTMs have been developed using condensation chemistry.[38,40,41] Some of these HTMs possess a larger molecular dipole moment and nevertheless exhibit high mobilities. This project aims to combine theoretical and experimental approaches to rationalise the relationship between the properties of these materials and their charge transport behaviour, in order to guide the design of novel HTMs.

The theoretical background to the computational methods used is given in *Chapter 2*. The single molecule properties presented in later chapters were obtained using Hartree-Fock (HF) and DFT calculations. Therefore, a brief background of these Quantum Mechanical (QM) methods is presented.

Next, the semi-empirical ab initio MD methods, Classical MD and Force Fields are covered. Finally, the in-house kinetic Monte Carlo algorithm, CharTED-KMC, used in our charge transport simulations, is outlined.

Chapter 3 describes the investigations into the mobility trends of known HTMs, from their single molecule properties to MD and kMC simulations. Of the charge transport parameters investigated, we find that the dipole moment plays a major role. Our DFT calculations show that the best performing HTM also has the highest dipole moment. This is rather surprising since the energetic disorder of amorphous materials is thought to scale with the dipole moment, thereby quenching mobility. Our kMC simulations indicate that while this is indeed the case, the percolation pathways found in high dipole systems suggest that local effects play an important role.

In *Chapter 4* we present the result of kMC and MD simulations which investigate the effect of the HTM matrix and intermolecular interactions. H-bonding and high dipole moments are thought to generate a driving force for enhanced intermolecular interactions, which would have an impact on the energetic noise width of the material. The distributions of HOMO energies and dipole moments were found for a selection of molecules. Taking our cue from crystallography data, the percentage population of dimers in representative systems was investigated theoretically, and as was the effect of dimerisation on the overall dipole moment of dimers. The ability of HTMs to form a stable distribution of dimers within an otherwise amorphous material may explain the favourable PSC performance observed with these high dipole materials.

Chapter 5 covers the synthesis, and results of preliminary opto-electronic property investigations, of a series of high dipole HTMs. These were designed to aid investigations into the effect of the dipole moment and H-bonding on mobility. The asymmetric donor-acceptor (D-A) type HTMs, consist of secondary and tertiary amide linkered molecules, as well as a urea-derivative. The synthesis of TPA-BT is also covered.

Finally, a summary of or main findings and their limitations, as well as an outline of future work that would help further HTM design is presented in *Chapter 6*.

References

1. GOV.UK, *UK becomes first major economy to pass net zero emissions law*, https://www.gov.uk/government/news/uk-becomes-first-major-economy-to-pass-net-zero-emissions-law (accessed November 2019); Department for Business, Energy & Industrial Strategy, *Digest of UK energy statistics 2019*, https://assets.publishing.service.gov.uk/government/uploads/system/uploads/attachment_data/file/820277/DUKES_2019_Press_Notice_GOV.UK.pdf (accessed November 2019).
2. National Grid ESO, *Britain's Electricity Explained: 2023 Review*, https://www.nationalgrideso.com/news/britains-electricity-explained-2023-review (accessed September 2024).
3. International Energy Agency, *Renewables 2023: Analysis and forecast to 2028*, https://www.iea.org/reports/renewables-2023/electricity (accessed September 2024).
4. Frauenhofer Institute for Solar Energy, *Photovotaics report, 2023*, https://www.ise.fraunhofer.de/content/dam/ise/de/documents/publications/studies/Photovoltaics-Report.pdf (accessed December 2023).
5. A. Louwen, W. van Sark, A. Faaij and R. Schropp*, Nat. Commun.*, 2016, **7,** 13728.
6. A. E. Becquerel, *Compt. Rend.*, 1839, **9**, 145; A. E. Becquerel, *Ann. Phys. (Berl.)*, 1841, **54**, 35.
7. W. Smith, *Nature*, 1873, **7**, 303.
8. C. E. Fritts, *Am. J. Sci.*, 1883, **26**, 465.
9. Smithsonian Magazine, *A Brief History of Solar Panels*, https://www.smithsonianmag.com/sponsored/brief-history-solar-panels-180972006/, (accessed January 2024).
10. D. M. Chapin, C. S. Fuller and G. L. Pearson, *J. Appl. Phys.*, 1954, **25**, 676.
11. Vast Power of the Sun Is Tapped By Battery Using Sand Ingredient; new battery taps sun's vast power. *The New York Times*, April 26, 1954, p 1.
12. Bell Telephone Systems, *Bell System Solar Battery Converts Sun's Rays into Electricity!*, via NREL, *Silicon Solar Cell Turns 50*, 2004, https://www.nrel.gov/docs/fy04osti/33947.pdf (accessed February 2024).
13. A. B. Muñoz-García, I. Benesperi, G. Boschloo, J. J. Concepcion, J. H. Delcamp, E. A. Gibson, G. J. Meyer, M. Pavone, H. Pettersson, A. Hagfeldt and M. Freitag, *Chem. Soc. Rev.*, 2021, **50**, 12450.
14. International Energy Agency, *The World Needs More Diverse Solar Panel Supply Chains to Ensure a Secure Transition to Net Zero Emissions*, https://www.iea.org/news/the-world-

needs-more-diverse-solar-panel-supply-chains-to-ensure-a-secure-transition-to-net-zero-emissions, (accessed 01/2024).

15. M. Dhimish, V. Holmes, P. Mather and M. Sibley, *Sol. Energy Mater. Sol. Cells*, 2018, **179**, 72; M. Dhimish and G. Badran, *npj Mater. Degrad.*, 2023, **7**, 14.
16. G. A. Heath, T. J. Silverman, M. Kempe, M. Deceglie, D. Ravikumar, T. Remo, H. Cui, P. Sinha, C. Libby, S. Shaw, K. Komoto, K. Wambach, E. Butler, T. Barnes and A. Wade, *Nat. Energy*, 2020, **5**, 502.
17. NREL Best Research-Cell Efficiency Chart, https://www.nrel.gov/pv/cell-efficiency.html, (accessed February2024).
18. F. Di Giacomo, A. Fakharuddin, R. Jose and T. M. Brown, *Energy Environ. Sci.*, 2016, **9**, 3007.
19. International Energy Agency, *Renewables 2020: Analysis and forecast to 2025*, OECD Publishing, Paris, 2020.
20. P. C. Dastoor and W. J. Belcher, *Substantia*, 2019, **3**, 99.
21. A. Pochettino, *Acad. Lincei Rend.*, 1906, **15**, 355.
22. M. Volmer, *Ann. Physik*, 1913, **40**, 775.
23. D. Kearns and M. Calvin, *J. Chem. Phys.*, 1958, **29**, 950.
24. H. Shirakawa, E. J. Louis, A. G. MacDiarmid, C. K. Chiang and A. J. Heeger, *J. Chem. Soc., Chem. Commun.*, 1977, **16**, 578.
25. F. C. Krebs, S. A. Gevorgyan and J. Alstrup, *J. Mater. Chem.*, 2009, **19**, 5442.
26. F. C. Krebs, *Sol. Energy Mater. Sol. Cells*, 2009, **93**, 394.
27. M. Jørgensen, K. Norrman, S. A. Gevorgyan, T. Tromholt, B. Andreasen and F. C. Krebs, Adv. Mater., 2012, **24**, 580.
28. B. O'Regan and M. Grätzel, *Nature*, 1991, **353**, 737.
29. M. L. Petrus, PhD thesis, Technische Universiteit Delft, 2014.
30. D. Zhang, M. Stojanovic, Y. Ren, Y. Cao, F. T. Eickemeyer, E. Socie, N. Vlachopoulos, J.-E. Moser, S. M. Zakeeruddin, A. Hagfeldt and M. Grätzel, *Nat. Commun.*, 2021, **12**, 1777.
31. H. Michaels, M. Rinderle, R. Freitag, I. Benesperi, T. Edvinsson, R. Socher, A. Gagliardi and M. Freitag, *Chem. Sci.*, 2020, **11**, 2895.
32. D. B. Mitzi, *Dalton Trans.*, 2001, **1**, 1.
33. C. C. Stoumpos, C. D. Malliakas and M. G. Kanatzidis, *Inorg. Chem.*, 2013, **52**, 9019.
34. A. Kojima, K. Teshima, Y. Shirai and T. Miyasaka, *J. Am. Chem. Soc.*, 2009, **131**, 6050.
35. J.-H. Im, C.-R. Lee, J.-W. Lee, S.-W. Park and N.-G. Park, *Nanoscale*, 2011, ***3***, 4088.
36. M. M. Lee, J. Teuscher, T. Miyasaka, T. N. Murakami and H. J. Snaith, *Science*, 2012, **338**, 643.

37. G. E. Eperon, V. M. Burlakov, P. Docampo, A. Goriely and H. J. Snaith, *Adv. Funct. Mater.*, 2014, **24**, 151.
38. M. L. Petrus, K. Schutt, M. T. Sirtl, E. M. Hutter, A. C. Closs, J. M. Ball, J. C. Bijleveld, A. Petrozza, T. Bein, T. J. Dingemans, T. J. Savenije, H. Snaith and P. Docampo, *Adv. Energy Mater*., 2018, **8**, 1801605.
39. A. Extance, *Nature*, 2019, **570**, 429.
40. M. L. Petrus, A. Music, A. C. Closs, J. C. Bijleveld, M. T. Sirtl, Y. Hu, T. J. Dingemans, T. Bein and Pablo Docampo, *J. Mater. Chem. A*, 2017, **5**, 25200.
41. M. L. Petrus, M. T. Sirtl, A. C. Closs, T. Bein and P. Docampo, *Mol. Syst. Des. Eng.,* 2018, **3**, 734.
42. G.-W. Kim, H. Choi, M. Kim, J. Lee, S. Y. Son and T. Park, *Adv. Energy Mater.*, 2020, **10**, 1903403.
43. T. H. Schloemer, J. A. Christians, J. M. Luther and A. Sellinger, *Chem. Sci.*, 2019, **10**, 1904.
44. A. K. Jena, M. Ikegami and T. Miyasaka, *ACS Energy Lett.*, 2017, **2**, 1760.
45. I. Lee, J. H. Yun, H. J. Son and T.-S. Kim, *ACS Appl. Mater. Interfaces*, 2017, **9**, 7029.
46. Y. Yue, N. Salim, Y. Wu, X. Yang, A. Islam, W. Chen, J. Liu, E. Bi, F. Xie, M. Cai and L. Han, *Adv. Mater.*, 2016, **28**, 10738.
47. T. Malinauskas, D. Tomkute-Luksiene, R. Sens, M. Daskeviciene, R. Send, H. Wonneberger, V. Jankauskas, I. Bruder and V. Getautis, *ACS Appl. Mater. Interfaces*, 2015, **7**, 11107.
48. P. Agarwala and D. Kabra, *J. Mater. Chem. A*, 2017, **5**, 1348.
49. S. Gangala and R. Misra, *J. Mater. Chem. A*, 2018, **6**, 18750.
50. C.-G. Zhan, J. A. Nichols and D. A. Dixon, *J. Phys. Chem. A*, 2003, **107**, 4184.
51. M. Jeong, I. W. Choi, E. M. Go, Y. Cho, M. Kim, B. Lee, S. Jeong, Y. Jo, H. W. Choi, J. Lee and J. H. Bae, *Science*, 2020, **369**, 1615.
52. I. M. Abdellah, T. H. Chowdhury, J.-J. Lee, A. Islam, M. K. Nazeeruddin, M. Gräetzel and A El-Shafei, *Sustain. Energy Fuels*, 2021, **5**, 199.
53. B. Xu, Z. Zhu, J. Zhang, H. Liu, C.-C. Chueh, X. Li and A. K.-Y. Jen, *Adv. Energy Mater.*, 2017, **7**, 1700683.
54. H. Wang, C. Wu, M. Zhai, C. Chen, L. Tao, X. Ding, Y. Miao and M. Cheng, *ACS Appl. Energy Mater.*, 2022, **5**, 13261.
55. N. J. Jeon, H. Na, E. H. Jung, T.-Y. Yang, Y. G. Lee, G. Kim, H.-W. Shin, S. I. Seok, J. Lee and J. Seo, *Nat. Energy*, 2018, **3**, 682.
56. F. Zhang, Z. Wang, H. Zhu, N. Pellet, J. Luo, C. Yi, X. Liu, H. Liu, S. Wang, X. Li, Y. Xiao, S. M. Zakeeruddin, D. Bi and M. Grätzel, *Nano Energy*, 2017, **41**, 469.

57. Y. K. Wang, H. Ma, Q. Chen, Q. Sun, Z. Liu, Z. Sun, X. Jia, Y. Zhu, S. Zhang, J. Zhang, N. Yuan, J. Ding, Y. Zhou, B. Song and Y. Li, *ACS Appl. Mater. Interfaces,* 2021, **13**, 7705.

58. H. Guo, H. Zhang, C. Shen, D. Zhang, S. Liu, Y. Wu and W.-H. Zhu, *Angew. Chem. Int. Ed.*, 2021, **60**, 2674.

59. R. Li, C. Li, M. Liu, P. Vivo, M. Zheng, Z. Dai, J. Zhan, B. He, H. Li, W. Yang, Z. Zhou and H. Zhang, *CCS Chem.*, 2022, **4**, 3084.

60. Q. Cheng, H. Chen, F. Yang, Z. Chen, W. Chen, H. Yang, Y. Shen, X.-M. Ou, Y. Wu, Y. Li and Y. Li, *Angew. Chem. Int. Ed.*, 2022, **61**, e202210613.

61. F. Wolf, M. T. Sirtl, S. Klenk, M. H. H. Wurzenberger, M. Armer, P. Dörflinger, P. Ganswindt, R. Guntermann, V. Dyakonov and T. Bein, *CrystEngComm*, 2023, **25**, 3142.

62. A. Krishna, D. Sabba, H. Li, J. Yin, P. P. Boix, C. Soci, S. G. Mhaisalkar and A. C. Grimsdale, *Chem. Sci.*, 2014, **5**, 2702.

63. Q.-Q. Ge, J.-Y. Shao, J. Ding, L.-Y. Deng, W.-K. Zhou, Y.-X. Chen, J.-Y. Ma, L.-J. Wan, J. Yao, J.-S. Hu and Y.-W. Zhong, *Angew. Chem., Int. Ed.*, 2018, **57**, 10959.

64. X.-J. Ma, X.-D. Zhu, K.-L. Wang, F. Igbari, Y. Yuan, Y. Zhang, C.-H. Gao, Z.-Q. Jiang, Z.-K. Wang and L.-S. Liao, *Nano Energy*, 2019, **63**, 103865.

65. X. Yu, D. Gao, Z. Li, X. Sun, B. Li, Z. Zhu and Z.'a. Li, *Angew. Chem. Int. Ed.*, 2023, **62**, e202218752.

66. J. Liu, Y. Wu, C. Qin, X. Yang, T. Yasuda, A. Islam, K. Zhang, W. Peng, W. Chen and L. Han, *Energy Environ. Sci.*, 2014, **7**, 2963.

67. K. Rakstys, S. Paek, P. Gao, P. Gratia, T. Marszalek, G. Grancini, K. T. Cho, K. Genevicius, V. Jankauskas, W. Pisula and M. K. Nazeeruddin, *J. Mater. Chem. A*, 2017, **5**, 7811.

68. Z. Zhu, Y. Bai, H. K. H. Lee, C. Mu, T. Zhang, L. Zhang, J. Wang, H. Yan, S. K. So and S. Yang, *Adv. Funct. Mater.*, 2014, **24**, 7357; T. Matsui, I. Petrikyte, T. Malinauskas, K. Domanski, M. Daskeviciene, M. Steponaitis, P. Gratia, W. Tress, J.-P. Correa-Baena, A. Abate, A. Hagfeldt, M. Grätzel, M. K. Nazeeruddin, V. Getautis and M. Saliba*, ChemSusChem*, 2016, **9**, 2567; Y. Kim, E. H. Jung, G. Kim, D. Kim, B. J. Kim and J. Seo, *Adv. Energy Mater.*, 2018, **8**, 1801668.

69. J. Wu, C. Liu, M. Hu, X. Deng, W. Tan, Y. Tian and B. Xu, *J. Mater. Chem. A*, 2018, **6**, 13123.

70. B. Cai, Y. Xing, Z. Yang, W.-H. Zhang and J. Qiu, *Energy Environ. Sci.*, 2013, **6**, 1480.

71. J. Lee, M. M. Byranvand, G. Kang, S. Y. Son, S. Song, G.-W. Kim and T. Park, *J. Am. Chem. Soc.*, 2017, **139**, 12175; J. Lee, T. H. Lee, M. M. Byranvand, K. Choi, H. I. Kim, S. A. Park, J. Y. Kim and T. Park, *J. Mater. Chem. A*, 2018, **6**, 5538.

72. Y. Guo, L. He, J. Guo, Y. Guo, F. Zhang, L. Wang, H. Yang, C. Xiao, Y. Liu, Y. Chen, Z. Yao and L. Sun, *Angew. Chem.*, 2022, **134**, e202114341.
73. Q. Fu, Z. Xu, X. Tang, T. Liu, X. Dong, X. Zhang, N. Zheng, Z. Xie and Y. Liu, *ACS Energy Lett.*, 2021, **6**, 1521.
74. Z. Xie, H. Park, S. Choi, H.-Y. Park, T. Gokulnath, H. Kim, J. Kim, H.-B. Kim, I. W. Choi, Y. Jo, D. S. Kim, Y.-Y. Kim, S. Y. Yoon, J. Yoon, Y.-R. Cho and S.-H. Jin, *Adv. Energy Mater.*, 2023, **13**, 2202680.
75. T. Duong, J. Peng, D. Walter, J. Xiang, H. Shen, D. Chugh, M. Lockrey, D. Zhong, J. Li, K. Weber, T. P. White and K. R. Catchpole, *ACS Energy Lett.*, 2018, **3**, 2441.
76. M. Li, Y. Li, S.-I. Sasaki, J. Song, C. Wang, H. Tamiaki, W. Tian, G. Chen, T. Miyasaka and X.-F. Wang, *ChemSusChem*, 2016, **9**, 2862.
77. J. Cao, X. Lv, P. Zhang, T. T. Chuong, B. Wu, X. Feng, C. Shan, J. Liu and Y. Tang, *Adv. Mater.*, 2018, **30**, 1800568.
78. Z. Yu, L. Wang, X. Mu, C.-C. Chen, Y. Wu, J. Cao and Y. Tang, *Angew. Chem. Int. Ed.*, 2021, **60**, 6294.
79. J. A. Christians, R. C. M. Fung and P. V. Kamat, *J. Am. Chem. Soc.*, 2014, **136**, 758.
80. X. Li, J. Yang, Q. Jiang, W. Chu, D. Zhang, Z. Zhou and J. Xin, *ACS Appl. Mater. Interfaces*, 2017, **9**, 41354.
81. N. Arora, M. I. Dar, A. Hinderhofer, N. Pellet, F. Schreiber, S. M. Zakeeruddin and M. Grätzel, *Science*, 2017, **358**, 768.
82. X. Jin, X. Lei, C. Wu, G. Jiang, W. Liu, H. Zeng, T. Chen and C. Zhu, *J. Mater. Chem. A*, 2017, **5**, 19884.
83. H. Zhang, H. Wang, W. Chen and A. K.-Y. Jen, *Adv. Mater.*, 2017, **29**, 1604984.
84. H. Chen, A. Maxwell, C. Li, S. Teale, B. Chen, T. Zhu, E. Ugur, G. Harrison, L. Grater, J. Wang, Z. Wang, L. Zeng, S. M. Park, L. Chen, P. Serles, R. A. Awni, B. Subedi, X. Zheng, C. Xiao, N. J. Podraza, T. Filleter, C. Liu, Y. Yang, J. M. Luther and E. H. Sargent, *Nature*, 2023, **613**, 676.
85. a) J. J. Kwiatkowski, J. Nelson, H. Li, J. L. Bredas, W. Wenzel and C. Lennartz, *Phys. Chem. Chem. Phys.*, 2008, **10**, 1852; b) C. Lee, R. Waterland and K. Sohlberg, *J. Chem. Theory Comput.*, 2011, **7**, 2556; c) P. Kordt, J. J. van der Holst, M. Al Helwi, W. Kowalsky, F. May, A. Badinski, C. Lennartz and D. Andrienko, *Adv. Funct. Mater.*, 2015, **25**, 1955; d) B. Baumeier, F. May, C. Lennartz and D. Andrienko, *J. Mater. Chem.*, 2012, **22**, 10971.
86. S. M. Ryno, C. Risko and J.-L. Brédas, *J. Am. Chem. Soc.*, 2014, **136**, 6421.
87. N. Karl, *Mol. Cryst. Liq. Cryst.*, 1989, **171**, 31.
88. R. A. Marcus, *Annu. Rev. Phys. Chem.*, 1964, **15**, 155.

89. A. Miller and E. Abrahams, *Phys. Rev.*, 1960, **120**, 745.
90. A. Troisi, *Chem. Soc. Rev.*, 2011, **40**, 2347.
91. H. Bässler, *Phys. Status Solidi B*, 1993, **175**, 15.
92. P. Friederich, V. Meded, A. Poschlad, T. Neumann, V. Rodin, V. Stehr, F. Symalla, D. Danilov, G. Lüdemann, R. F. Fink, I. Kondov, F. von Wrochem and W. Wenzel, *Adv. Funct. Mater.*, 2016, **26**, 5757.
93. R. Coehoorn and P. A. Bobbert, *Phys. Status Solidi A*, 2012, **209**, 2354.
94. P. Friederich, A. Fediai, S. Kaiser, M. Konrad, N. Jung and W. Wenzel, *Adv. Mater.*, **31**, 2019, 1808256.
95. P. Friederich, V. Gómez, C. Sprau, V. Meded, T. Strunk, M. Jenne, A. Magri, F. Symalla, A. Colsmann, M. Ruben and W. Wenzel, *Adv. Mater.*, 2017, **29**, 1703505.
96. J. Hachmann, R. Olivares-Amaya, A. Jinich, A. L. Appleton, M. A. Blood-Forsythe, L. R. Seress, C. Román-Salgado, K. Trepte, S. Atahan-Evrenk, S. Er, S. Shrestha, R. Mondal, A. Sokolov, Z. Bao and A. Aspuru-Guzik, *Energy Environ. Sci.*, 2014, **7**, 698.
97. K. Alberi, M. B. Nardelli, A. Zakutayev, L. Mitas, S. Curtarolo, A. Jain, M. Fornari, N. Marzari, I. Takeuchi, M. L. Green, M. G. Kanatzidis, M. F. Toney, S. Butenko, B. Meredig, S. Lany, U. Kattner, A. Davydov, E. Toberer, V. Stevanovic, A. Walsh, N.-G. Park, A. Aspuru-Guzik, D. Tabor, J. Nelson, J. Murphy, A. Setlur, J. Gregoire, H. Li, R. Xiao, A. Ludwig, L. W. Martin, A. Rappe, S.-H. Wei and J. Perkins, *J. Phys. D: Appl. Phys.*, 2018, **52**, 013001.
98. CAS SciFinder^{n}, https://www.cas.org/solutions/cas-scifinder-discovery-platform/cas-scifinder/synthesis-planning, (accessed: January 2024).
99. Reaxys®, https://www.reaxys.com/#/search/quick, (accessed: January 2024).
100. M. Sulpizi, P. Carloni, J. Hutter and U. Rothlisberger, *Phys. Chem. Chem. Phys.*, 2003, **5**, 4798.
101. P. T. van Duijnen and M. Swart, *J. Phys. Chem. A*, 1998, **102**, 2399.
102. C. Oostenbrink, A. Villa, A. E. Mark and W. F. V. Gunsteren, *J. Comput. Chem.*, 2004, **25**, 1656.
103. J. Wang, R. M. Wolf, J. W. Caldwell, P. A. Kollman and D. A. Case, *J. Comput. Chem.*, 2004, **25**, 1157.
104. J. S. Smith, O. Isayev and A. E. Roitberg, *Chem. Sci.*, 2017, **8**, 3192.
105. Y. Youn, D. Yoo, H. Song, Y. Kang, K. Yeop Kim, S. Ho Jeon, Y. Cho, K. Chae and S. Han, *J. Mater. Chem. C*, 2018, **6**, 1015.
106. V. Rühle, A. Lukyanov, F. May, M. Schrader, T. Vehoff, J. Kirkpatrick, B. Baumeier and D. Andrienko, *J. Chem. Theory Comput.*, 2011, **7**, 3335.

107. V. Rühle, C. Junghans, A. Lukyanov, K. Kremer and D. Andrienko, *J. Chem. Theory Comput.*, 2009, **5**, 3211.
108. D. M. Huang, R. Faller, K. Do and A. J. Moulé, *J. Chem. Theory Comput.*, 2010, **6**, 526.
109. P. K. Watkins, A. B. Walker and G. L. B. Verschoor, *Nano Lett.*, 2005, **5**, 1814.
110. M. J. Jurow, C. Mayr, T. D. Schmidt, T. Lampe, P. I. Djurovich, W. Brütting and M. E. Thompson, *Nat. Mater.*, 2015, **15**, 85.
111. P. Friederich, V. Rodin, F. von Wrochem and W. Wenzel, *ACS Appl. Mater. Interfaces*, 2018, **10**, 1881.
112. T. Pope, Y. Giret, M. Fsadni, P. Docampo, C. Groves and T.J. Penfold, *Organ. Electron.*, 2023, **115**, 106760.
113. V. Rodin, F. Symalla, P. Friederich, V. Meded, D. Danilov, A. Poschlad, G. Nelles, F. von Wrochem and W. Wenzel, *Phys. Rev. B*, 2015, **91**, 15.
114. F. Liu, H. van Eersel, B. Xu, J. G. E. Wilbers, M. P. de Jong, W. G. van der Wiel, P. A. Bobbert and R. Coehoorn, *Phys. Rev. B*, 2017, **96**, 205203.
115. C. Groves, *Rep. Prog. Phys.*, 2017, **80**, 026502.
116. M. Casalegno, G. Raos and R. Po, *J. Chem. Phys.*, 2010, **132**, 094705.
117. A. Massé, R. Coehoorn and P. A. Bobbert, *Phys. Rev. Lett.*, 2014, **113**, 116604.
118. B. Baumeier, O. Stenzel, C. Poelking, D. Andrienko and V. Schmidt, *Phys. Rev. B*, 2012, **86**, 184202.
119. Quantum Patch: a) P. Friederich, F. Symalla, V. Meded, T. Neumann and W. Wenzel, *J. Chem. Theory Comput.*, 2014, **10**, 3720; b) P. Friederich, V. Meded, F. Symalla, M. Elstner and W. Wenzel, *J. Chem. Theory Comput.*, 2015, **11**, 560.
120. P. Borsenberger and H. Bässler, *J. Chem. Phys.*, 1991, **95**, 5327.
121. A. Dieckmann, H. Bässler and P. Borsenberger, *J. Chem. Phys.*, 1993, **99**, 8136.

2 Theoretical Background

2.1 Introduction

This chapter gives a background to the methods used in the results chapters that follow. Section ***2.2*** begins with a brief introduction to electronic structure theory, highlighting the Schrödinger equation and the Born Oppenheimer Approximation. Hartree-Fock (HF) theory and Density Functional Theory (DFT) are two methods for finding approximate solutions to the Schrödinger equation, and are introduced in sections ***2.2.1*** and ***2.2.2***. Simulation techniques are covered next; *Ab Initio* Molecular Dynamics (AIMD), as well as Classical MD and an introduction to Force Fields in section ***2.3***, and finally kinetic Monte Carlo (kMC), with an outline of our in-house open source kMC code "CharTED-KMC"[1], given in section ***2.4***. This chapter is based mainly on the textbooks by Jensen[2], Reach[3], and Cramer[4]. The textbook by Sherrill[5] was used as an additional resource for HF theory, and Koch and Holthausen[6] for DFT. Finally, much of the kMC section ***2.4*** is taken from our publication.[7]

2.2 Electronic Structure Theory

The time-indepedent Schrödinger equation solves for the many body wavefunction ψ from which we can obtain all the information about a given system. The Schrödinger equation is given by,

$$\hat{H}\psi(\boldsymbol{r},\boldsymbol{R}) = E\psi(\boldsymbol{r},\boldsymbol{R})\,. \tag{2.1}$$

Where $\hat{H}$ is the Hamiltonian which contains all the interactions of the electrons and nuclei, and E is the energy of the system. The Schrödinger equation can only be solved exactly for a two-body problem, such as a hydrogen atom where the Hamiltonian is expanded to,

$$\hat{H} = -\sum_{i}^{n}\frac{{\nabla_{\mathrm{i}}}^2}{2} - \sum_{I}^{N}\frac{{\nabla_{\mathrm{I}}}^2}{2m_I} + \sum_{i<j}^{n}\frac{1}{\boldsymbol{r}_{ij}} + \sum_{I<J}^{N}\frac{q_I q_J}{\boldsymbol{R}_{IJ}} - \sum_{i}^{n}\sum_{I}^{N}\frac{q_I}{\boldsymbol{r}_{iI}} \tag{2.2}$$

and where the nuclei, N, run over I and J, while the electrons n, run over i and j, and m is the mass of the nuclei and q is the charge. In order from left to right, the first two terms represent the kinetic energy of the electrons and nuclei, respectively, and the last three terms the potential energy due to the repulsive and attractive interactions.

To obtain a solution for a many-body system, approximations are necessary. Since electrons are much lighter and faster than nuclei, the dynamics of the nuclei and electrons can be decoupled, with the nuclear positions considered fixed. This "clamped nuclei" representation is the basis for the Born-Oppenheimer approximation which allows us to solve the Schrödinger equation for the electrons for a given nuclear configuration.[8] The Hamiltonian in (2.1) and (2.2) can then be simplified to the electronic Hamiltonian, $\widehat{H_e}$, which consists of the electronic terms, the kinetic energy term, and the potential energy terms, i.e. the electron nuclei attraction, and the electron-electron repulsion,

$$\widehat{H}_e \psi_e(\boldsymbol{r}; \boldsymbol{R}) = E_e \psi_e(\boldsymbol{r}; \boldsymbol{R}) \tag{2.3}$$

$$\widehat{H}_e = -\sum_i^n \frac{\nabla_{\mathrm{i}}{}^2}{2} + \sum_{i<j}^n \frac{1}{\boldsymbol{r}_{ij}} - \sum_i^n \sum_I^N \frac{q_I}{\boldsymbol{r}_{iI}} \,. \tag{2.4}$$

Since the positions of the nuclei are fixed, the kinetic energy term of the nuclei falls away and the nuclear repulsive interaction term is a constant which does not affect the electronic wavefunction. For all but the simplest cases, only an approximate solution to the electronic Schrödinger equation (2.3) can be found, as the exact electron interaction term becomes an intractable problem in many-body systems. Hartree-Fock and DFT are methods that allow us to find an approximate solution for the Schrödinger equation.

2.2.1 Hartree-Fock Theory

Hartree-Fock theory solves the many-body wavefunction using a mean-field model. The electron kinetic energy term and the electron-nuclei coulomb attraction term are the separable components of equation (2.4), which may be incorporated into a single term so that the electronic Hamiltonian can be written as,

$$\widehat{H}_e = -\sum_i^n h(\boldsymbol{i}) + \sum_{i<j}^n \frac{1}{\boldsymbol{r}_{ij}} \,. \tag{2.5}$$

As we shall see later, the electron repulsion term is not easily separable for each electron in the system, so a mean field approach is used in which each electron experiences the average field due to the average positions of all other electrons.

In the one-electron Schrödinger equation,

$$\hat{h}_i \chi_i = \epsilon_i \chi_i \tag{2.6}$$

the electron spin orbital wavefunction is the product of the spatial and spin function,

$$\chi(\boldsymbol{x}) = \varphi(\boldsymbol{r})\sigma(\boldsymbol{s}) \tag{2.7}$$

$$\boldsymbol{s} = \boldsymbol{\alpha}, or\ \boldsymbol{\beta} \tag{2.8}$$

where each electron has 3*N* spatial degrees of freedom and where the spin orbital, $\boldsymbol{s}$, may be spin up ($\boldsymbol{\alpha}$) or spin down ($\boldsymbol{\beta}$)

The Hartree product, ψ_{HP}, is therefore the sum of the spin orbital wavefunctions,

$$\psi_{HP}(\boldsymbol{x}_1, \boldsymbol{x}_2, \dots, \boldsymbol{x}_N) = \chi_1(\boldsymbol{x}_1), \chi_2(\boldsymbol{x}_2), \dots, \chi_N(\boldsymbol{x}_N) \tag{2.9}$$

However, to satisfy the anti-symmetry principle, i.e., that no two fermions can have the same quantum number (space-spin coordinates), Slater determinants are used. The Slater determinant describes the total wavefunction of a system as a product of its single electron antisymmetric spin orbital wavefunctions $\chi(\boldsymbol{x})$,

$$\psi_{SD}(\boldsymbol{x}_1, \boldsymbol{x}_2, \dots, \boldsymbol{x}_N) = \frac{1}{\sqrt{N!}} \begin{vmatrix} \chi_1(\boldsymbol{x}_1) & \chi_2(\boldsymbol{x}_1) & \cdots & \chi_N(\boldsymbol{x}_1) \\ \chi_1(\boldsymbol{x}_2) & \chi_2(\boldsymbol{x}_2) & \cdots & \chi_N(\boldsymbol{x}_2) \\ \vdots & \vdots & \ddots & \vdots \\ \chi_1(\boldsymbol{x}_N) & \chi_2(\boldsymbol{x}_N) & \cdots & \chi_N(\boldsymbol{x}_N) \end{vmatrix} \tag{2.10}$$

Since the exact wavefunction of a system is not known, trail wavefunctions are generated from the Hartree-Fock wavefunction, which takes the form of the Slater determinant in (2.10) above, ψ_{SD}. Using the variation theorem, parameters are adjusted to minimise the energy of the system and arrive at an approximate solution to the Schrödinger equation. This is expressed by,

$$\delta E_{HF} = \langle \psi_{SD} | \hat{H} | \psi_{SD} \rangle \tag{2.11}$$

The Hartree-Fock energy is then given by,

$$E_{HF} = \sum_{i}^{n} \hat{h}_i + \frac{1}{2}\sum_{i}^{n}\sum_{j}^{n}(\hat{J}_{ij} - \hat{K}_{ij}) \tag{2.12}$$

where kinetic energy is given by,

$$\hat{h}_i = \int \chi_i{}^*(\boldsymbol{x})\left[-\frac{\nabla_i{}^2}{2} - \frac{q_I}{\boldsymbol{r}_{iI}}\right]\chi_i(\boldsymbol{x})d\boldsymbol{x} \tag{2.13}$$

The electron-electron Coulomb repulsion is given by,

$$\hat{J}_{ij} = \iint |\chi_i(\boldsymbol{x}_1)|^2 \frac{1}{\boldsymbol{r}_{12}} |\chi_j(\boldsymbol{x}_2)|^2 d\boldsymbol{x}_1 d\boldsymbol{x}_2 \tag{2.14}$$

and electron-electron exchange integral, arising from the anti-symmetry principle, and is given by,

$$\hat{K}_{ij} = \iint \chi_i{}^*(\boldsymbol{x}_1)\chi_j{}^*(\boldsymbol{x}_1)\frac{1}{\boldsymbol{r}_{12}}\chi_i(\boldsymbol{x}_2)\chi_j(\boldsymbol{x}_2)d\boldsymbol{x}_1 d\boldsymbol{x}_2 \tag{2.15}$$

The single-electron Hartree Fock equations are given by,

$$\hat{f}_i\chi_i = \epsilon_i\chi_i \tag{2.16}$$

where ϵ_i and χ_i correspond to the energy and spin orbital wavefunctions, respectively, of the different electronic states of the system, reducing the many-body Schrödinger equation (2.1) to n single-electron equations. Solving the HF equations for the minimum energy state allows us to find the best approximate wavefunction of the system. The Fock operator, $\hat{f}_i$, in (2.16) is given by,

$$\hat{f}_i = -\frac{\nabla_{\mathrm{i}}{}^2}{2} + \sum_{I}^{n}\frac{q_I}{\boldsymbol{r}_{iI}} + \hat{V}_{HF} \tag{2.17}$$

which includes the electron kinetic energy term and the Coulomb attraction term, and in which electron-electron interactions are approximated by the Hartree-Fock potential, V_{HF}, which is the average field felt by the electron due to the $n-1$ remaining electrons. This reduces the two-electron operator to a one electron operator,

$$\hat{V}_{HF} = \sum_{i}^{n}(\hat{J}_i - \hat{K}_i) \tag{2.18}$$

that includes the classical Coulomb repulsion term,

$$\hat{J}_i f(\boldsymbol{x}) = \sum_i^n \int |\chi_i(\boldsymbol{x}_2)|^2 \frac{1}{\boldsymbol{r}_{12}} f(\boldsymbol{x}_1) d\boldsymbol{x}_2 \tag{2.19}$$

and the exchange integral, which is the due to the anti-symmetry principle,

$$\hat{K}_i f(\boldsymbol{x}) = \sum_i^n \int \chi_i{}^*(\boldsymbol{x}_2) \frac{1}{\boldsymbol{r}_{12}} \chi_i(\boldsymbol{x}_1) f(\boldsymbol{x}_1) d\boldsymbol{x}_2 \tag{2.20}$$

The Hartree-Fock energy is solved using a self-consistent field (SCF) procedure, in which the initial wavefunction is guessed and the energy is minimised through iterative cycles, as described above, until a convergence threshold is achieved. Hartree-Fock theory forms the foundation for more complex theoretical methods. Nevertheless, Hartree-Fock methods suffer from electron correlation errors as it only accounts for electron exchange. Using a mean-field approach, results in instantaneous electron-electron repulsions being neglected (dynamic correlation), while the use of a single Slater determinant is not appropriate in cases where the ground state is best described by more than one quasi-degenerate determinant (static correlation).

2.2.2 Density Functional Theory

According to the Hohenberg-Kohn theorems, all the ground-state properties of a system can be determined by the corresponding ground state electron density.[9] Therefore, DFT approximates the solution for the many-body Schrödinger equation using the electron density. The Hohenberg-Kohn-Sham formulation of DFT maps the interacting *N*-electron system onto a *N* non-interacting electron system, coupled through the Kohn-Sham effective potential.[10] This way the many-body problem can be approximated by a many single body problems and the electron density can be solved in terms of the wavefunctions of single electrons.

The first Hohenberg-Kohn theorem states that the external potential, $\hat{V}_{Ne}$, is a unique functional of the ground-state electron density. This means that the electron density determines all the properties of the system including the total energy. The proof is based on *reductio ad absurdum*.

Consider two systems with distinct external potentials, Hamiltonians, wavefunctions, and ground-state energies, $E_1 \neq E_2$, but the same ground-state electron density, $\rho(\mathbf{r})$,

$$\hat{V}_1 \Rightarrow \hat{H}_1 \Rightarrow \Psi_1 \;\Rightarrow\; \rho(\mathbf{r}) \;\Leftarrow \Psi_2 \Leftarrow \hat{H}_2 \;\Leftarrow \hat{V}_2 \,. \tag{2.21}$$

We can use Ψ_2 to solve for $\hat{H}_1$. Applying the variation principle, it then follows that,

$$E_1 = \langle \Psi_1 | \hat{H}_1 | \Psi_1 \rangle < \langle \Psi_2 | \hat{H}_1 | \Psi_2 \rangle \,, \tag{2.22}$$

and therefore,

$$E_1 < \langle \Psi_2 | \hat{H}_1 | \Psi_2 \rangle = \langle \Psi_2 | \hat{H}_2 | \Psi_2 \rangle + \langle \Psi_2 | \hat{H}_1 - \hat{H}_2 | \Psi_2 \rangle \,. \tag{2.23}$$

Since the only difference between the two Hamiltonians is their external potentials, this may be written as,

$$E_1 < E_2 + \int \rho(\boldsymbol{r})[V_1(\boldsymbol{r}) - V_2(\boldsymbol{r})]\, d\boldsymbol{r} \,. \tag{2.24}$$

However, using Ψ_1 to solve for H_2 we arrive at,

$$E_2 < E_1 + \int \rho(\boldsymbol{r})[V_2(\boldsymbol{r}) - V_1(\boldsymbol{r})]\, d\boldsymbol{r} \,, \tag{2.25}$$

and the sum of these inequalities gives the contradictory relation,

$$E_1 + E_2 < E_2 + E_1 \,. \tag{2.26}$$

Therefore, the first Hohenberg-Kohn theorem is determined to be true since the assumption that it is false is invalid. The ground-state electron density, $\rho(\mathbf{r})$ has been shown to determine the external potential and all the properties of the system, so we can write the energy as a functional of the density,

$$E[\rho] = T_e[\rho] + V_{ee}[\rho] + V_{Ne}[\rho] \,. \tag{2.27}$$

Where T is the kinetic energy term, V_{ee} is the electron-electron interaction term, and V_{Ne} is the nuclear-electron term, i.e., the external potential.

The second Hohenberg-Kohn theorem states that the correct ground state energy, i.e., the minimised total energy state, of a system is a functional only of the true ground state electron density ρ, and an approximation may be arrived at starting from a trial density, $\tilde{\rho}$ by using the minimisation principle,

$$E[\tilde{\rho}] \geq E[\rho] \,. \tag{2.28}$$

Therefore, the Hohenberg-Kohn theorems show that all the properties of a system may be arrived at from the exact functional of the density, which can, however, only ever be approximated.

Expressing the electronic Hamiltonian,

$$\hat{H}_e = \hat{T}_e + \hat{V}_{ee} + \hat{V}_{Ne} + \left(\hat{V}_{NN}\right), \tag{2.29}$$

in terms of the electron density, gives us the following expression for the external potential term,

$$\hat{V}_{Ne} = \int \rho(\boldsymbol{r}) V(\boldsymbol{r})\, d\boldsymbol{r}\,, \tag{2.30}$$

and the Coulombic repulsion term $\hat{V}_{ee}$,

$$J[\rho] = \frac{1}{2}\iint \frac{\rho(\boldsymbol{r})\rho(\boldsymbol{r}')}{|\boldsymbol{r}-\boldsymbol{r}'|} d\boldsymbol{r} d\boldsymbol{r}'\,. \tag{2.31}$$

However, in so doing, the electron-electron exchange and correlation interactions are neglected. At the same time, the kinetic energy term, $\hat{T}_e$, cannot easily be expressed in terms of the electron density.

The Hohenberg-Kohn-Sham formulation of DFT maps the interacting *N*-electron system onto *N* non-interacting electron systems coupled through the Kohn-Sham effective potential. In Kohn-Sham density functional theory the energy of a system is given by the universal density functional of the true interacting system. Like in Hartree-Fock theory, this non-interacting system is the product of its single electron antisymmetric spin orbital wavefunctions $\varphi_i(x)$, described as a Slater determinant,

$$\rho(\boldsymbol{r}) = \sum_i |\varphi_i(\boldsymbol{x})|^2\,, \tag{2.32}$$

and the antisymmetric ground-state wavefunction gives the kinetic energy of the non-interacting system,

$$T[\rho] = \sum_i \left\langle \varphi_i \middle| \frac{\nabla^2}{2} \middle| \varphi_i \right\rangle\,. \tag{2.33}$$

Taking these terms $(2.30 - 2.33)$ together, the Kohn-Sham energy is then given by,

$$E_{KS}[\rho] = T[\rho] + J[\rho] + \int \rho(\boldsymbol{r}) V(\boldsymbol{r}) + E_{xc}[\rho]\,, \tag{2.34}$$

where the exchange-correlation functional, $E_{xc}[\rho]$, incorporates the difference in kinetic energy between the actual and theoretical (non-interacting) systems, as well as the difference between actual electron-electron and the simplified Coulomb interaction energies. The exact exchange-correlation functional $E_{xc}[\rho]$ cannot be known and must be approximated $(2.36 - 2.42)$, as we shall see later. The functional derivative of the exchange correlation potential is given by V_{xc}. The Kohn-Sham equations,

$$\left[-\frac{\nabla^2}{2}+\frac{1}{2}\int\frac{\rho(\boldsymbol{r}')}{|\boldsymbol{r}-\boldsymbol{r}'|}d\boldsymbol{r}'+V(\boldsymbol{r})+V_{xc}(\boldsymbol{r})\right]\varphi_i(\boldsymbol{r})=\epsilon_i\varphi_i(\boldsymbol{r})\,, \tag{2.35}$$

are solved until the Kohn- Sham orbital energy has converged using self-consistent cycles.

The exchange-correlation energy density, $E_{xc}\big(\rho(\boldsymbol{r})\big)$, at a given position $\boldsymbol{r}$, is dependent on the density at all other points. The power in this approach resides in the fact that comparable simple approximations to the exchange and correlation term are able to map the non-interacting system upon a form closer to the correct many body wavefunction. Most approximate exchange-correlation functionals that exist today are based on the local density approximation (LDA). The non-homogenous system is conceptualised as a unform electron gas in which the electrons travel within an infinite space that has a uniform positive background potential, so that the system has an overall neutral charge,

$$E_{xc}^{LDA}[\rho]=\int\rho(\boldsymbol{r})e_{xc}\big(\rho(\boldsymbol{r})\big)d\boldsymbol{r}\ . \tag{2.36}$$

The local exchange-correlation energy density now depends only on local density, and the exchange and correlation energy density contributions can be separated,

$$E_{xc}\big(\rho(\boldsymbol{r})\big)=E_x\big(\rho(\boldsymbol{r})\big)+E_c\big(\rho(\boldsymbol{r})\big)\,. \tag{2.37}$$

Using Hartree-Fock theory, the exchange energy of an electron in a uniform electron gas,

$$E_x\big(\rho(\boldsymbol{r})\big)=\frac{3}{4}\left(\frac{3}{\pi}\right)^{1/3}\rho(\boldsymbol{r})^{4/3}\,, \tag{2.38}$$

allows us to arrive at the exchange potential, given by,

$$V_x^{LDA}(\boldsymbol{r})=\left(\frac{3}{\pi}\right)^{1/3}\rho^{1/3}(\boldsymbol{r})\,. \tag{2.39}$$

The local density approximation functionals perform well for systems in which the density changes slowly over space, such as single atoms and metallic solids.[11] However, it is too crude for many other applications, as most molecules don't have a uniform density and atoms and molecules are often characterised by rapidly changing electron densities. The generalised gradient approximation addresses this problem by including the electron density gradient at each point within the exchange-correlation functional, which is expressed as,

$$E_{xc}^{GGA}[\rho]=\int f\big(\rho(\boldsymbol{r})\nabla\rho(\boldsymbol{r})\big)d\boldsymbol{r}\ . \tag{2.40}$$

GGA functionals provide a substantial improvement in the accuracy of calculations over LDA, while remaining computationally inexpensive, with PBE and BYLP are perhaps the best know examples of GGA functionals.[12,13]

DFT suffers from self-interaction error in which the self-interaction term, due the electron interacting with itself, is not fully cancelled out by the approximate exchange term, resulting in an underestimation of the energy.[14] In HF the exchange terms and the Coulomb term cancel out so that there is no self-interaction. Hybrid functionals, such as PBE0, mix the 'exact' Hartree-Fock exchange energy with the DFT exchange energy to improve the accuracy of calculations even further,

$$E_{xc}^{hybrid} = aE_x^{HF} + (1-a)E_x^{DFT} + E_c^{DFT} . \tag{2.41}$$

The PBE0 functional[15] uses 25% Hartree–Fock exchange energy with 75% Perdew–Burke-Ernzerhof (PBE) exchange energy and PBE correlation energy,

$$E_{xc} = \frac{1}{4}E_X(HF) + \frac{3}{4}E_x(PBE) + E_c(PBE) . \tag{2.42}$$

While increasingly complex functionals deliver increased chemical accuracy, there is no functional that is universally appropriate, and it is not always easy to predict which functional would be the most suitable.[16]

2.3 Molecular Dynamics

Molecular dynamics (MD) are a type of simulation method, first devised in the 1950s to model the movement of atoms and molecules over time.[17] Each step within an MD simulation involves setting up the potential energy surface (PES) by calculating the energies and forces acting within the system, and then using this to solve the equations of motion. Classical MD neglects the quantum mechanical description of chemical systems, and the chemical system is represented as a 'ball and stick' model which follows the laws of classical mechanics. *Ab initio* MD (AIMD), takes the quantum nature of the electrons into account to construct a PES by solving the electronic Schrödinger equation using DFT or wavefunction methods.

In MD atoms are treated as hard spheres, with a given mass m, the dynamics of which can be simulated by solving Newton's second law of motion,

$$-\frac{dV}{d\boldsymbol{r}} = \boldsymbol{F} = m\boldsymbol{a} = m\frac{d^2\boldsymbol{r}}{dt^2}\,, \tag{2.43}$$

where V is the potential energy at position r which contains the Cartesian coordinates of the particles.

Using a Maxwell-Boltzmann distribution of kinetic energies, the atoms in the system are randomly assigned their velocities, and their positions $\boldsymbol{r}$ after a sufficiently small time-step t is found. The Taylor expansions of the forward and backward time steps,

$$\boldsymbol{r}(t+\delta t) = \boldsymbol{r}(t) + \delta\boldsymbol{v}(t) + \frac{1}{2}\frac{\boldsymbol{f}(t)}{m}\delta t^2 + \boldsymbol{O}(\delta^3) \tag{2.44}$$

$$\boldsymbol{r}(t-\delta t) = \boldsymbol{r}(t) - \delta\boldsymbol{v}(t) + \frac{1}{2}\frac{\boldsymbol{f}(t)}{m}\delta t^2 + \boldsymbol{O}(\delta^3) \tag{2.45}$$

are added to derive the Verlet algorithm[18],

$$\boldsymbol{r}(t+\delta t) = 2\boldsymbol{r}(t) - \boldsymbol{r}(t-\delta t) + \frac{\boldsymbol{f}(t)}{m}\delta t^2\,. \tag{2.46}$$

At the start of the calculation, before the Verlet algorithm is triggered, the initial preceding position vector,$\boldsymbol{r}_{-1}$, is required. This is not available using the algorithm but can be estimated as follows,

$$\boldsymbol{r}_{-1} = \boldsymbol{r}_0 - \boldsymbol{v}_0\Delta t\,. \tag{2.47}$$

After the positions are found, the acceleration of the particles is calculated, using the force field, to compute their trajectory,

$$\boldsymbol{v}(t) = \frac{\boldsymbol{r}(t+\delta t) - \boldsymbol{r}(t+\delta t)}{2\delta t} \,. \tag{2.48}$$

While the Verlet algorithm gives high position accuracy, the velocities are less accurate and out of phase with the position by half a time step. The Velocity-Verlet is a commonly used algorithm, including in the LAMPPS MD[19] and Orca AIMD[20] packages, and avoids this issue by explicitly incorporating the acceleration into the equations for propagating the particles.[21]

2.3.1 Classical Force Fields

As mentioned above, the energies and forces acting within the system must be calculated at each step of the MD simulation. For classical MD, the electrons are replaced by springs and these properties are estimated using a force field (FF). In classical FFs, the system is conceptualised using a "ball and spring" model. Commonly used FFs for MD simulations include AMBER[22], and CHARMM[23]. The force field represents the potential energy of the system and is given as the sum of intra- and inter-molecular potentials,

$$V = V_{inter} + V_{intra} \,. \tag{2.49}$$

The intramolecular component includes the various contortions a molecule can undergo; bond stretching, angle bending, and dihedral rotation (torsion),

$$V_{intra} = \sum V_{bond} + \sum V_{angle} + \sum V_{tors} \,, \tag{2.50}$$

and the intermolecular (or non-bonded) terms consist of the long-range electrostatic and short-range van der Waals interactions,

$$V_{inter} = V_{vdw} + V_{el} \,. \tag{2.51}$$

The way these individual terms are treated depends upon the FF used. For our classical MD simulations, classical force fields with bespoke force constants were developed using the modified Seminario approach[24], based on the Cartesian Hessian matrix obtained from DFT (PBE0/def2-tzvp)[12,15,25] optimised ground state configurations of our molecules using the ORCA quantum chemistry package[20]. Dihendrals (torsional angles) were taken from the QM Hessian converted to internal coordinates.

Using the modified Seminario method, bond stretching and angle bending force constants are obtained directly from the QM Hessian matrix of the geometrically optimised molecule.[24] In so doing, this method avoids the problem of interdependency between the different components of the force field of the original Seminario method. In the original method, bond stretching force constants are estimated by projecting the forces felt by an atom due to the displacement of its neighbour onto their mutual bond vector. Angle bending force constants are treated as the linear combination of their perpendicular bond vectors. In larger molecules this results in double counting and an overestimation of the stiffness the molecule. This is because displacing one atom deforms multiple angles, but the energy change and angle force constant in the original Seminario method is only attributed to one angle. In the modified Seminario method, the chemical environment of atoms are taken into account when the bond and angle force constants are calculated. Seminario angle force constants are rescaled to account for the average energy contribution of neighbouring angle changes. The modified Seminario method results in a higher level of accuracy in QM normal mode frequencies generated, without the need for empirical data or iterative fitting of the MM Hessian matrix, while using the bond stretching force constants results in a similar level of accuracy to standard force fields for a variety of small organic molecules.

The form of our FF is given as,

$$V = \sum_{bonds} k_b(r - r_0)^2 + \sum_{angles} k_a(\theta - \theta_0)^2 + \sum_{dihedrals} k_d[1 + cos(\phi - \phi_0)]^2 + \sum_{inter} S(r) \cdot \left[4\epsilon\left(\left(\frac{\sigma}{r}\right)^{12} - \left(\frac{\sigma}{r}\right)^{6}\right) + \left(\frac{C}{\epsilon} \cdot \frac{q_i q_j}{r}\right)\right], \quad (2.52)$$

where the intramolecular components are described in terms of the bond length, r, the bond angle, θ, the dihedral angle, ϕ, and the respective spring constants, k. The improper angle rotation component of the tortional term is omitted for brevity. The intermolecular (non-bonded) point charge interaction potentials,

$$S(r) = \begin{cases} 1 & r < r_{in} \\ \dfrac{(r_{out}^2 - r^2)^2\left(r_{out}^2 + 2r^r - 3r_{in}^2\right)}{\left(r_{out}^2 - r_{in}^2\right)^3} & r_{in} < r < r_{out} \\ 0 & r > r_{out} \end{cases}, \quad (2.53)$$

are given by the inner and outer cut-off radii, r_{in} and r_{out}; the Lennard Jones potential for the van der Waals interactions is given by the user-defined atomic constants, ϵ and σ; and the electrostatic component is given by a Coulombic potential which includes the cut-off constant, C.

2.3.2 Ab initio Molecular Dynamics (AIMD)

In MD, the gradient of the potential energy V of the particles in the system is used to calculate the positions and velocities of the next time step. In AIMD, DFT or wavefunction methods are used to obtain the electronic structure of the system by solving the electronic Schrödinger equation. The energy of the system minimised with respect to the wavefunction at each time step and from this the interaction energies are calculated. The Hellman-Feynman theorem[26] states that the derivative of the energy eigenvalue with respect to the forces acting on the atoms can be expressed in terms of the expectation value of the derivative of the Hamiltonian with respect to the same parameter,

$$\frac{\delta E}{\delta R} = \left\langle \Psi_k \middle| \frac{\widehat{H}}{\delta R} \middle| \Psi_k \right\rangle . \tag{2.54}$$

In AIMD this relationship can be used to approximate the forces acting on the atoms. The wavefunction must be tightly converged at each time step to fulfil the law of energy conservation over the course of the simulation. AIMD is far more computationally expensive than classical MD and is limited to smaller systems and shorter timescales, however, it is useful when greater accuracy is required such as in simulating the conformational changes of molecules over time.

2.4 Kinetic Monte Carlo and CharTED-KMC

Monte Carlo methods, also known as multiple probability simulations, make use of random input sampling to predict possible outcomes. Kinetic Monte Carlo (kMC) is a subset of this method, which tracks the dynamic evolution of a system from one state to another, based on the associated probability distributions of these pathways, and is therefore useful for simulating random walk (Markov chain) processes.

CharTED-KMC[1] in-house kinetic Monte Carlo code, developed by Thomas Pope, Yvelin Giret and Thomas J. Penfold, specifically focuses upon modelling charge transport in organic semiconductors. In the context of the present thesis, its functionality includes careful tuning of the correlated energetic disorder strength, including the relative orientation of dipoles, from random to perfectly anti-ferroelectric with respect to each other.[6] When dipoles are randomly oriented, the correlated disorder increases linearly with the magnitude of the dipole moment. Assuming that sites are energetically discrete neglects charge delocalisation, which occurs when electronic couplings are large and comparable to energetic disorder. Oversimplifying dipole orientation and electronic coupling effects can, therefore, lead to an underestimation of the mobility. Therefore, a model for simulating charge transport in semi-ordered systems was developed.

Treating the correlated and uncorrelated energetic disorder explicitly enables us to investigate the effect of the dipole moment on the mobility separately. For each system studied, the magnitude of the dipole moment is kept constant between sites. However, the rotational degrees of freedom are varied by altering the azimuthal ϕ and polar φ angles. To randomise the dipole directions, we first draw two values from a normalised distribution which are then used to calculate each of the angles. The polar angle is restricted by an order parameter α, which limits the extent of deviation possible from fully antiferroelectric symmetry. When α = 1, dipoles on neighbouring sites are aligned to the same axis and point in opposite directions to one another. The order parameter can be tuned along a continuum up to α = 0, where fully random orientation of site dipoles is obtained.

Charge hopping between sites is a first order process, where the probability for a hop to occur increases exponentially over time. The probability that a charge remains on a given site for a time, t, is given by,

$$p_{survival}(t) = exp(-k_{tot}t)\,. \tag{2.55}$$

Therefore, the hopping probability at time t, $p_{hop}(t)$ is,

$$p_{hop}(t) = 1 - p_{survival}(t) = 1 - exp(-k_{tot}t)\,. \tag{2.56}$$

In the kMC simulation, the HTM is simulated via a representative grid, with each grid site representing an HTM hopping site (HTM molecule/dimer). The energy of each grid site calculated, and holes are randomly distributed onto the grid points at the selected hole density. Under an applied electric field, holes move across the grid via sequential probabilistically chosen hopping events between neighbouring sites that take place over a series of time steps.

For a given hopping event, all neighbouring grid sites are identified, and the rate of hopping to each of these sites is calculated using the appropriate rate equation, such as the Marcus rate equation[27].

The hopping rates, k_i, are probabilistically weighted, by calculating the cumulative rate for each hopping event (2.57). In so doing, higher rate pathways are more likely to be chosen. For an event, j, the cumulative rate, s_j, is given by,

$$s_j = \sum_{i}^{j} k_i\ . \tag{2.57}$$

An event is selected by randomly drawing a number, η, uniformly distributed between zero and s_N, where s_N is the cumulative sum of all N possible hopping events. The event, j, with rate k_j is chosen when,

$$s_{j-1} < \eta < s_j\,. \tag{2.58}$$

The charge is moved onto the new site and the grid is updated. To update the system time, a random number, ζ, uniformly distributed between zero and one is drawn, and the time step for the hopping event, t_{hop}, is calculated,

$$t_{hop} = -\frac{ln\zeta}{s_N}\,, \tag{2.59}$$

and added to the clock. At this point, the kMC loop starts again for the newly updated grid and is repeated until the number of requested steps is fulfilled. The cumulative sum of the hopping time steps gives the total time, t_{tot}, for the simulated charge hopping pathway through the grid and is used to calculate the charge mobility.

The direction of each of the hops is found, taking the electric field gradient as a reference, and by subtracting all backward from forward hopping events the carrier flux, Φ, for a given run is calculated.

For each experiment, several simulation runs are carried out. While input parameters remain constant, simulations evolve via different pathways, due to different grid starting configurations and random sampling at each step, yielding a spread of results. Experimental results are considered reliable when the overall carrier flux has a non-zero average and obeys a Gaussian distribution, so that the Random Walk Overlap (RWO) is close to zero. This is found by comparing the results with a zero average 1-D random walk with a distribution width of $\sqrt{N_{steps}}/2$, where N_{steps} is the number of steps taken.

After finding the average carrier flux, Φ, the average charge mobility, μ, is found using,

$$\mu = \frac{1}{E_{field}} \cdot \frac{1}{N_{chrg}} \cdot \frac{\Phi}{t_{tot}} , \tag{2.60}$$

where N_{chrg} is the number of charged particles and E_{field} is the applied electric field. The current for a grid of dimensions N_x, N_y and N_z with a lattice spacing, L, is given by,

$$J = \frac{1}{N_x} \cdot \frac{1}{N_y} \cdot \frac{1}{N_z} \cdot \frac{1}{L^2} \cdot \frac{\Phi}{t_{tot}} . \tag{2.61}$$

At the start of a simulation, a periodic cubic lattice of grid points is set up, with given dimensions and lattice spacing. Next the site energies of each grid point are found,

$$E_{\boldsymbol{i}}^{site} = E_{HOMO} + E_{\boldsymbol{i}}^{unc} + E_{\boldsymbol{i}}^{corr} + E_{\boldsymbol{i}}^{field} . \tag{2.62}$$

The E_{HOMO} parameter is a pre-selected input for the simulation. $E_{\boldsymbol{i}}^{field}$ is the component of the site energy due to the electric field strength felt at its position in the y-direction of the lattice, i.e., parallel to the direction of the electric field, and is calculated from the pre-selected electric field and lattice spacing inputs. Next, uncorrelated and correlated energetic disorder are added to each site.

For each grid point, the spatially uncorrelated energetic disorder, $E_{\boldsymbol{i}}^{unc}$, is added, based on a site energy drawn randomly[28] from a Gaussian density of states, of mean E_{HOMO}, and an assigned noise width of σ_{unc},

$$g(\varepsilon) = \frac{1}{\sqrt{2\pi}} \cdot \frac{1}{\sigma_{unc}} e^{-\varepsilon/2\sigma_{unc}^2} . \tag{2.63}$$

In the context of hole hopping through HOMO sites on adjacent molecules within an HTM film, E_i^{unc} reflects the energetic spread of HOMO levels within the film due to the variation in conformation of constituent molecules.

The correlated disorder, E_i^{corr}, represents the electrostatic energy component due to the interaction between the permanent dipole moment on the site, d, and those of its neighbouring sites set at a distance mapped by the spatial vector, R. For site i with neighbour j, the correlated disorder[29] on site i is given by,

$$E_i^{corr} = -\frac{1}{\epsilon_r}\sum_{j\neq i}\frac{\boldsymbol{d_j}\cdot\boldsymbol{R_{ij}}}{\left|\boldsymbol{R_{ij}}\right|^3} \ . \tag{2.64}$$

The number of neighbouring sites included in the calculation is based on a test simulation, where the number of sites is increased until results are found to converge. The dipole magnitude is a pre-selected input parameter and set as constant between all sites. The orientation of the dipoles on each site is then found. This is achieved by first drawing two random numbers from a uniform distribution between 0 and 1, to obtain the variables r_ϕ and r_φ. These are then used to define the azimuthal, $\cos\phi = (2r_\phi - 1)$, and polar, $\varphi = 2\pi\,(1-\alpha)\,r_\varphi$, angles, respectively, where the polar angle is restricted by the order parameter, α. The order parameter allows us to tune the randomness in orientation, from a fully disordered ($\alpha = 0$) to a fully ordered system ($\alpha = 1$) where all dipoles are oriented antiferroelectric to one another. Using an arbitrary orthonormal frame of reference, which is different for each simulation, defined by p_1, p_2 and p_3, the dipole vector is given by,

$$\widehat{\boldsymbol{d}}_{\boldsymbol{n}} = C_{\boldsymbol{n}}^{\pm}(sin\varphi cos\phi\boldsymbol{p_1} + sin\varphi sin\phi\boldsymbol{p_2} + cos\varphi\boldsymbol{p_3}) \ , \tag{2.65}$$

where $C_{\boldsymbol{n}}^{\pm}$ is a corrugation to reflect the antiferroelectric nature of the underlying structure.

The interaction of a charge on a site $\boldsymbol{n}$, with its neighbouring permanent dipoles on the cubic grid is given by,

$$e_{\boldsymbol{n}} = \frac{d}{\epsilon_r L^2}\cdot\frac{\widehat{\boldsymbol{n}}\cdot\widehat{\boldsymbol{d}}_{\boldsymbol{n}}}{|\boldsymbol{n}|^2} \ . \tag{2.66}$$

Where L is the lattice spacing, and n is a triple lattice vector with its unit vector $\widehat{\boldsymbol{n}}$.

The site energies have a variance[30] given by,

$$\sigma_{corr}^2 = \langle E^2\rangle - \langle E\rangle^2 \tag{2.67}$$

where the average site energy,

$$\langle E\rangle = \sum_{\boldsymbol{n}}\langle e_{\boldsymbol{n}}\rangle = 0 \ , \tag{2.68}$$

averages to zero due to the underlying ferroelectric structure of the grid points, and the second order term,

$$\langle E^2 \rangle = \sum_{\boldsymbol{n},\boldsymbol{n}'} \langle e_{\boldsymbol{n}} e_{\boldsymbol{n}'} \rangle \ , \tag{2.69}$$

has the cross terms $\boldsymbol{n} \neq \boldsymbol{n}'$, and the diagonal terms, $\boldsymbol{n} = \boldsymbol{n}'$. The sum of the distribution of the diagonal terms is, therefore, given by,

$$\sum_{\boldsymbol{n}} \langle e_{\boldsymbol{n}}^2 \rangle = \ d_0^2 \cdot d^2 \ , \tag{2.70}$$

so that the zero-order noise width is given by,

$$\sigma_0 = d_0 \cdot d \tag{2.71}$$

where d_0 is the zero-order dipole constant,

$$d_0 = 2.3475 \cdot \frac{1}{\epsilon_r L^2} \ . \tag{2.72}$$

The cross-terms for a non-random system are collected in,

$$X_\alpha = -\frac{1}{2.3475^2} \sum_{\boldsymbol{n},\boldsymbol{n}'} \langle e_{\boldsymbol{n}} e_{\boldsymbol{n}'} \rangle \tag{2.73}$$

so that,

$$\sigma_\alpha = \sqrt{1 - X_\alpha} \cdot \sigma_0 \ . \tag{2.74}$$

Dimer systems, in which dipoles cancel each other out, may be accounted for by setting the dimer population within the grid up to 50%, with dimer sites assigned randomly and dipoles on the assigned sites set to zero. Note, however, that the remaining energy parameters remain constant.

Once the grid site energies are set up holes are allocated randomly to sites, using the scheme outlined by van der Holst[31], for a given hole density, weighted according to their Fermi-Dirac distribution probabilities,

$$p_i = \left(1 + e^{(E_i^{site} - E_F)/k_B T}\right)^{-1} \ , \tag{2.75}$$

using the preselected temperature, T, and Fermi energy, E_F, inputs. The cumulative sum of the probabilities for a hole occupying each site is found,

$$s_j = \sum_{i}^{j} p_i \ , \tag{2.76}$$

and a number, η, between zero and s_N, where N is the total number of grid sites, is chosen at random. A site, s_j, is chosen if it satisfies the inequality,

$$s_{j-1} < \eta < s_j \ . \tag{2.77}$$

Once the hole is placed on s_j, the probability is set to zero and the cumulative sum of the probabilities is found for the updated grid. This process is repeated until all the holes are assigned their grid sites.

For hopping, unoccupied neighbouring grid sites within a radius of $\left(\sqrt{3} \cdot L\right)$ of the charge particle are considered, where L is the grid lattice constant. Each possible hopping event is accompanied by an energy change in the system, ΔE. For a hop between two sites, $\boldsymbol{i}$ and $\boldsymbol{j}$, at a distance, $\boldsymbol{R_{ij}}$, to one another, the energy change is given by,

$$\Delta E_{\boldsymbol{ij}} = E_{\boldsymbol{i}}^{site} - E_{\boldsymbol{j}}^{site} + \Delta E_{\boldsymbol{ij}}^{coulomb} \tag{2.78}$$

where $E_{ij}^{coulomb}$ is the associated change in Coulomb energy,

$$\Delta E_{\boldsymbol{ij}}^{coulomb} = E_{\boldsymbol{i}}^{coulomb} - E_{\boldsymbol{j}}^{coulomb} \ , \tag{2.79}$$

which is calculated for each site using,

$$E_{\boldsymbol{i}}^{coulomb} = \frac{1}{\epsilon_r} \cdot \sum_{\substack{j \neq i \\ j = occupied}} \frac{1}{|\boldsymbol{R_{ij}}|} \tag{2.80}$$

where ϵ_r is the relative permittivity of the medium.

The change in energy due to hopping, ΔE, is used to calculate the associated hopping rate, k, using the appropriate rate equation. For charge transfer between two sites, $\boldsymbol{i}$ and $\boldsymbol{j}$, the Miller-Abrahams hopping rate[32] is given by,

$$k_{\boldsymbol{ij}} = \omega_0 e^{-2\gamma|\boldsymbol{R_{ij}}|} \times \begin{cases} e^{-\Delta E_{\boldsymbol{ij}}/k_B T} & \Delta E_{\boldsymbol{ij}} > 0 \\ 1 & \Delta E_{\boldsymbol{ij}} \leq 0 \end{cases} \tag{2.81}$$

and the Marcus rate[27] is given by,

$$k_{\boldsymbol{ij}} = \omega_0 e^{-2\gamma|\boldsymbol{R_{ij}}|} \times e^{-\left(\lambda + \Delta E_{ij}\right)^2 / 4\lambda k_B T} \tag{2.82}$$

where ω_0 and λ are the pre-assigned hopping attempt frequency and reorganisation energy, respectively.

Once a hopping event is executed, and the grid updated, the rates for any possible event within a cut-off radius of the new charge site are recalculated. This cut-off radius is several times greater than the lattice constant and is set large enough to capture all relevant sites that have a significant impact on the energies of the new possible hopping sites.

Both the Miller-Abrahams (2.81) and Marcus (2.82) rate equations may only be used within a field limit beyond which results become unreliable. Using the Miller-Abrahams rate (2.81), at high field, the change in energy between sites is dominated by the field term so that downfield hopping events become highly energetically favourable and no upfield hopping occurs. As a result, the flux and drift velocity remain constant while the field is increased further, and the mobility tends to zero. Similarly, using the Marcus rate (2.82), at high field, the site energy is dominated by the field term so that downfield hopping events with a positive change in Coulombic energy have a higher probability of being chosen. Therefore, over time the simulation will develop to increase the overall Coulomb energy of the system, as charges concentrate downfield, until an equilibrium is reached the and the charges move downfield together as a wave.

Here, the hopping rate limit is reached when,

$$\lambda + \Delta E = 0 \,. \tag{2.83}$$

Assuming charges hop in the direction of the field, site energy differences may be given by,

$$E_{\boldsymbol{i}}^{site} - E_{\boldsymbol{j}}^{site} \approx - E_F \cdot L \,. \tag{2.84}$$

And the highest rate occurs when,

$$\Delta E_{\boldsymbol{ij}}^{coulomb} = E_F \cdot L - \lambda \,. \tag{2.85}$$

Therefore, if the reorganisation energy is significantly smaller than the applied field strength, the simulation will tend to draw hopping events that give a positive $\Delta E^{coulomb}$, and the Marcus equation may be used if,

$$E_F \cdot L \leq \lambda \quad . \tag{2.86}$$

Since kMC algorithms are able track rare events that occur over long time-steps they are suitable for simulating hopping transport, and therefore predicting the average mobility of a system. However, it should be noted that due to their probabilistic weighting, kMC results tend to be skewed favourably towards high-rate events, which may result in slower processes being underrepresented.

References

1. CharTED-KMC, https://github.com/thomasjamespope/CharTED-KMC, (accessed January 2024).
2. Frank Jensen, *Introduction to Computational Chemistry*, John Wiley & Sons Ltd, Chichester, 2nd edn., 2007.
3. Andrew R. Leach, *Molecular Modelling Principles and Applications*, Pearson Education Ltd, Essex, 2nd edn., 2001.
4. C. J. Cramer, *Essentials of Computational Chemistry: Theories and Models*, John Wiley & Sons Ltd, Chichester, 2nd edn., 2004.
5. C. D. Sherrill*, An Introduction to Hartree-Fock Molecular Orbital Theory*, School of Chemistry and Biochemistry, Georgia Institute of Technology, 2000.
6. W. Koch and M. C. Holthausen, *A Chemist's Guide to Density Functional Theory*, Wiley-VCH Verlag GmbH, 2nd edn., 2001.
7. T. Pope, Y. Giret, M. Fsadni, P. Docampo, C. Groves and T.J. Penfold, *Organ. Electron.*, 2023, **115**, 106760.
8. M. Born and R. Oppenheimer*, Ann. Phys.*, 1927, **389**, 457.
9. P. Hohenberg and W. Kohn, *Phys. Rev.*, 1964, **136**, B864.
10. W. Kohn and L. J. Sham, *Phys. Rev.*, 1965, **140**, A1133.
11. J. M. Poblet, X. López, and C. Bo, *Chem. Soc. Rev.*, 2003, **32**, 297; S. Wen, W. Guan, J. Wang, Z. Lang, L. Yan, and Z. Su, *Dalton Trans.*, 2012, **41**, 4602.
12. J. P. Perdew,K. Burke and M. Ernzerhof, *Phys. Rev. Lett.*, 1996, **77**, 3865.
13. A. D. Becke, *Phys. Rev. A*, 1988, **38**, 3098; C. Lee, W. Yang, R. G. Parr, *Phys. Rev. B*, 1988, **37**, 785.
14. K. Burke, *J. Chem. Phys.*, 2012, **136**, 150901.
15. C. Adamo and V. Barone, *J. Chem. Phys.*, 1999, **110**, 6158.
16. J. P. Perdew and K. Schmidt, *AIP Conf. Proc.*, 2001, **577**, 1.
17. B. J. Alder and T.E. Wainwright, *J. Chem. Phys.*, 1959, **31**, 459.
18. L. Verlet, *Phys. Rev.*, 1967, **159**, 98.
19. A. P. Thompson, H. M. Aktulga, R. Berger, D. S. Bolintineanu, W. M. Brown, P. S. Crozier, P. J. in 't Veld, A. Kohlmeyer, S. G. Moore, T. D. Nguyen, R. Shan, M. J. Stevens, J. Tranchida, C. Trott and S. J. Plimpton, *Comp. Phys. Comm.*, 2022, **271**, 10817.
20. F. Neese, *Wiley Interdiscip. Rev. Comput. Mol. Sci.*, 2012, **2**, 73; F. Neese, *Wiley Interdiscip. Rev. Comput. Mol. Sci.*, 2017, **8**, e1327.

21. H. C. Andersen, *J. Comput. Phys.*, 1983, **52**, 24; H. C. Andersen, *J. Chem. Phys.*, 1980, **72**, 2384.
22. D.A. Case, H.M. Aktulga, K. Belfon, I.Y. Ben-Shalom, J.T. Berryman, S.R. Brozell, D.S. Cerutti, T.E. Cheatham, III, G.A. Cisneros, V.W.D. Cruzeiro, T.A. Darden, N. Forouzesh, G. Giambaşu, T. Giese, M.K. Gilson, H. Gohlke, A.W. Goetz, J. Harris, S. Izadi, S.A. Izmailov, K. Kasavajhala, M.C. Kaymak, E. King, A. Kovalenko, T. Kurtzman, T.S. Lee, P. Li, C. Lin, J. Liu, T. Luchko, R. Luo, M. Machado, V. Man, M. Manathunga, K.M. Merz, Y. Miao, O. Mikhailovskii, G. Monard, H. Nguyen, K.A. O'Hearn, A. Onufriev, F. Pan, S. Pantano, R. Qi, A. Rahnamoun, D.R. Roe, A. Roitberg, C. Sagui, S. Schott-Verdugo, A. Shajan, J. Shen, C.L. Simmerling, N.R. Skrynnikov, J. Smith, J. Swails, R.C. Walker, J. Wang, J. Wang, H. Wei, X. Wu, Y. Wu, Y. Xiong, Y. Xue, D.M. York, S. Zhao, Q. Zhu and P.A. Kollman, *Amber 2023*, University of California, San Francisco, 2023; D.A. Case, H.M. Aktulga, K. Belfon, D.S. Cerutti, G.A. Cisneros, V.W.D. Cruz eiro, N. Forouzesh, T.J. Giese, A.W. Götz, H. Gohlke, S. Izadi, K. Kasavajhala, M.C. Kaymak, E. King, T. Kurtzman, T.-S. Lee, P. Li, J. Liu, T. Luchko, R. Luo, M. Manathunga, M.R. Machado, H.M. Nguyen, K.A. O'Hearn, A.V. Onufriev, F. Pan, S. Pantano, R. Qi, A. Rahnamoun, A. Risheh, S. Schott-Verdugo, A. Shajan, J. Swails, J. Wang, H. Wei, X. Wu, Y. Wu, S. Zhang, S. Zhao, Q. Zhu, T.E. Cheatham III, D.R. Roe, A. Roitberg, C. Simmerling, D.M. York, M.C. Nagan and K.M. Merz Jr., *J. Chem. Inf. Model.*, 2023, **63**, 6183.
23. B. R. Brooks, C. L. Brooks III, A. D. Mackerell, L. Nilsson, R. J. Petrella, B. Roux, Y. Won, G. Archontis, C. Bartels, S. Boresch A. Caflisch, L. Caves, Q. Cui, A. R. Dinner, M. Feig, S. Fischer, J. Gao, M. Hodoscek, W. Im, K. Kuczera, T. Lazaridis, J. Ma, V. Ovchinnikov, E. Paci, R. W. Pastor, C. B. Post, J. Z. Pu, M. Schaefer, B. Tidor, R. M. Venable, H. L. Woodcock, X. Wu, W. Yang, D. M. York and M. Karplus, *J. Comput. Chem.*, 2009, **30**, 1545.
24. A. E. Allen, M. C. Payne and D. J. Cole, *J. Chem. Theory Comput.*, 2018, **14**, 274; J. M. Seminario, *Int. J. Quantum Chem.*, 1996, **60**, 1271.
25. F. Weigend and R. Ahlrichs, *Phys. Chem. Chem. Phys.*, 2005, **7**, 3297; F. Weigend, *Phys. Chem. Chem. Phys.*, 2006, **8**, 1057.
26. H. Hellmann, *Zeitschrift für Phys.*, 1933, **85**, 180; R. P. Feynman, *Phys. Rev.*, 1939, **56**, 340.
27. R. A. Marcus, *Annu. Rev. Phys. Chem.*, 1964, **15**, 155.
28. G. Marsaglia and W. W. Tsang, *J. Stat. Softw.*, 2000, **5**, 1.
29. J. J. M. Van der Holst, F. W. A. Van Oost, R. Coehoorn and P. A. Bobbert, *Phys. Rev. B*, 2011, **83**, 085206.
30. R.H. Young, *Philos. Mag. B*, 1995, **72**, 435; R.D. Misra, *Math. Proc. Camb. Philos. Soc.*, 1940, **36**, 173.

31. J. J. M. van der Holst, PhD Thesis, Eindhoven University of Technology, 2010.
32. A. Miller and E. Abrahams, *Phys. Rev.*, 1960, **120**, 745.

3 Theoretical Studies of Hole Transport Materials

3.1 Introduction

Charge transport in amorphous organic hole transport materials (HTMs) has a hopping character.[1] The charge hopping between neighbouring sites has been parameterised in disorder- and polaronic-based models[1,2], and the effects of properties, such as molecular packing, on overall mobility have been extensively studied.[3-5] Despite this, predicting mobility and designing high performing HTMs remains a challenge. The amorphous nature of these materials is reflected in the distribution of conformations and orientations of molecules within a film, and the corresponding distribution of their properties. This makes studying the interplay of charge transport parameters, and accurately modelling mobility a complex task.[5] Here we look at the relationship between the experimental mobilities of a range of HTMs, and their theoretically derived molecular and charge transport properties. Later, the results of kinetic Monte Carlo (kMC) studies are discussed in which the interplay of hopping transport parameters are studied. Figures **3.13**-**18** were generated by Dr Thomas Pope. Results from our kMC studies have been published:

> T. Pope, Y. Giret, M. Fsadni, P. Docampo, C. Groves and T. Penfold, *Org. Electron.*, 2023, **115**, 106760.

3.2 Hopping transport

The mobility of charge carriers depends on the type of charge transport regime present in the material. Amorphous organic semiconductor films tend to be dominated by weak van der Waals and π-π stacking interactions, resulting in highly localised energetic sites.[1] In disordered systems such as these, the movement of localised charge carriers is described in terms of 'hops' between discrete sites, separated by an energy barrier. Sites may be part of a molecule, a whole molecule or a distinct group of molecules and hole mobility through these materials is related to the average rate of hole hopping between these sites.[1] Hopping rates have been parameterised through disorder- and polaron-based

models, each representing limiting cases, and, therefore, may be applied to different systems with varying levels of success.[2]

3.2.1 Disorder-based models versus unified disorder and polaron-based models

In amorphous systems, energetic disorder is conventionally considered the dominant parameter governing the rate of charge transport.[3] The widely used Gaussian disorder model (GDM), describes the hopping of charges between sites of different energies, where the density of states (DOS) has a Gaussian distribution.[4] Within this model, the energetic disorder is given by the width of the DOS distribution, σ.

At the disorder limit, in systems with weak electron-phonon (vibrational) couplings and at low temperature, the charge hopping rate, k_{ij},may be given by the Miller-Abrahams equation,

$$k_{ij} = \omega_0 e^{-2\gamma|\boldsymbol{R}_{ij}|} \times \begin{cases} e^{-\frac{\Delta E_{ij}}{k_B T}} & \Delta E_{ij} > 0 \\ 1 & \Delta E_{ij} \leq 0 \end{cases} \tag{3.1}$$

where ω_0 is the hopping attempt frequency, γ is the inverse charge localisation, and $\boldsymbol{R}_{ij}$ is the spatial vector between sites ***i*** and ***j*,** and ΔE_{ij} is the associated energy change for the hopping event.[6] The hopping rate is exponentially dependent on the site distances and the difference in site energies (which depends on the energetic disorder). When the energy of the initial site is greater than the energy of the final site, the charge transfer rate does not keep increasing with the driving force, whilst when the energy of the initial site is smaller than the energy of the final site, the Boltzmann factor gives the activation energy. While the Miller-Abrahams rate is considered appropriate for many systems, it neglects polaronic contributions which may be present in systems with moderate electron-phonon (vibrational) couplings or when temperatures are increased ($\hbar\omega_0 \ll k_B T$).[2,7] Indeed, Fischchuk *et al.* have shown that the activation energy can be decoupled into polaronic and disorder contributions, with the relative weight of each dependent on the system in question, to give a better description of charge transport.[2]

The small polaron model of Holstein and Friedman, describes a polaron as a quasi-particle consisting of the Coulombic interaction of a charge carrier with its surroundings, the so-called electron(hole)-phonon coupling.[8,9] Within this model, a local charge is stabilised by the deformation of the molecular site that it has induced, confining it within a potential well of the order of the lattice constant for the material. Thermal activation is required to alter the configurations of sites to their energetically degenerate transition states allowing a charge carrier to 'hop' out of its initial potential well (disappearance of the polaron) to a newly self-induced well at its final site (creation of the polaron).

According to the Franck-Condon principle, charge transfer occurs faster than the change in the position of the nuclei or the molecular surroundings.[10] Therefore, charge transfer is more likely the more the wavefunctions of the reactant and product overlap, *i.e.*, when their potential energy curves intersect. According to Emin, at the non-adiabatic limit, characteristic of systems where the donor and acceptor molecules are weakly coupled and the reorganisation of the environment facilitates charge transfer, the electronic wave function of the charge carrier changes instantaneously at the transition state.[11]

At the non-adiabatic limit, the semi-classical Landau-Zener charge transfer rate reduces to the Marcus equation, in which the rate for a hop between two sites, ***i*** and ***j***, is given by,

$$k_{ij} = \frac{2\pi}{\hbar}\left|\boldsymbol{J}_{ij}\right|^2 \frac{1}{\sqrt{4\pi\lambda_{ij}k_B T}} \times exp\left(-\frac{\left(\lambda_{ij} + \Delta G_{if}\right)^2}{4\lambda_{ij}k_B T}\right) \tag{3.2}$$

where $\hbar$ is Plank's constant, k_B is Boltzmann's constant, T is the temperature, and $\boldsymbol{J}_{ij}$, λ_{ij} and ΔG_{if}, are the electronic coupling, the reorganisation energy, and the change in Gibbs free energy, respectively.[12,13] In contrast to the Miller-Abrahams equation, the Marcus equation shows additional dependencies the reorganisation energy which has an opposing influence on the driving force and, therefore, the Marcus rate.[14]

The hopping rate may be used to theoretically study the trends in mobility exhibited by HTMs. Intrinsic molecular properties may be obtained from DFT calculations, including single point energies and dipole moments. From these we obtain the reorganisation energy and the energetic driving force for charge transfer due to inter-site energetic disorder relating to the dipole moment, as discussed in sections ***3.4.4*** and ***3.4.7***.[15-18] Interactions between charge transfer dimers can also be investigated using wavefunction methods to obtain electronic couplings, and *ab initio* molecular dynamics (MD) may be used to obtain activation energies and, to some extent, asses the energetic disorder. Film morphologies and insights into charge transfer behaviour may be obtained from classical MD simulations.[1,5,17,18] On a broader level, charge transfer in the bulk can be simulated via by kMC, using the rate equations, taking calculated hopping rate parameters as inputs, to arrive at the overall mobility of a material.[5,19]

3.2.2 HTMs investigated

Theoretical studies were performed on literature molecules to understand how mobility parameters relate to experimentally measured mobilities. Density functional theory (DFT), Hartree-Fock (HF) and molecular dynamics (MD) calculations were limited to HTMs with reported pristine experimental

mobilities that were measured against a spiro-OMeTAD reference. Finding molecules with pristine reported mobilities proved to be a challenge, and spiro-OMeTAD reference mobilities were found to vary substantially between studies. For this reason, the compounds included have a reported spiro-OMeTAD reference mobilities within 4 x10^{-5} and 6 x10^{-5} cm^2 V^{-1} s^{-1}. These molecules included amide-, hydrazone- and azomenthine-based HTMs, group **1**, (EDOT Amide TPA; EDOT-MPH; EDOT-, Fu-, Th-, Diazo-, Ph-Inv-, Ph- and TPA-OMeTPA).[20]

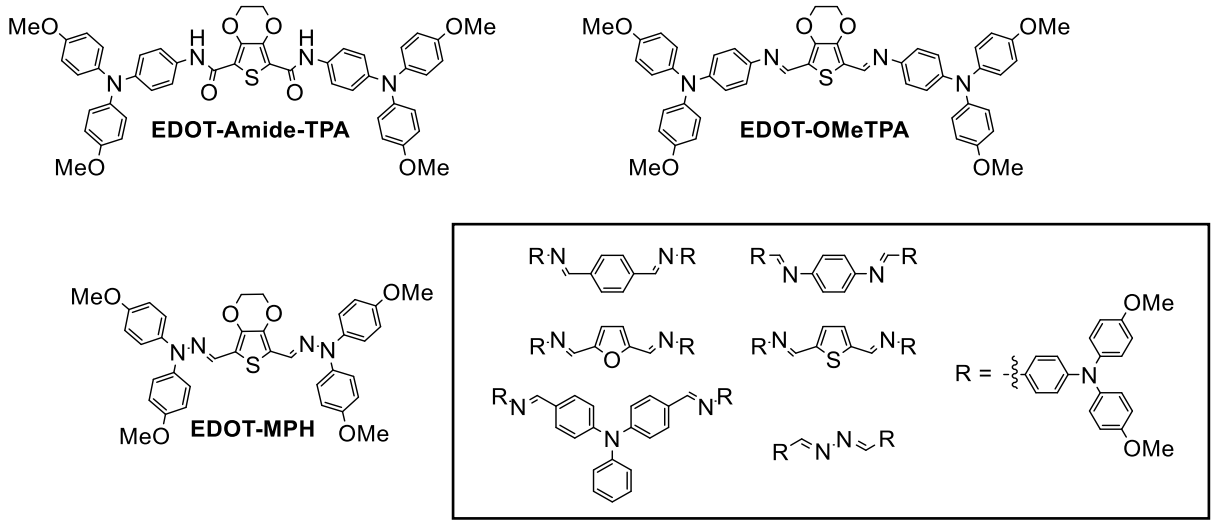

Figure 3.1 Molecular structures of the group **1** compounds; EDOT-Amide-TPA, EDOT-MPH, and EDOT-OMeTPA and other the azomenthine-based HTMs with EDOT, phenyl, furanose, thiophene, triphenylamine (TPA) and diazo-group core, and their triphenylamine (TPA) side unit.[20]

Two further literature molecules with TPA side units (AZO-II, TTz-I) as well as BEDN and X51, were later included to widen the sample of molecules.[21] Frontier orbital energies were also studied, as the appropriate energetic alignment of molecules with the perovskite absorber is essential for these to extract holes and block charge recombination so they can function as HTMs in perovskite solar cells (PSCs). The molecules investigated all had experimental spiro-OMeTAD HOMO reference values between -5.21 eV to -4.80 eV, and included the above mentioned HTMs (omitting X51), as well as 6 literature molecules with DPA side units (Trux-OMeTAD, X22, X26, X36, X59, V886) and further 3 molecules (ST1, TCTA, X55).[22] The molecules chosen, follow the trend in developing stable, low-cost, easy to synthesise and tuneable HTMs. The Docampo molecules, as well as BEDN, TTz-I and AZO-II were all synthesised using facile condensation reactions between cores and side-units. Studying molecules with synthetic advantages may provide an added advantage in informing the design of HTMs.

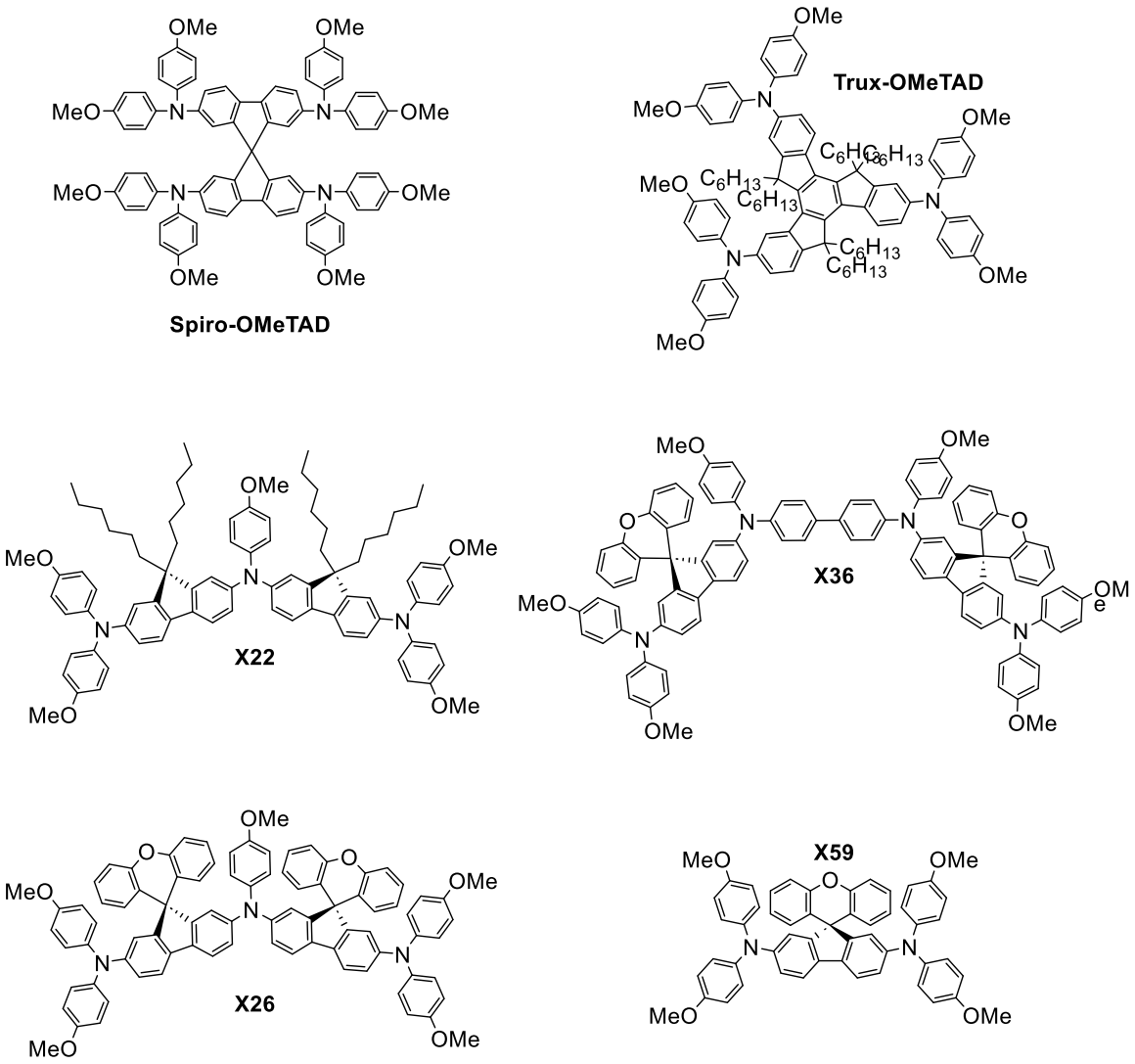

Figure 3.2 Molecular structures of literature HTMs with DPA side units, included with **group 1** molecules to form **group 2**, used in calculating a HOMO energy level correction.[20-22]

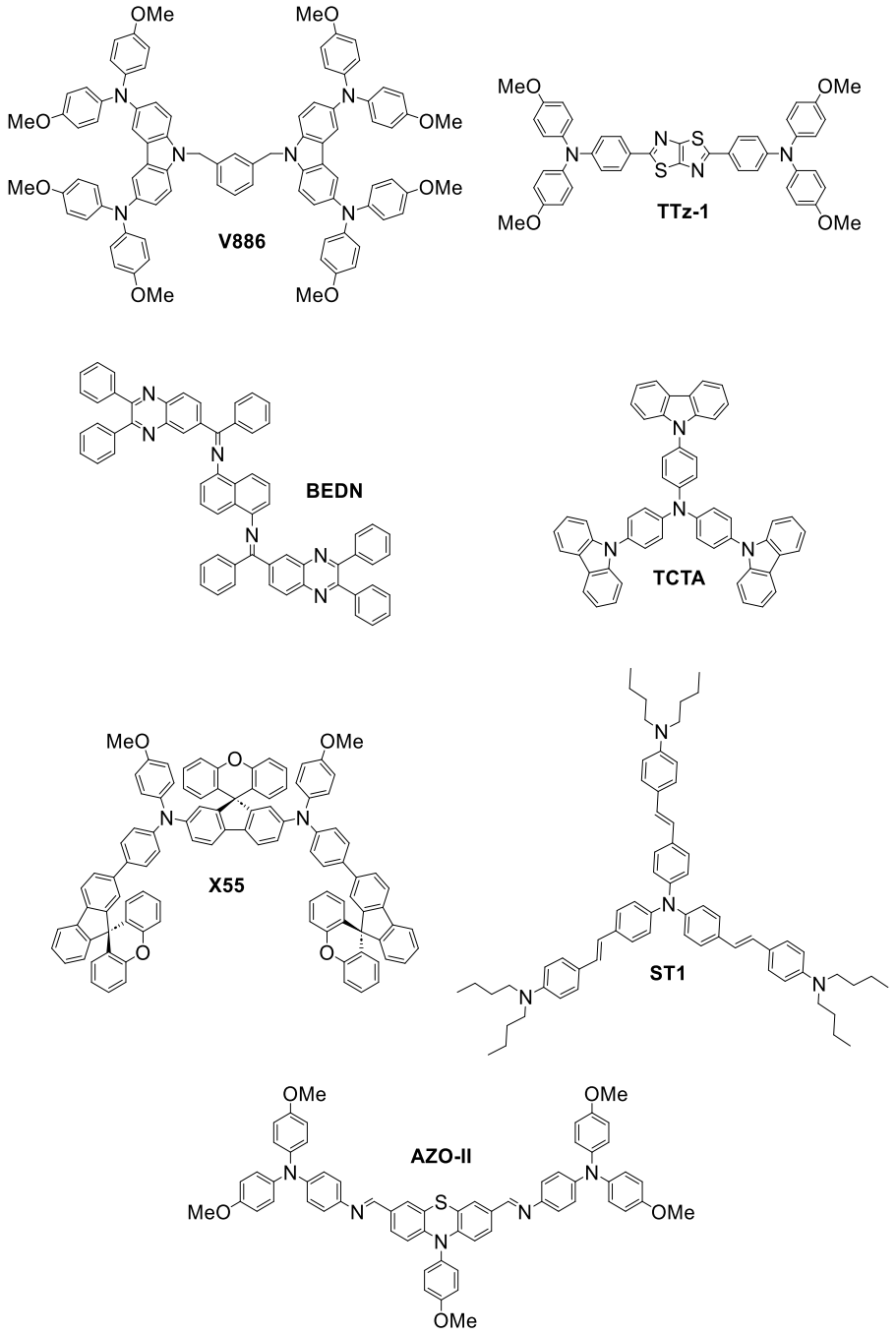

Figure 3.3 Molecular structures of further literature HTMs included with **group 2** molecules, to form **group 3** used in calculating a HOMO energy level correction.[21,22]

Tentative explanations for the good performance of some of these HTMs have been given in the literature. The azomenthine bond in highly conjugated compounds such as EDOT-MPH offers stability, and good conductivity, both desirable features in a HTM.[20] Intermolecular H-bonding in EDOT-Amide-TPA could promote favourable packing arrangements, reduce the disorder of molecules in the film (by restricting changes in conformation) and enhance molecular orbital overlap which might enable better charge transport.[20] This might explain its superior performance to spiro-OMeTAD, despite the break

in conjugation between the core and side-units due to the amide bond. The good performance of AZO-II is partially attributed to its electron-rich phenothiazine core.[21] However, no definitive structure-property relationships have been demonstrated. To understand the mobility trends for these different molecules, we must look into the underlying parameters that determine mobility.

3.3 Computational methods

Single molecule properties of HTMs were obtained from DFT calculations performed using the PBE0 functional[23] and def2-sv(p) basis set[24] using Orca (v. 4 and 5)[25]. The geometries of the neutral and cationic molecules were first optimised in vacuum. The relaxed geometries were then used to calculate the final single point (SP) and frontier orbital energies of the solvated species in dichloromethane, by implementing the conductor-like polarizable continuum model (C-PCM), to approximate the effect of the amorphous environment on the single molecule properties. [19] The electronic state-to-state direct coupling for charge transfer pairs was calculated using QChem (v. 5)[26] at the Hartree-Fock level, with a 6-31G(d) basis set.[27] Molecular dynamics (MD) were run at the semi-empirical level using PM3 calculations with Orca (v. 4) over 10,000 steps, and the temperature of the system was maintained at 300 K using a Berendsen thermostat. Finally, kinetic Monte Carlo (kMC) simulations were carried out using an in-house code, CharTED kMC, implementing both Miller-Abrahams and Marcus-type rate equations.[19]

3.4 Theoretical studies: single molecule properties

3.4.1 Frontier orbital energies

A crucial aspect in the screening of HTMs for devices involves the investigation of frontier orbital energies. HTMs for perovskite solar cells (PSCs) must have LUMO energies higher than the perovskite conduction band (~-3.9 eV), to block electron transfer and prevent charge recombination.[20] Suitable HOMO levels lie around -5.2 eV, slightly above the perovskite valence band level of -5.4 eV, to provide a driving force for hole transport.[20,28] The suitability of molecules for specific device applications is firstly contingent on the alignment of frontier orbital energies, so determining these accurately is an important part of the design process. Comparing theoretical to experimental frontier orbital energies provides a way of gauging the accuracy of theoretical calculations for a class of molecules.

For many organic molecules, DFT hybrid functionals such as B3LYP and PBE0, have been shown to give HOMO–LUMO energy gaps that agree reasonably well with experimental results.[29] However, Zhang and Musgrave found that for some molecules, the DFT frontier orbital energies calculated differ widely from the experimentally determined negative ionisation potentials and electron affinities.[30] The same

authors reported that a simple linear correction could be applied to calculated HOMO energies to significantly reduce the error. Chi *et al.* ran DFT calculations on organic HTMs with spiro cores at the B3LYP/6-31G(d,p) level using dichloromethane as a solvent via the C-PCM.[31] They also found that a fitting value could be applied to the theoretical HOMO values, giving corrected results that were in excellent agreement with experimental HOMO levels from cyclic voltammetry. Petrus *et al.* found that applying this correction also yielded accurate DFT HOMO results for their nine HTMs.[20] Therefore, DFT calculations using hybrid functionals provide a simple theoretical prediction of experimental HOMO-LUMO energies, particularly when a correction factor is applied that has been obtained from a representative group of molecules.

3.4.2 HOMO energy correction

Based on a method reported by Chi *et al.*, theoretical HOMO levels of HTMs in dichloromethane were compared with corresponding experimentally determined energies, as reported in the literature.[30,31] For a group of 15 HTMs (group **2**)[20-22], the theoretical HOMO energies were plotted against their experimental values (**Figure 3.4**) and an excellent linear correlation was found ($R^2 = 0.955$), given by:

$$y = 0.962x - 0.396 \tag{3.3}$$

The molecules in group **2** consist of the symmetrical HTMs shown in **Figures 3.1** and **3.2**; namely the TPA-based compounds EDOT-Amide-TPA, EDOT-MPH, EDOT-OMeTPA, Diazo-OMeTPA, Fu-OMeTPA, Th-OMeTPA, Ph-OMeTPA, Ph-Inv-OMeTPA and TPA-OMeTPA, as well as the DPA-based compounds Trux-OMeTAD, X22, X26, X36 and X59, and spiro-OMeTAD for reference. The absolute mean error between the theoretical and experimental data was found to be 0.206 eV. Owing to the excellent linear correlation, applying a correction factor of -0.206 eV to the theoretical HOMO energies provided values in close agreement with experimental results. Indeed, the absolute mean error between the corrected HOMO values and the experimental HOMO values was found to be 0.019 eV.

Group **2** was expanded to 22 molecules to form group **3**, which a further 7 HTMs, shown in **Figure 3.3**, including molecules with TPA side-units and other HTM types; namely AZO-II, BEDN, ST-1, TCTA, TTz-1, V886 and X55 .[31] The relationship between theoretical and experimental HOMO energies was investigated, using the same approach as described above (**Figure 3.4**). This second larger group showed a weak linear correlation ($R^2 = 0.322$), and an absolute mean error of 0.239 eV.

Applying a correction of -0.239 eV to the theoretical values, resulted in an absolute mean error of 0.105 eV between the corrected and experimental HOMO levels. Interestingly, applying the correction factor of -0.206 eV from the first group to the expanded group of 22 HTM, resulted in a smaller absolute mean error of 0.094 eV between the corrected and experimental HOMO levels. Correcting theoretical HOMO energies by -0.206 eV was, therefore, found to give a modest improvement in the agreement with experimental data. Applying this correction factor to HOMO energies calculated in DCM (C-PCM) at the PBE0/def2-sv(p) level may, therefore, prove to be useful for HTMs with a similar structure to the first group.

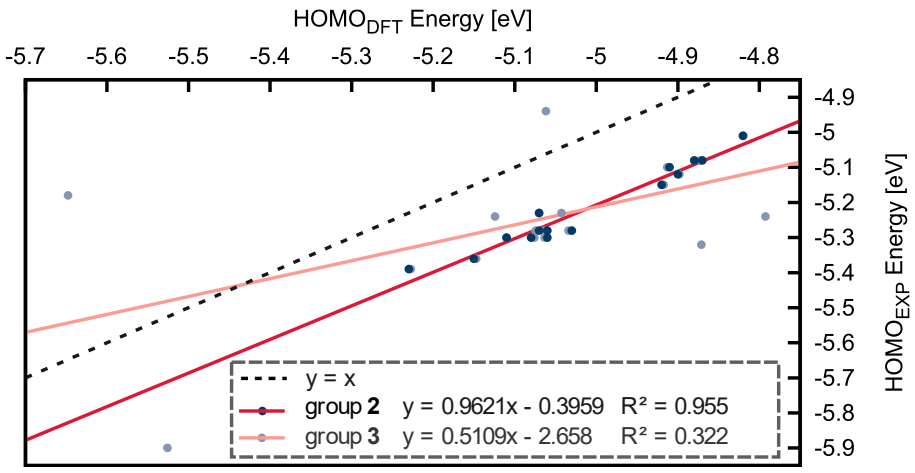

Figure 3.4 Plots of experimental literature HOMO energies against their calculated DFT HOMO energies (PBE0/def2-sv(p)), for group **2** and **3** HTMs, with dashed identity line $y = x$.

3.4.3 Hole hopping rate parameters

The Marcus and Miller-Abrahams rate equations describe charge hopping in terms of the electronic interaction of molecules and the energetics surrounding charge transfer. There is an exponential negative dependency of the hopping rate on the difference in site energies. In a material where all sites are energetically degenerate, or where hole transfer represents an energetically downhill process, the Miller-Abrahams rate simplifies to the coupling and spatial vector terms. However, in an amorphous material, the conformational and orientational distribution of molecules gives rise to energetic disorder, so that there is variance associated with the site energy difference term. It is this energetic disorder that differentiates hopping from the band-like charge transport exhibited by crystalline materials and explains the orders of magnitude lower mobility exhibited by amorphous semi-conductors.

Disorder leads to a distribution of hopping rates and may result in charge percolation via energetically favourable routes, increasing both the distance and time taken for charges to travel through a film, thereby reducing the mobility.[32] Energetic disorder may be separated into two components, the correlated ($E_i^{corr.}$) and uncorrelated disorder ($E_i^{unc.}$).[5] $E_i^{unc.}$ relates to the energetic distribution of HOMO energies due to differences in the conformations of molecules in an amorphous matrix. As with overall rigid molecules, those with HOMOs localised on rigid regions of the structure tend to be less affected by conformational changes and, as a result, the distribution width of $E_i^{unc.}$ may be quite narrow.[33] $E_i^{corr.}$ relates to differences in molecular orientation resulting in inter-site variations in potential due to intermolecular van der Waals and, notably, electrostatic dipole-dipole interactions.[33] In amorphous systems where molecules, and therefore dipoles, are randomly oriented, the energetic noise can be mapped onto a Gaussian distribution, with a width that scales with the size of the dipole moment.[34] The reorganisation energy, which is the energy required by the system to change the conformations of the polaronic initial state to its final state before charge is transferred, may also negatively affect the hopping rate, and is explicitly considered in the Marcus equation. However, its effects may be outweighed and even opposed by other parameters, such as the electronic coupling term.[35]

The hopping rate parameters outlined above, *i.e.*, the electronic coupling, the size of the dipole moment, the width of the distribution of HOMO energies, and the reorganisation energy, were investigated as a simple screening tool for predicting trends in hole mobility which would be useful for HTM design. DFT (PBE0/def2-sv(p)) calculations were performed to obtain the Debye dipole moments of molecules and single point (SP) energies for reorganisation energies (λ_{ij}) of group **1** molecules in vacuum and dichloromethane (C-PCM). The electronic couplings ($\boldsymbol{J}_{ij}$) between charge transfer pairs in vacuum were obtained from Hartree-Fock (6-31G(d)) calculations, using relaxed geometries of the molecules in their neutral and cationic states, generated in vacuum using DFT (PBE0/def2-sv(p)), set with antiferroelectric configurations with respect each other's dipole moments, with centre-to-centre distance of 10 Å (spiro-OMeTAD 16 Å). The correlated disorder was obtained from the width of HOMO energy distributions extracted via DFT (PBE0/def2-sv(p)) for conformations of single molecules in vacuum obtained via MD run at the semi-empirical level (PM3)[36] using Orca (v. 4). Simulations were run over 10,000 steps, with a timestep of 0.5 fs and initial velocities of 300 K. The optimised geometries of HTMs in vacuum were used as MD starting inputs and the molecular geometries, generated in the simulation trajectories, were used to obtain the HOMO energy distributions.

Table 3.1 Mobility, ***μ***, parameters of selected literature molecules in vacuum; ***HOMO*** and ***LUMO*** energies and dipole moments were obtained directly from DFT calculations (PBE0/def2-sv(p)); ***HOMO SD*** gives the standard deviation of DFT (PBE0/def2-sv(p)) HOMO energy distributions for conformations obtained via MD; electronic couplings, ***J***, were found using UHF with a 6-31G(d) basis set; reorganisation energies, ***λ***, were calculated from DFT single point energies (PBE0/def2-sv(p)) using Nelsen's four-point method.[16]

Molecule	*μ ($cm^2 V^{-1} s^{-1}$)*	*HOMO (eV)*	*LUMO (eV)*	*Dipole (D)*	*HOMO SD (eV)*	*J (eV)*	*λ (eV)*
EDOT-Amide-TPA	3.90×10^{-5}	-4.87	-1.82	8.84	0.164	-2.21×10^{-4}	0.110
Diazo-OMeTPA	1.00×10^{-6}	-4.91	-1.56	2.35	0.165	2.91×10^{-3}	0.151
EDOT-OMeTPA	5.00×10^{-6}	-4.80	-1.99	2.09	0.152	-2.21×10^{-4}	0.162
Fu-OMeTPA	5.00×10^{-7}	-4.88	-2.00	3.58	0.119	5.74×10^{-4}	0.172
Ph-Inv-OMeTPA	6.00×10^{-6}	-5.02	-1.56	3.82	0.125	-3.64×10^{-3}	0.167
Ph-OMeTPA	4.00×10^{-6}	-4.93	-2.03	2.46	0.163	-6.04×10^{-4}	0.102
Th-OMeTPA	1.00×10^{-5}	-4.90	-2.14	2.82	0.146	-8.55×10^{-4}	0.143
TPA-OMeTPA	1.00×10^{-6}	-4.88	-1.72	1.88	0.165	8.14×10^{-4}	0.084
EDOT-MPH	2.80×10^{-5}	-4.52	-1.16	3.90	0.179	-1.03×10^{-4}	0.273
Spiro-OMeTAD	4.00×10^{-5}	-4.60	-0.751	2.27	0.141	1.86×10^{-3}	0.070

3.4.4 Reorganisation energy

Reorganisation energy includes the energy changes associated with both the long-range electronic and nuclear adaptations in the environment induced by local charge transfer between a donor and acceptor site, as well as the short-range changes in the active region itself. Calculations for this parameter can therefore be simplified by separating the long-range outer-sphere (λ_{out}) and short-range inner-sphere (λ_{in})contributions.[1]

$$\lambda = \lambda_{in} + \lambda_{out} \tag{3.4}$$

The outer-sphere reorganisation energy generally constitutes a more significant contribution to the total reorganisation energy for solvated species.[15] In organic solids, that are characterised by weak van der Waals intermolecular interactions, outer-sphere contributions are often neglected. This is because the response of long-range properties to local conformational changes in these systems is generally weak.[37,38] Therefore, the reorganisation energy may be simplified to the inner-sphere component, λ_{in}, which is readily found using Nelsen's four-point method,

$$\lambda \approx \lambda_{in} = E_+^* - E_+ + E_0^* - E_0 \tag{3.5}$$

were E_0 and E_+ are the energy of the neutral and cationic molecules, respectively, in their relaxed states, E_+^* is the energy of the cation in the neutral geometry, and E_0^* is the energy of the neutral molecule in the cationic geometry.[16]

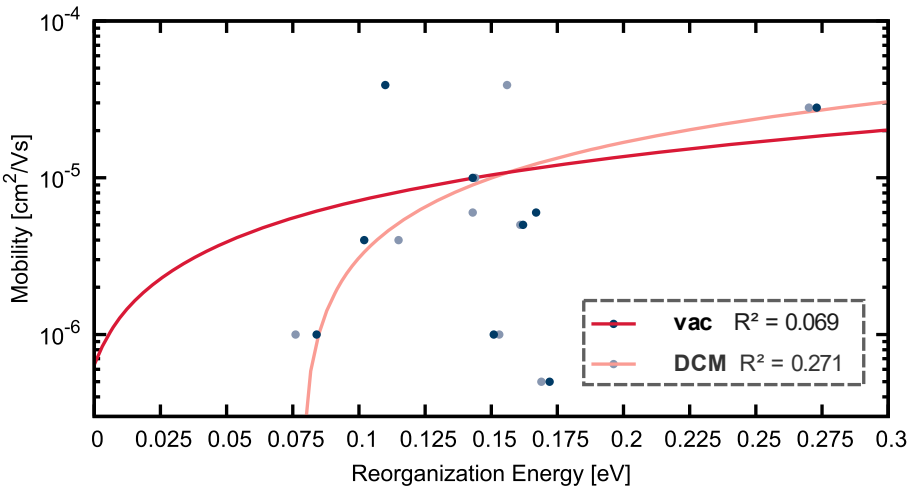

Figure 3.5 Mobility against theoretical reorganisation energies of group **1** molecules in vacuum and DCM.

Reorganisation energies are commonly determined using SP energies from DFT calculations run in vacuum, ignoring entropy since this is likely negligeable at 300 K. This approach fails to account for

the limits to conformational freedom experienced by molecules in the solid phase.[17,18] It also does not capture other effects from the interaction between donor and acceptor molecules.[39] However, using this approach may be sufficient for the purpose of comparing the relative reorganisation energies of similar molecules.

No correlation was found between group **1** theoretical vacuum λ and experimental mobilities. However, a very weak positive correlation was found between theoretical DCM λ and experimental mobilities. This opposes the relationship given in the Marcus rate equation, but may simply be explained by the small data set being skewed by the high reorganisation energies of the two highest performing HTMs. These results suggest that, in this series, other parameters, such as the driving force and electronic coupling, likely dominate over polaronic effects experienced by these molecules. This would agree with a recent study which shows that the molecular reorganisation contributes only weakly to the mobility and justifies the use of a simple Miller-Abrahams rate model over the Marcus rate for describing charge transport in amorphous organic solids.[40]

3.4.5 Uncorrelated disorder: HOMO energy distribution

The DFT (PBE0/def2-sv(p)) HOMO energies were calculated for conformations in vacuum obtained from MD snapshots for each HTM. When plotted, these were found to approach a normal distribution. The standard deviations (SD) of the HOMO energies are listed in Table **3.1**, and in HTM group **1** these ranged between 0.12 and 0.18 eV. The HOMO SD of spiro-OMeTAD was found to be 0.13 eV, which is close to 0.15 eV, reported in the literature.[35] While there is a modest difference in the distribution widths across the group, it is worth noting that the HOMO SD of the highest performing HTM, EDOT-Amide-TPA, and that of molecules with mobilities more than one order of magnitude lower, Ph-, TPA- and Diazo-OMeTPA, are within 0.001 eV of each other. These results suggest that the uncorrelated disorder plays a minor role, and other factors such as the correlated disorder may be dominant. This is rather surprising, since Friedrich *et al.* found that intrinsic disorder provides the dominant contribution to differences in the hole mobility of low dipole amorphous materials, in contrast with high dipole molecules like Alq_3.[41,42] This is because the low energetic barrier to rotations around dihedral angles, result in pronounced changes in conformation and HOMO energies, and may therefore, give rise to significant differences in the width of the uncorrelated disorder between molecules. One explanation for our findings may be the similarity of group **1** molecules which differ mainly in their core units, although the amide linker in EDOT-Amide-TPA gives rise to localisation of the HOMO on the TPA side-units. Therefore, the large conformational changes that are possible may

be nevertheless give rise to similar energy distributions width across this class of compounds. In addition, the TPA units make up a substantial part of the molecule so that the HOMO is mainly concentrated on this moiety.

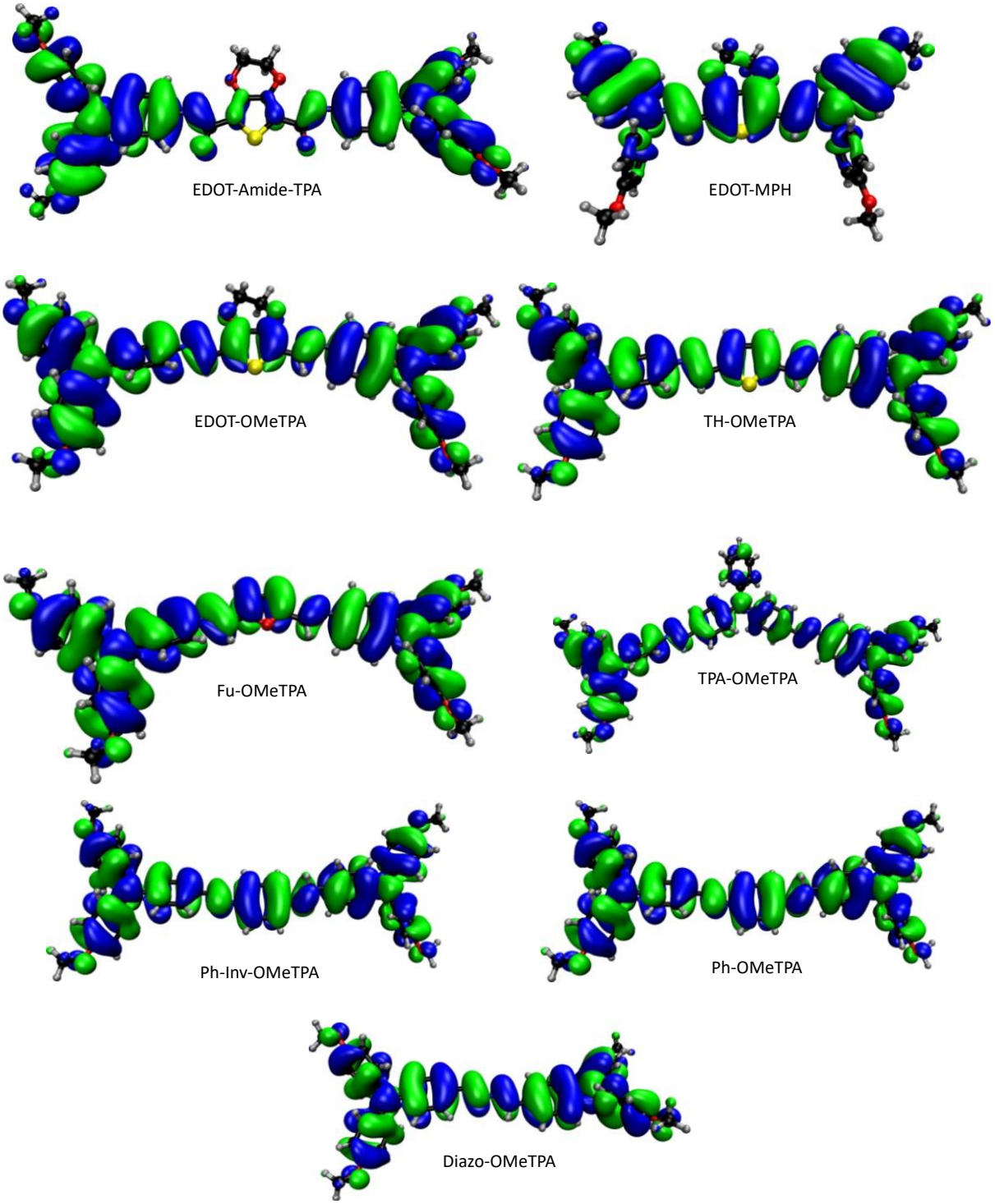

Figure 3.6 HOMO orbitals of group **1** molecules in DCM.

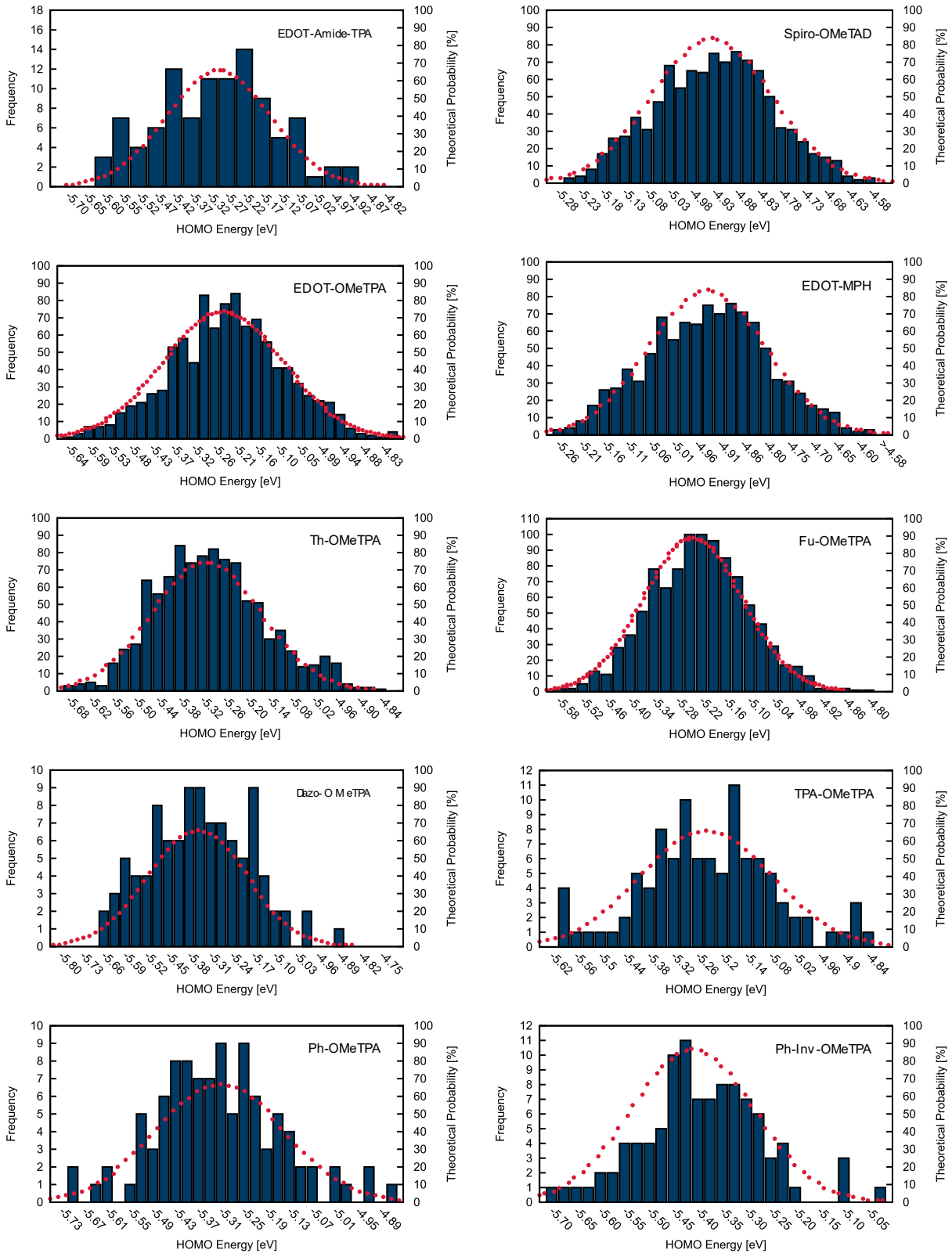

Figure 3.7 Distributions of DFT (PBE0/def2-sv(p)) HOMO energies of group **1** molecules and spiro-OMeTAD structures obtained from MD (PM3) simulation snapshots.

Mensfoort *et al.* suggested that in α-NPD, disorder is entirely spatially correlated (i.e. due to the dipole moment) since rotations around the C−C torsional angle are the most energetically favourable, resulting in the decoupling of the triarylamine units and two energetically degenerate HOMO sites.[41] However, Massé *et al.* later used multiscale modelling and found that in the same molecule disorder is almost entirely uncorrelated, due to conformational restrictions of molecules in the film.[42] These contradictory results point to the impact of the method used and the importance of considering film effects when studying disorder in amorphous materials. Our MD simulations were run at room temperature, as uncorrelated disorder is known to be temperature dependent, and in vacuum which fails to capture any environmental effects, such as restrictions to rotational freedom and stabilised states, which could have a large impact on the level of uncorrelated disorder within the film.[43] The effects of the environment on the uncorrelated disorder was later explored using MD simulations, as discussed in *Chapter 4*.

3.4.6 Electronic coupling

The electronic coupling (or transfer integral) is a key parameter controlling charge transfer rates, and is approximately proportional to the molecular orbital wavefunction, overlap of neighbouring donor and acceptor sites.[44,45] Computationally efficient methods, such as Direct Coupling [DC] methods, have been shown to accurately predict electronic couplings for a wide range of materials.[46] For semiconductors, values fall between 0-0.2 eV, with larger couplings being characteristic of high performing crystalline materials that exhibit band-like transport.[45,47] DC methods treat charge transfer pairs in terms of their charge-localised unrestricted Hartree-Fock (UHF) configurations and represents the initial and final states of the system.[47] The "1+1" DC approach in QChem combines the wavefunctions of charge-localised donor and acceptor fragments.[26] The effective coupling, V_{DA}, mixes these states and is given as half of the energy splitting at the diabatic crossing of these two states[44],

$$|V_{DA}| = \frac{1}{2}(E_1 - E_2) \tag{3.6}$$

In both the Miller-Abrahams and Marcus equations, the rate is shown to increase proportionally with square of the electronic coupling, which decays in strength with distance.[6,15] Disordered materials are characterised by a distribution of electronic couplings,[47] and these are very sensitive to the positioning of molecules, including changes in conformation and packing.[14,47] In close lying molecules (∼3.5 Å) short-range coupling becomes significant.[59] The coupling strength is then heavily influenced by the degree of overlap between the molecular orbitals of adjacent molecules and determines how easily intermolecular charge transfer can occur. The relative positions of molecules (e.g., face-to-face

stacking, edge-to-face, or slipped configurations) influence how their orbitals align and overlap. Unlike long-range Coulombic coupling, short-range coupling is very sensitive to small (sub-Å) transverse displacements which give rise to constructive or destructive interference of orbitals. Destructive interference occurs when atomic orbitals overlap out-of-phase, increasing the energy, while constructive interference occurs when atomic orbitals overlap in-phase, lowering the energy barrier to intermolecular charge transfer. By contrast, long-range Coulombic interactions depend primarily on dipole alignment and are less sensitive to minor molecular displacements. At the weak-coupling limit where the Miller-Abrahams and Marcus rates apply, direct orbital overlap is negligible and charge transfer occurs via tunnelling. [14] The rate of hole hopping decreases exponentially with the distance between the coupling sites.

To generate the dimer pairs, molecules were displaced from their centre-of-mass by 10 Å and 16 Å for Spiro-OMeTAD. This resulted in dimers with core-to-core distances of 10 Å (and 16 Å for Spiro-OMeTAD), but different short pi-pi contact distances, ranging between 4-8.4 Å, due to their different conformations. In the crystal structure of EDOT-Amide-TPA the closest intermolecular core-core distance was found to be is 7.7 Å (vs 10 Å in the generated dimers), with short pi-pi contacts of 6.5 Å pi-pi (vs 5.7 Å in the generated dimers)[60] In Spiro-OMETAD crystals, short 4.0 Å (vs 4 Å in the generated dimers) pi-pi contacts were found, while inter-unit-cell distances ranged between 14.72 and 17.28 Å (vs 16 Å in the generated dimers).[61] Miamate *et al.* found intermolecular distances among a series of amorphous hole-transporters with bulky triphenylamine groups was around 6 Å.[58] Therefore, although there is some variation in the intermolecular distances between the dimers generated, they are in a range that is consistent with molecules of this type. Additionally, Friedrich *et al.* found that between centre-of-mass distances of 5-10 Å, there is little change in the intermolecular coupling strength between dimer pairs of the same molecule. [5,18]

For group **1**, no correlation was found between experimental mobilities and the calculated $\boldsymbol{J_{ij}}$ of charge transfer pairs, oriented antiferroelectrically with respect to their dipole moments. The distribution of electronic coupling strengths in an amorphous film, and the interplay of hopping parameters make it difficult to relate any trends in mobility to a single computed value. Therefore, the absence of a clear trend may reflect the limitation of using single dimer configurations to represent the average inter-site coupling in the entire amorphous film. While the molecules in this group are similar, the actual orientation and packing in their amorphous films may differ widely, especially between the bulkier TPA-OMe-TPA and the planar EDOT-Amide-TPA with H-bonding sites. We can expect the films of these molecules to contain different ranges of dimer configurations, with differing inter-site distances and relative monomer orientations, which would give rise to different ranges of electronic couplings.

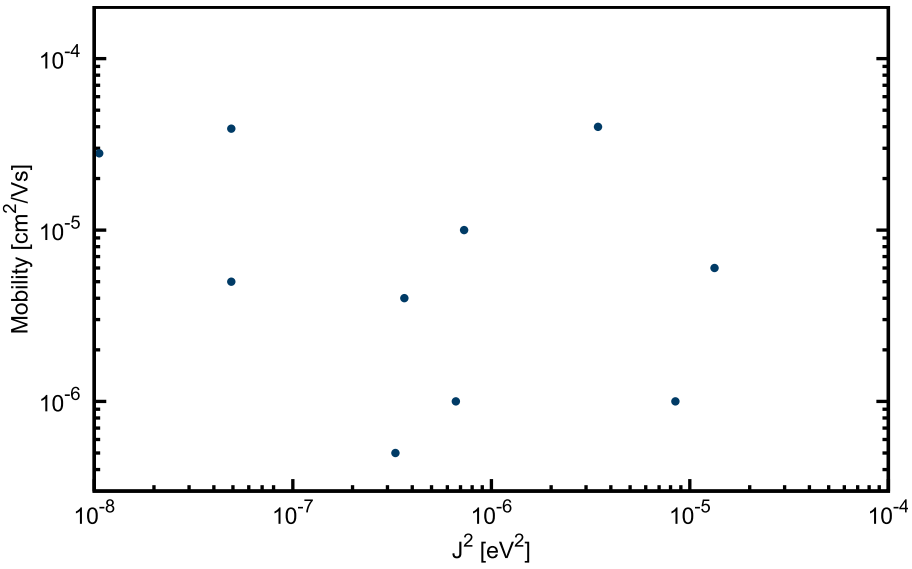

Figure 3.8 Electronic coupling squared, given as the Effective Coupling, squared, of group **1** molecules and spiro-OMeTAD, using UHF with a 6-31G(d) basis set, against their experimental mobilities.

A representative range of coupling values from different dimer configurations may be extracted from crystalline structures. However, this is far more challenging in disordered systems. Using fine-grained film models, an average electronic coupling and its standard deviation can be found. Doing so is more likely to reveal any trends in electronic coupling strengths and experimental mobilities. Even so, the electronic coupling strength can be a misleading screening tool for HTM design. For example, while higher dipoles may lead to closer packing and stronger coupling, this could have the knock-on effect of increasing the correlated disorder, as the effects of both favourable and unfavourable electrostatic interactions are enhanced when coupling sites are brought closer together.[19]

3.4.7 Dipole moment and correlated disorder

Amorphous HTMs lack long-range order, so the orientation of molecular dipoles in these materials is disordered. The permanent dipole moments of neighbouring sites interact, and the energies of polar molecules are, therefore, spatially correlated. The distribution width of this correlation energy gives us a measure of the uncorrelated energetic disorder.[52] Higher dipole moments result in a more complex energetic landscape with a wider distribution, and have been shown to quench mobility.[17,18] However, several molecules exhibit contradictory properties, *i.e.*, high mobilities and high dipole moments.[20,53] Indeed, a modest positive linear correlation ($R^2 = 0.726$) was found between the Debye dipole moments of group **1** molecules and their experimental mobilities, although this can be mainly attributed to two molecules and no correlation was found when the sample size was increased. It is unclear how the high dipole moment of EDOT-Amide-TPA and EDOT-MPH impacts the mobility;

whether it might provide a driving force for favourable self-assembly during film formation, or whether its deleterious effects on mobility are counteracted by other parameters.

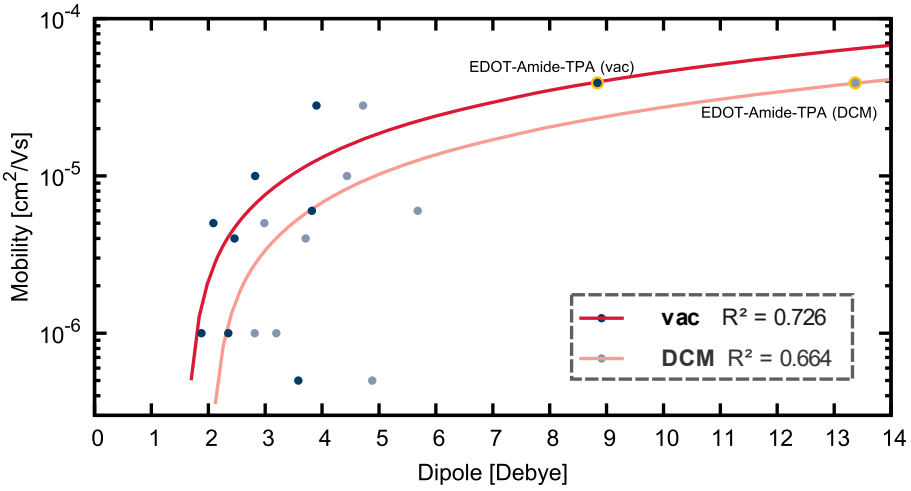

Figure 3.9 Mobility against Debye dipole moment of relaxed neutral group **1** molecules in vacuum (vac) and DCM, with the coefficient of determination, R^2, of their linear trendlines given in the insert.

While amorphous materials are characterised by a lack of long-range order, some exhibit ordered domains which may be due to intermolecular dipole-dipole interactions.[54] These materials include so-called "auto-organised amorphous glasses".[55] High dipole moments on molecules can lead to supramolecular assembly into tightly bound centrosymmetric dimer aggregates with anti-parallel dipole arrangement leading to an overall dipole moment that approaches zero.[53] The preferential orientation of dipole moment vectors within ordered domains leads to higher film density and a more favourable energetic landscape, resulting in a higher charge carrier mobility.[56] Therefore, it is important to differentiate between global and local disorder and consider both in analyses. Failing to consider local order may result in overestimation of the correlated energetic disorder by assuming a wider DOS and significant errors in the calculated mobility.[54] A further complication is that disorder rate models generally assume a Gaussian DOS, based on the absorption band shape of disordered organic materials.[14] In reality, however, the DOS may be more complex. However, the presence of such ordered domains greatly depends on the deposition technique used. Physical vapour deposition (PVD) tends to achieve higher quality films and has been shown to give rise to an anisotropic structure, while spin-coated films tend to show a lower degree of molecular orientation ordering, lower film density and glass transition temperature.[51,56,57] Therefore, while dipole-dipole interactions may play a role during film formation via spin-coating, H-bonding may be more significant in molecules such as such as EDOT-Amide-TPA and could explain the higher-than-expected mobilities seen here.[20]

3.4.8 Limitations of single molecule calculations

While single molecule and dimer calculations can provide a detailed molecular description of the isolated species, they do not properly account for film effects which may significantly impact the hopping parameters in some materials. Fully disordered materials tend to exhibit a distribution of conformations and orientations of molecules within a film, that will also differ in terms of their relative distances to one another. These distributions are generally assumed to be Gaussian in shape, with the width of the distribution representing the degree of disorder within a material. However, the film formation process and intermolecular electrostatic interactions may lead to a more complex DOS through for example the presence of ordered domains. Therefore, the level of disorder may be lower or higher than predicted in the film, where molecules are constrained. It is also important to consider that these parameters interact in a complex way, particularly when materials are neither fully ordered nor fully disordered, so that no clear relationship can be drawn between any one and overall mobility. Once such example would be the electronic coupling, which is highly dependent on both distance and orientation of molecules, and its relationship with the correlated disorder.

As mentioned previously, electrostatic interactions are likely to have a significant impact on packing of molecules. For example, the ability of molecules to H-bond may dramatically impact the level of order within the film and would need to be considered for a correct representation of any of the hopping parameters and prediction of hopping rates. C-PCM was implemented to include solvation effects in dichloromethane, however, this can only approximate the amorphous environment. In addition, the molecules were not optimised with C-PCM implemented, as doing so would greatly increase the computational cost. Instead, geometries of the molecules optimised in vacuum were used when C-PCM was implemented to obtain frontier orbital and single point energies as well as electronic dipole moments. For a more thorough description of the charge transport mechanism, simulations of the film structure and of the hopping process would need to be conducted.

3.5 Theoretical studies: kinetic Monte Carlo simulations

The properties extracted from single molecule and dimer quantum chemical calculations, could not adequately explain the mobility trends in the HTMs under investigation. Furthermore, the modest positive correlation between the dipole moment and mobility, and the surprising trend in reorganisation energies, indicate that energetic disorder and packing may play an important role in these molecules. Therefore, charge transport simulations using kMC could lend insight into the relationship between the molecular and bulk properties. kMC methods map the dynamic evolution of a system from state to state by using the probability distributions of random inputs and is suitable for simulating processes that run over longer timescales. Since charge hopping is a rare event, the transition between one state and another is independent of previous transitions (Markov Chain) and this ergodic behaviour means that random sampling should, in principle, provide a representative output mobility for the system.[59]

3.5.1 Kinetic Monte Carlo method

Kinetic Monte Carlo simulations were performed for a range of systems using the "CharTED-KMC" protocol being developed by the Penfold group which makes use of either Miller-Abrahams or Marcus-type rate equations to calculate for hole hopping rates between sites. Theoretical details are outlined in *Chapter 2*.[19]

Table 3.2 Defaults values for kMC used by the CharTED-KMC code.

Parameter	***Default Values***
Uncorrelated disorder [eV]	0.0
Order parameter	0.0
Dipole moment [Debye]	0.5
Lattice [nm]	1.0
Relative permittivity [a.u.]	3.0
Temperature [K]	300
Electric field [V/nm]:	5.0×10^{-2}
Hole density [/site]	1.0×10^{-5}
Reorganisation energy (Marcus rate) [eV]	0.1374
Hopping attempt frequency (Hz)	2.8×10^{14}
Charge localisation factor (eV)	0.1

The hopping rate through a simulated cell of consisting of a cubic lattice of 300 x 300 x 300 sites, was calculated, assuming a spatially homogenous molecular environment and full periodic boundary conditions. The number of simulation steps was set to 10^6 to ensure that convergence was reached, and the average mobility from 22 calculations was found. Parameters were set to their default values, as given in Table **3.2** and **3.3**, unless otherwise specified.

Table 3.3 Zero-order width of the DOS, σ_0, and the associated dipole magnitude, d.

$\sigma_0\ [k_BT]$	*1*	*2*	*3*	*4*	*5*
σ_0 [eV]	0.026	0.052	0.078	0.103	0.129
d [D]	0.171	0.341	0.512	0.682	0.853

3.5.2 Results of CharTED-KMC mobility simulations

Initially, the relationship between mobility and uncorrelated disorder, as well as with the reorganisation energy was explored for fully disordered systems with a range of dipole moments. The mobilities generated by the simulations were based on Marcus hopping rates, with the other free parameters given in Table **3.2**.

Figure **3.10** shows how the mobility changes with the uncorrelated disorder. We found that when the uncorrelated disorder approaches zero, the dipole moment becomes the limiting factor governing the mobility and was explored more fully later (**Figure 3.13(b)**). As the uncorrelated was increased, there is a reduction in mobility so that systems at 0 Debye and an uncorrelated disorder of 0.02 eV have the same mobility as systems at 1 Debye with an uncorrelated disorder of 0.005 eV. The effect of the dipole moment increasingly diminishes compared to the uncorrelated disorder, and from 0.02 to 0.08 eV we see an exponential drop in mobility, as we would expect from the rate equation. Beyond 0.1 eV of uncorrelated disorder, the mobility is effectively quenched.

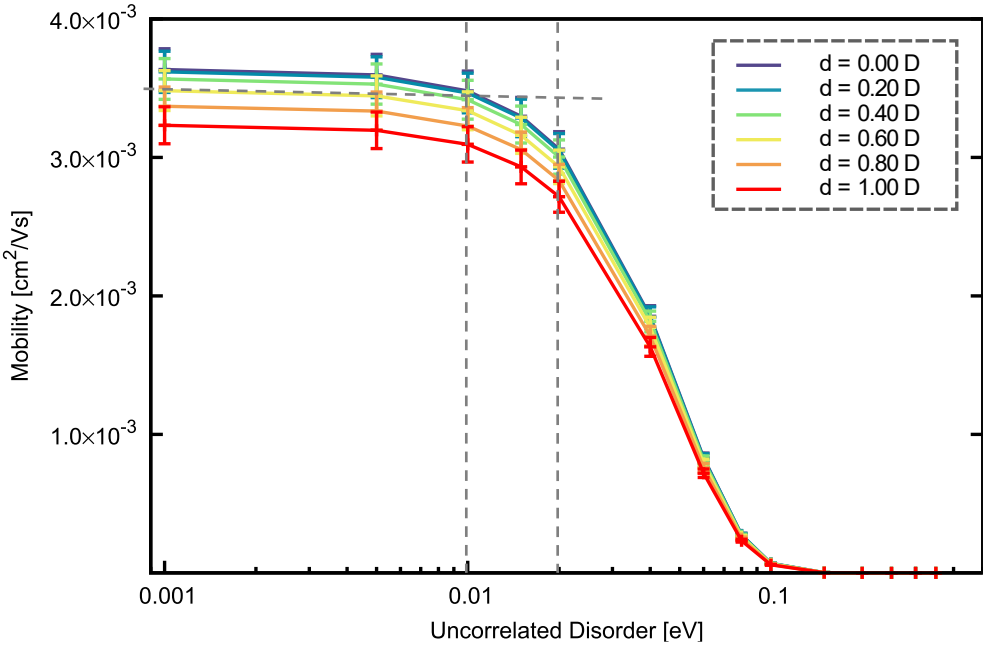

Figure 3.10 Mobility of fully disordered systems ($\alpha = 0$) with a range of dipole moments at E_{Field} = 0.05 V/nm as a function of the uncorrelated disorder, obtained using the Marcus rate equation.

Figure **3.11** shows that the change in mobility with the reorganisation energy is more gradual, as it enters as $exp\left(-\left(\lambda_{ij}\right)^2/4\lambda_{ij}\right)$ in the Marcus rate equation and is valid for values were the reorganisation energy is greater or equal to the product of the applied field strength and the lattice parameter ($\lambda_{ij} \geq E_{field} \cdot L$). As the reorganisation energy increases, the mobility decreases very gradually at first and then almost linearly for systems with $\lambda_{ij} \geq 0.06$ eV, before beginning to plateau again at $\lambda_{ij} \geq 0.2$ eV. The mobility for the 0 Debye systems with $\lambda_{ij} = 0.137$ eV, which is the average reorganisation energy calculated for the group **1** molecules (Section ***3.4***, above), drops to that of the 1 Debye system, when the reorganisation energy is increased by just over 0.01 eV. While we only find a weak correlation between our calculated reorganisation energies and the experimental mobilities of group **1** molecules (Section ***3.4.4***), it is worth noting that the range in reorganisation energies was found to be quite large, up to 0.2 eV and could compound the effect of other parameters on the mobility. However, as discussed previously, the reorganisation energy alone cannot account for the differences observed in the measured mobilities, even for systems with similar dipole moments.

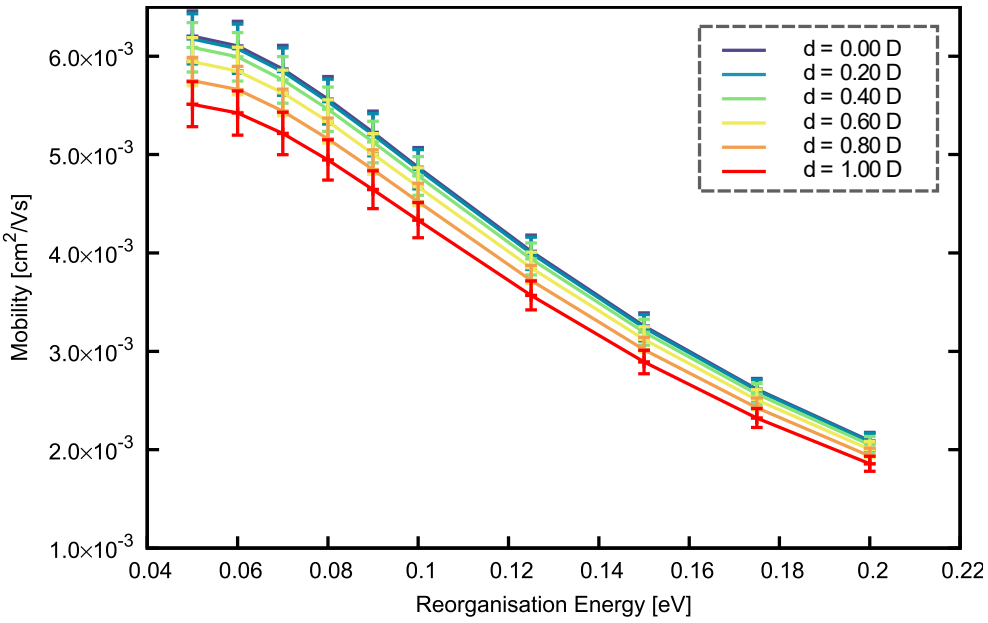

Figure 3.11 Mobility of fully disordered systems ($\alpha = 0$) with a range of dipole moments at E_{Field} = 0.05 V/nm as a function of the reorganisation energy, obtained using the Marcus rate equation.

The change in mobility against the applied electric field was found for a range fully disordered systems, with ($\alpha = 0$), with different dipole moments, using both Marcus and Miller-Abrahams rate equations. Simulations using the Miller-Abrahams rate were carried out for systems with dipole moments in the range 0.171 to 0.853 Debye (Table **3.3**), corresponding to zero-order widths of the DOS, σ_0, equal to $k_BT, 2k_BT, 3k_BT, 4k_BT$ and $5k_BT$. Systems between 0 and 1 Debye were studied with mobilities based on Marcus hopping rates. The remaining simulation parameters (Table **3.2**) were kept the same for both sets of experiments.

Figure **3.13** shows that when the electric field strength, E_{Field}, was below 0.1 V nm^{-1}, the mobility, μ_h,obeys a Poole-Frenkel relationship[52] ($\mu_h = e^{\beta\sqrt{E_{Field}}}$). The trend is similar for Marcus-rate simulations, albeit that the relationship seems to hold at lower field strength, corresponding to 0.03 Vnm^{-1}. The zero-field mobility, μ_{ZF}, could, therefore, be extrapolated from the fitting equation, and was found to decay exponentially with the square of the dipole moment, d, ($\mu_{ZF} \propto e^{\lambda d^2}$), so that a small increase in the dipole moment resulted in a dramatic quenching of the mobility. For the Marcus-rate mobilities, figure **3.12** shows that mobilities increase with the electric field strength from 0.005 Vnm^{-1} up to peak mobilities at field strength between 0.02 for 0.0 Debye systems up to 0.06 Vnm^{-1} for 1.0 Debye systems. Below 0.005 Vnm^{-1}, the external field does not provide sufficient driving force for downfield hopping and at very high field strengths, the mobility is inhibited by coulomb repulsion as charges are concentrated downfield.

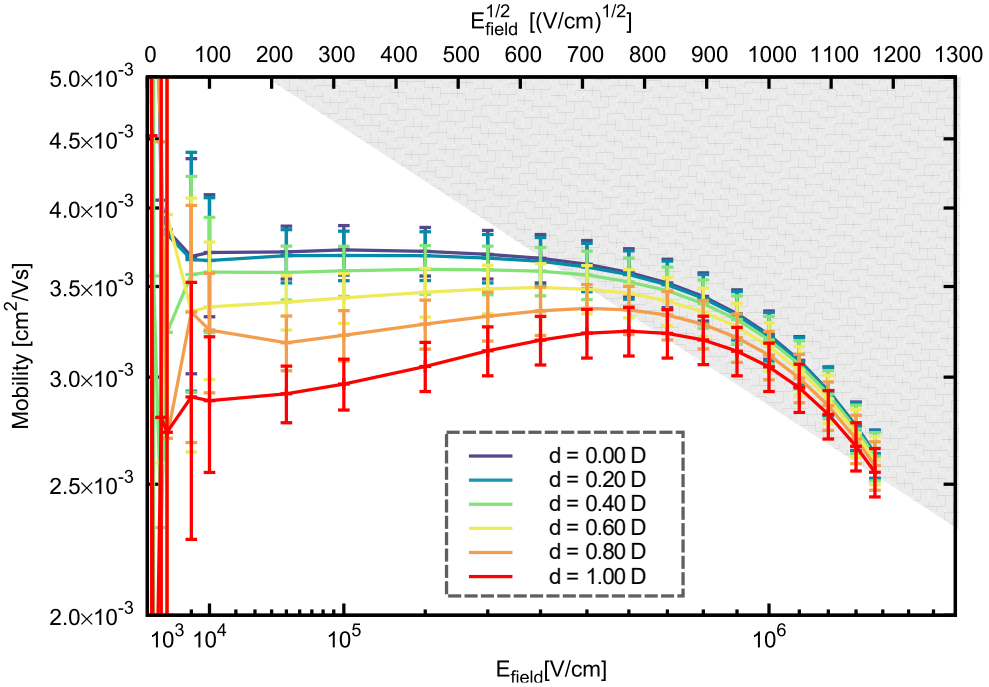

Figure 3.12 Mobility of fully disordered systems ($\alpha = 0$) with a range of Debye dipole moments as a function of the electric field, obtained with the Marcus rate equation with the shaded region indicating the breakdown in the relationship.

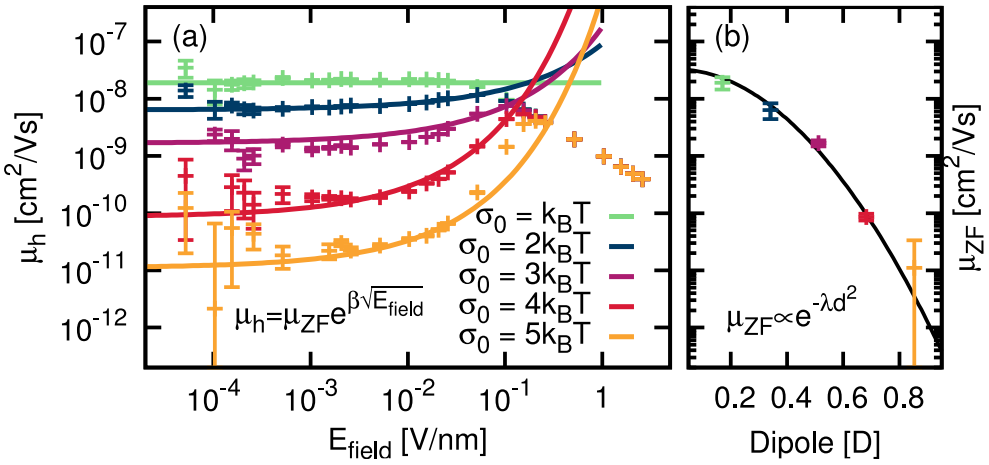

Figure 3.13 **(a)** Mobility of fully disordered systems ($\alpha = 0$) with a range of Debye dipole moments as a function of the electric field, obtained with Miller-Abrahams rate equation. The solid lines represent the fitted Poole–Frenkel-type empirical formula; **(b)** The zero-field mobility as a function of the dipole moment, where the solid black line represents the fitted exponential function with λ = 12.5±0.5.

For a range of dipole moments, *i.e.*, between 0.171 and 0.853 Debye (Miller-Abrahams rate) and 0.0 to 3.0 Debye (Marcus rate), we investigated the effect of dipole ordering on the mobility, by restricting the dipole vector tilt angle on each site.

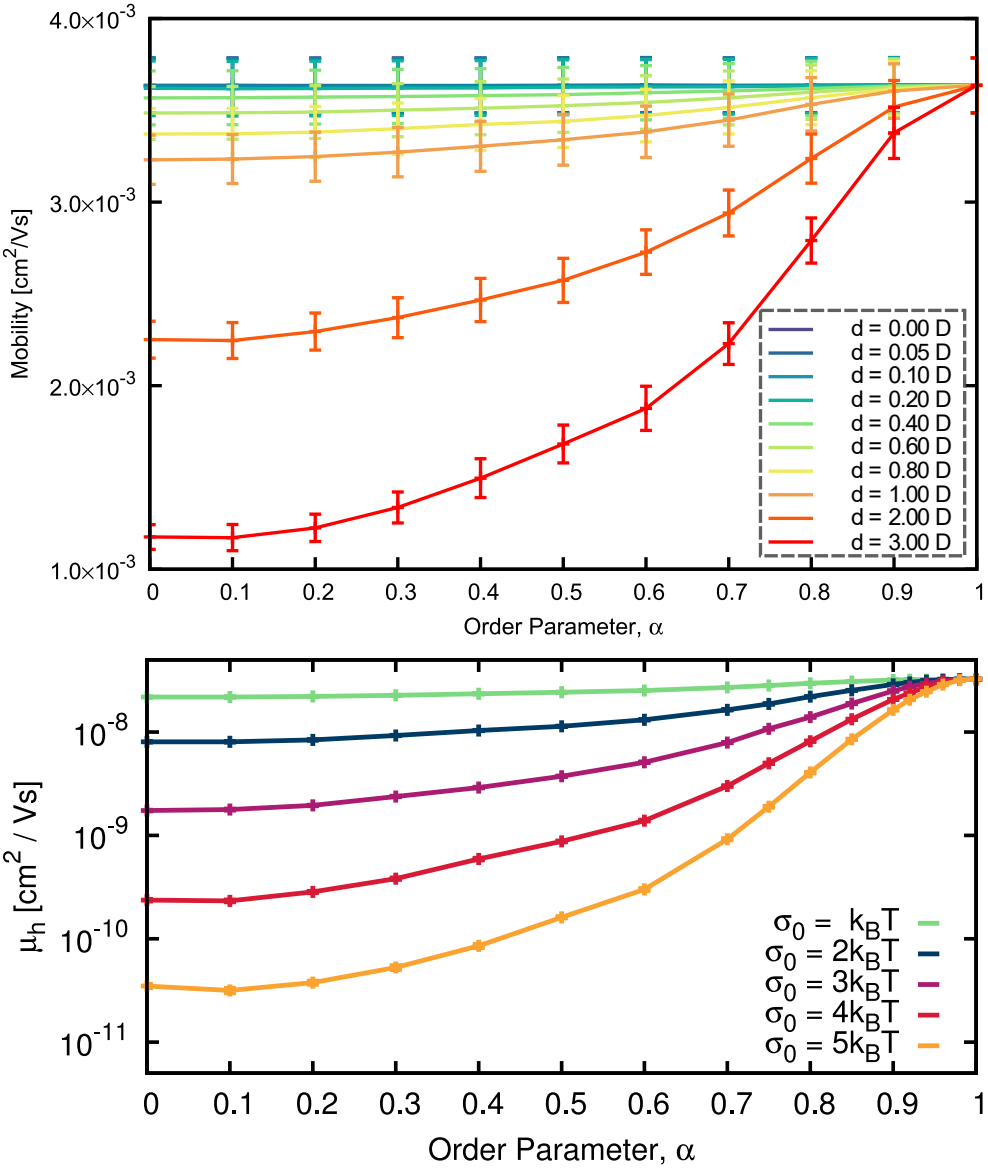

Figure 3.14 Mobility of as a function of the order parameter for systems with a range of dipole moments; obtained using a Marcus rate at E_{Field} = 0.05 V/nm (top), and using a Miller-Abrahams rate at E_{Field} = 0.01 V/nm (bottom).

Figure **3.14** shows that the quenching effect of the dipole moment was greatest when dipoles are oriented randomly, *i.e.*, in fully disordered systems where $\alpha = 0$, when the correlated energetic disorder, E^{corr}, is greatest, and that mobilities increase as the systems become more ordered. This change in mobility is most pronounced in higher dipole systems, so that increased disorder, at 3.0 Debye (**Figure 3.14** (top)) and $\sigma_0 = 5k_BT$ (**Figure 3.14** (bottom)), results in the expected exponential orders-of-magnitude quenching of mobility also observed in figures **3.12** and **3.13**, while only a marginal change is observed in the low dipole moment cases.[34,60] When systems are fully ordered, *i.e.*, $\alpha = 1$, and dipoles are oriented in an antiferroelectric manner to one another, the vectors cancel each other out and the size of the dipole moment has no effect. This is consistent with the cross-term parameter, X_a, tending towards one in the fully ordered case so that the width, σ_α, tends to zero. These results are in contrast with the trends between theoretical dipole moments calculations and experimental mobilities, shown in section ***3.4.7*** above, and show that global ordering of dipoles does not override the deleterious effect that large dipoles have on the mobility. This suggests that the mobilities measured for our best performing group **1** molecules are high despite the large dipole, and that the relationship between the dipole and mobility is more complex than was initially suggested.

The dependence of mobility on the electric field for the different dipole moment systems, for $\sigma_0 = k_BT, 2k_BT, 3k_BT, 4k_BT$ and $5k_BT$, was investigated for the full range of the order parameter, α, and shown in figure **3.15**. These plots show that the mobility tends to be the highest, at $E_{field}^{max} = 2 \times (\sigma_0 - k_BT)/eL$, when the contribution of the dipole interaction term, ΔE_{ij}^{corr}, to ΔE_{ij} in the rate equation (3.1) is matched by the field term ΔE_{field}. Mobility increases with the applied electric field until a saturation point is reached, which is lies within the grey shaded area of figure **3.15 (a-e)**. Beyond this point, there is a very large driving force for downfield hopping so that holes are restricted to a smaller volume of the system. As a result, fewer unoccupied hopping sites are available, and the hopping rate is increasingly reduced. The peak mobility is broader and occurs at lower field strengths in low-dipole systems, as less energy is required for charges to hop between sites. Fully ordered systems have the highest mobilities, and the peak mobility is broader at lower dipoles. As the dipole moment is increased, $\sigma_0 \geq 2k_BT$, the mobility peaks at increasingly higher field strengths for less ordered systems, $\alpha < 0.6$. For high dipole low order systems $\alpha < 0.6$, lower fields do not provide sufficient driving force for downfield hopping to occur preferentially, so that the hopping rate is mainly governed by the correlated disorder and coulomb terms, resulting in a lower mobility.

One way of rationalising the impact of the size of the dipole moment on the hopping rate is via its effect on the width of the DOS, *i.e.*, the energetic noise width of our system. Assuming a Gaussian DOS with a given noise width σ_α, based on the uncorrelated disorder, the energetic noise width may be either enhanced or reduced by incorporating the effect of the correlated energy. However, we go on to see that this explanation may be too simplistic. If the effect of the dipole can be explained entirely in terms of its impact on the width of the DOS, σ_α, then normalising the mobility by $\mu_0 = L^2\omega_0/\sigma_\alpha$ should eliminate the effect of both the magnitude and ordering of the dipole and result in the mobilities being constant for the range of systems with different dipole strengths and order parameters. Here, the normalisation factor, μ_0, is the prefactor to the zero-field approximation of the charge mobility in the Boltzmann regime,

$$\mu(T) = c_1\mu_0 e^{-c_2(\sigma_\alpha/k_BT)^2} \tag{3.7}$$

where, c_1 and c_2 are empirical fitting parameters.

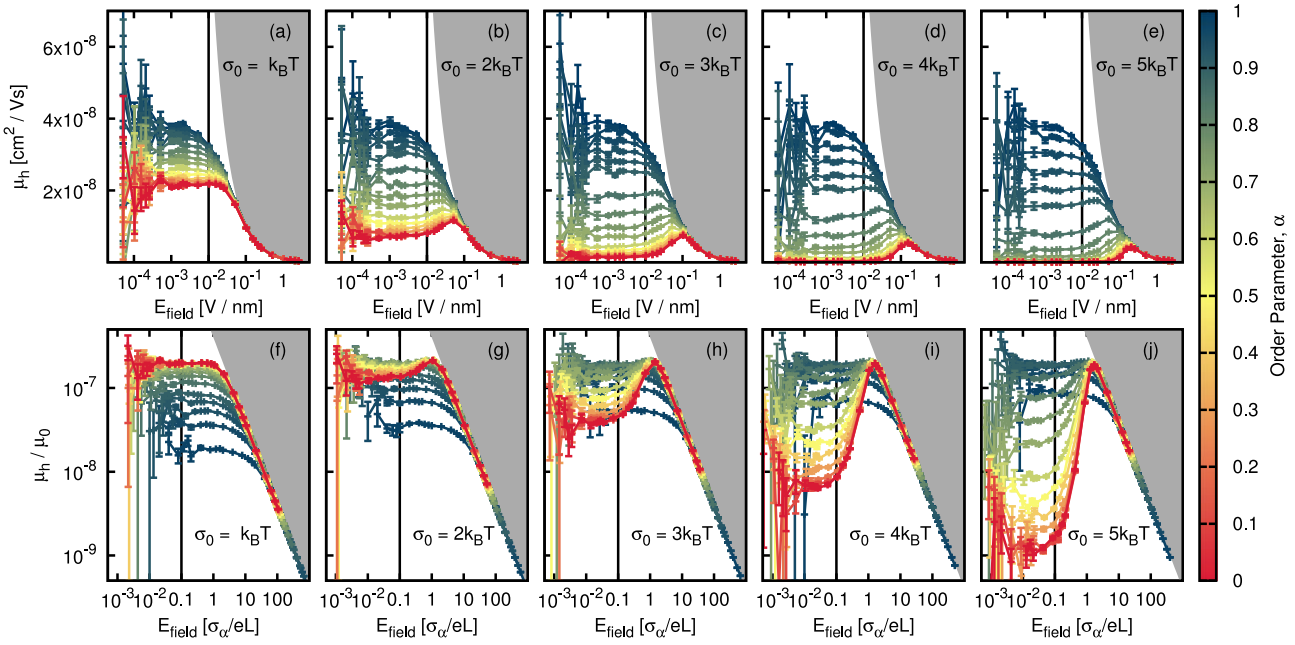

Figure 3.15 Mobility **(a–e),** and normalized mobility **(f–j),** as a function of electric field and the order parameter for the system with a dipole moment corresponding to a zero-order width of the DOS which are $\sigma_0 = k_BT, 2k_BT, 3k_BT, 4k_BT$ and $5k_BT$, respectively. For all cases, the grey-shaded region denotes the saturation point and the vertical line denotes the value for the electric field at which the data for figures **3.14** (bottom) and **3.16** are extracted.

However, figures **3.15 (f-j)** show that this is not the case and, in fact, systems with different dipole strengths are all affected differently by the order parameter, α. When the dipole moment is low, $\sigma_0 = k_B T$, we see that the expected trend in mobility is inverted. Here, normalised mobilities for disordered systems are the highest while fully ordered system have the lowest normalised mobility. Highly ordered systems (blue-green, $\alpha > 0.7$) were found to have normalised mobilities an order of magnitude smaller than more disordered systems (yellow-red, $\alpha > 0.3$). This is because highly ordered systems have a narrow noise width and μ_0 increases as σ_α tends to zero. In higher dipole systems, this effect becomes less pronounced, however when $\sigma_0 = 5k_B T$, the mobility is still lowest when $\alpha = 1$, and indeed for all dipole moments fully ordered systems have the lowest normalised mobility at field strengths above E_{field}^{max}. Above E_{field}^{max}, the normalised mobility is typically highest for order systems in the range $0.7 < \alpha < 0.9$.

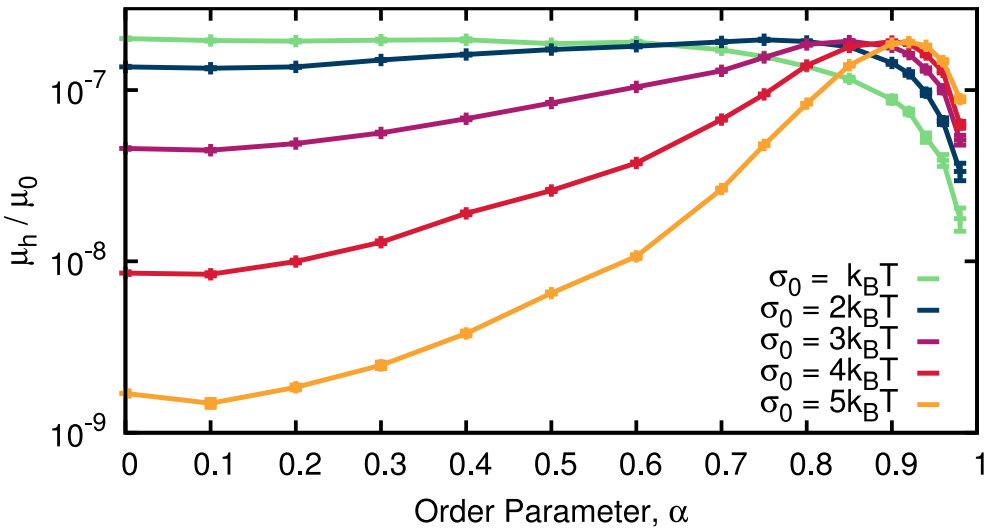

Figure 3.16 Normalized mobility at $E_{field} = 0.1 \times \sigma_\alpha / eL$,

When the normalised mobility is plotted against an arbitrary field strength (**Figure 3.16**), $E_{field} = 0.1 \times \sigma_\alpha / eL$, which is less than E_{field}^{max}, the mobility peaks at $0.7 < \alpha < 0.95$, when $\sigma_0 > k_B T$. As α approaches 1 and σ_α approaches zero, the mobility parameter μ_0 increases and the normalised mobility drops rapidly. When $\sigma_0 = k_B T$ this drop in mobility already begins to occur at order parameters $0.4 < \alpha$. When $\sigma_0 > k_B T$, the normalised mobility increases as the level of order increases up to the mobility peak, with the effect being greatest for high dipole systems which also reach their mobility peak at higher order parameters. Since the global random noise width σ_α is

already included within the normalisation factor, μ_0, the fact that the normalised mobilities still differ with the order parameter and the dipole moment at intermediate levels of order, e.g. in the range $0.1 < \alpha < 0.6$, indicates that ordering of dipoles may result in non-trivial localised effects that enhance the mobility (e.g. percolation).

This led us to map the hopping routes by analysing the cumulative charge population (CCP) on each sites. This is a measure of the number of charges particles that hop onto each site through the duration of the simulation over 10^6 time-steps. Charges are more likely to hop onto sites that are energetically accessible, so these will have a larger CCP. For each dipole moment, figure **3.17(a)** shows the percentage of sites with non-zero flux against the change in order parameter of the system. For fully ordered systems, regardless of dipole moment strength, charges hop onto just over half of all sites over the course of the simulation. As seen previously (**Figure 3.14**), antiferroelectric ordering quenches the dipole moment, so that all sites become energetically accessible. As the level of disorder increases, the CCP becomes distributed over an increasingly small proportion of hopping, an effect which is exacerbated for systems with larger dipole moments. For disordered systems, charge particles have fewer hopping sites energetically available to and, therefore, charge transport is restricted to a smaller proportion of the system. Figure **3.17(b)** shows that for a fully disordered system with a large dipole moment, $\sigma_0 = 4k_BT$, charge transport occurs via highly localised routes, in stark contrast with the fully ordered system in figure **3.17(c)**where the CCP is spread fairly evenly across hopping sites. This explains why the mobility is negatively impacted by higher dipole moment strengths and even further by increasing levels of disorder. In disordered systems, the large energy penalty associated with many of the possible hopping events leaves only few routes available for charges to move through, which may result in inefficient percolation through the system an increase in dead-end traps and longer time delays between events, reducing the mobility. This is exacerbated by the associated increase in the coulomb repulsion experienced by charge particles concentrated into the same small proportion of the system, mirroring the challenge posed by injection barriers in multi-layered devices.[61] The opposite effects in fully ordered systems result in optimal mobility. Charge transport becomes highly efficient as more sites are energetically available, the coulomb term experiences by charge particles is reduced and the time between hopping events is reduced. These combined factors help to explain why the normalisation parameter μ_0 does not effectively cancel out the effects of the strength and ordering of dipoles on the mobility. While this term incorporates the global effect of correlated disorder, we have seen from investigating the CCP that at higher dipole strengths and increased disorder, local effects play an increasingly important role in determining the overall mobility.

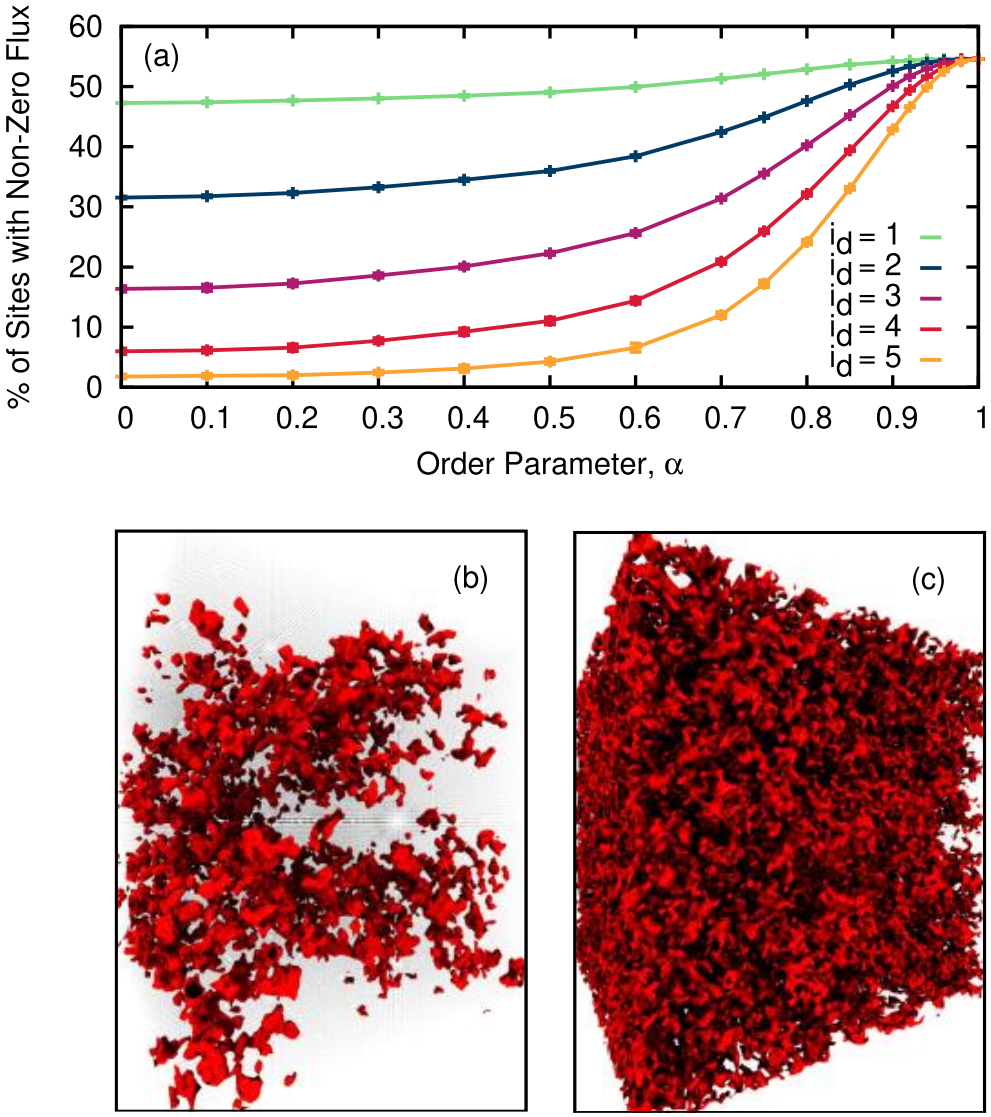

Figure 3.17 **(a)** Proportion of system sites that have been populated by a charge at least once during the simulation against the order parameter for a range of dipole moments; Cumulative charge population density over the system for a dipole moment corresponding to a zero-order width of the DOS of $\sigma_0 = 4k_BT$, with an order parameter of **(b)** 0.0, and **(c)** 1.0.

3.6 Conclusions

In this chapter, we explored the key parameters that underlie hopping charge transport to try and identify experimental mobility trends in a group of amide-, hydrazone-, and azomenthine-linker TPA-based amorphous small molecule organic HTMs. Our results show that it is difficult to predict mobility from singe molecule properties alone, and using these as a screening tool for novel compounds may be misleading, particularly if environmental effects are neglected. Results from our QM calculations do indicate that there is a surprising positive correlation between the dipole moment and mobility in our materials. The high dipole material EDOT-Amide-TPA (8.84 Debye) exhibits the highest experimental mobility, on par with spiro-OMeTAD, possibly due to favourable packing behaviour driven by dipole-dipole and H-bonding interactions.[20] A key question, therefore, is whether the mobility in these materials is high because of the dipole moment, or despite it? Could the high dipole reduce disorder through favourable packing arrangements, or does another unrelated parameter counter its deleterious effects?

To explore this further, we employed a KMC algorithm to study the effect of dipole ordering on the hole mobility of representative systems. Consistent with the literature, we found that high dipole moments create an energetically unfavourable environment for charge transport through the system for cases where the dipole moments are oriented randomly, as they are expected to be in an amorphous thin film. This leads to the charged particles being restricted to localized regions within the system, with a concomitant reduction in mobility. As the dipoles become more ordered, with respect to one another, the correlated disorder is reduced, more sites are energetically accessible leading to an increase in mobility. In addition to this, we find that as dipole moments increase, local interactions between the dipole moments become increasingly significant resulting in charge percolation through the system. Therefore, while high dipole moments significantly reduce mobility in disordered systems, the effects of dipole ordering may offset this to some extent. However, the level of global molecular ordering required is not typically achieved with solution-processed films. It should also be noted that close packing in these high dipole disordered systems would significantly increase the correlated disorder. It is possible that other intramolecular interactions, such as H-bonding[62], may offset or work together with the dipole moment to reduce the energetic disorder in these systems and enabling efficient charge transport. The effect of H-bonding on the dipole moment is, therefore, explored further in *Chapter 4*.

References

1. H. Oberhofer, K. Reuter and J. Blumberger, *Chem. Rev.*, 2017, **117**, 10319.
2. I. I. Fishchuk, A. Kadashchuk, S. T. Hoffmann, S. Athanasopoulos, J. Genoe, H. Bässler and A. Köhler, *Phys. Rev. B*, 2013, **88**, 125202.
3. H. Bässler, A. Köhler, in *Unimolecular and Supramolecular Electronics I.: Topics in Current Chemistry*, ed. R. Metzger, Springer, Berlin, 2011, vol. 312, Charge Transport in Organic Semiconductors, pp. 1-65.
4. H. Bässler, *Phys. Status Solidi B*, 1993, **175**, 15.
5. P. Friederich, A. Fediai, S. Kaiser, M. Konrad, N. Jung and W. Wenzel, *Adv. Mater.*, 2019, **31**, 1808256.
6. A. Miller and E. Abrahams, *Phys. Rev.*, 1960, **120**, 745.
7. L. Berencei, A. Grout-Smith, J. E. Poole and W. Barford, *J. Chem. Phys.*, 2019, **151**, 064120.
8. T. Holstein, *Ann. Phys.*, 1959, **8**, 325.
9. L. Friedman, *Phys. Rev.*, 1964, **135**, A233.
10. J. Franck, *J. Chem. Soc. Faraday Trans.*, 1926, **21**, 536; E. Condon, *Phys. Rev.*, 1926, **28**, 1182.
11. D. Emin, *Phys. Rev. Lett.*, 1974, **32**, 303.
12. R. A. Marcus, *Annu. Rev. Phys. Chem.*, 1964, **15**, 155.
13. V. Stehr, J. Pfister, R. F. Fink, B. Engels and C. Deibel, *Phys. Rev. B*, 2011, **83**, 155208.
14. V. Coropceanu, J. Cornil, D. A. da Silva Filho, Y. Olivier, R. Silbey and J.-L. Bredas, *Chem. Rev.*, 2007**, 107**, 926.
15. R. A. Marcus, *Annu. Rev. Phys. Chem.*, 1964, **15**, 155.
16. S. F. Nelsen, S. C. Blackstock and Y. Kim, *J. Am. Chem. Soc.*, 1987, **109**, 677.
17. I. D. Krysko, A. Y. Freidzon and A. A. Bagaturyants, *Phys. Chem. Chem. Phys.*, 2020, **22**, 3539.
18. P. Friederich, V. Meded, A. Poschlad, T. Neumann, V. Rodin, V. Stehr, F. Symalla, D. Danilov, G. Lüdemann, R. F. Fink, I. Kondov, F. von Wrochem and W. Wenzel, *Adv. Funct. Mater.*, 2016, **26**, 5757.
19. T. Pope, Y. Giret, M. Fsadni, P. Docampo, C. Groves and T. Penfold, *Organ. Electron.*, 2023, **115**, 106760.
20. Spiro-OMeTAD: J. Salbeck, N. Yu, J. Bauer, F. Weissörtel, H. Bestgen, *Synth. Met.*, 1997, **91**, 209-215; EDOT-Amide-TPA: M. L. Petrus, K. Schutt, M. T. Sirtl, E. M. Hutter, A. C. Closs,J. M. Ball, J. C. Bijleveld, A. Petrozza, T. Bein, T. J. Dingemans,T. J. Savenije, H. Snaith and P. Docampo, *Adv. Energy Mater.*, 2018, **8**, 1801605; EDOT-MPH: M. L. Petrus, M. T. Sirtl, A. C. Closs, T. Bein and P. Docampo, *Mol. Syst. Des. Eng.,* 2018, **3**, 734; EDOT-OMeTPA: M. L. Petrus, T. Bein, T. J. Dingemans, and P. Docampo, *J. Mater. Chem. A*, 2015, **3**, 12159; M. L. Petrus, A.

Music, A. C. Closs, J. C. Bijleveld, M. T. Sirtl, Y. Hu, T. J. Dingemans, T. Bein and P. Docampo, *J. Mater. Chem. A*, 2017, **5**, 25200.

21. Azo-II: *ACS Appl. Energy Mater.*, 2019, **2**, 3021; TTz-I: *ACS Appl. Energy Mater.*, 2019, **2**, 7609; BEDN: *J. Mater. Chem. A*, 2019, **7**, 21867; X51: B. Xu, E. Sheibani, P. Liu, J. Zhang, H. Tian, N. Vlachopoulos, G. Boschloo, L. Kloo, A. Hagfeldt and L. Sun, *Adv. Mater.*, 2014, **26**, 6629.
22. Trux-OMeTAD: *J. Am. Chem. Soc.*, 2016, **138**, 2528; X22, X26, X36: *Adv. Energy Mater.*, 2018, **8**, 1701209; X59: *NanoEnergy*, 2016, **23**, 138; V886: *J. Mater. Chem. C*, 2018, **6**, 8874; ST1: *J. Mater. Chem. A*, 2016, **4**, 16330; X55: *Chem 2*, 676–687; TCTA: *Org. Electron.*, 2010, **11**, 427.
23. J. P. Perdew,K. Burke and M. Ernzerhof, *Phys. Rev. Lett.*, 1996, **77**, 3865; C. Adamo and V. Barone, *J. Chem. Phys.*, 1999, **110**, 6158.
24. F. Weigend and R. Ahlrichs*, Phys. Chem. Chem. Phys.*, 2005, **7**, 3297.
25. F. Neese, *Wiley Interdiscip. Rev. Comput. Mol. Sci.*, 2012, **2**, 73; F. Neese, *Wiley Interdiscip. Rev. Comput. Mol. Sci.*, 2018, **8**, e1327.
26. Y. Shao et al., *Mol. Phys*., 2015, **113**, 184; Q-Chem 5.2 User's Manual, https://manual.q-chem.com/5.2/ (accessed 2024).
27. G. A. Petersson, A. Bennett, T. G. Tensfeldt, M. A. Al-Laham, W. A. Shirley and J. Mantzaris, *J. Chem. Phys., 1988,* **89**, 2193; G. A. Petersson and M. A. Al-Laham, *J. Chem. Phys.*, **94**, 6081.
28. D. Ompong and J. Singh, *Org. Electron.*, 2018, **63**, 104.
29. S. Tortorella, M. Mastropasqua Talamo, A. Cardone, M. Pastore and F. De Angelis, *J. Phys.: Condens. Matter*, 2016, **28**, 074005.
30. G. Zhang and C. B. Musgrave, *J. Phys. Chem. A*, 2007, **111**, 1554.
31. W.-J. Chi, Q.-S. Li and Z.-S. Li, *Nanoscale*, 2016, **8**, 6146.
32. R. Coehoorn and P. A. Bobbert, *Phys. Status Solidi A*, 2012, **209**, 2354.
33. M. Malagoli, M. Manoharan, B. Kippelen and J.-L. Bredas*, Chem. Phys. Lett.*, 2002, **354**, 283.
34. H. Bässler, *Phys. Status Solidi B*, 1981, **107**, 9.
35. C. Lee, R. Waterland and K. Sohlberg, *J. Chem. Theory Comput.*, 2011, **7**, 2556–2567.
36. J. J. P. Stewart, *J. Comput. Chem.*, 1989, **10**, 209.
37. J.-L. Bredas, D. Beljonne, V. Coropceanu and J. Cornil, *Chem. Rev.*, 2004, **104**, 4971.
38. V. Stehr, J. Pfister, R. F. Fink, B. Engels and C. Deibel, *Phys. Rev. B*, 2011, **83**, 155208.
39. K. M. Rosso and M. Dupuis, *Chem. Phys.*, 2004, **120**, 7050.
40. R. Saxena, V. R. Nikitenko, I. I. Fishchuk, Ya. V. Burdakov, Yu. V. Metel, J. Genoe, H. Bässler, A. Köhler and A. Kadashchuk, *Phys. Rev. B*, 2021, **103**, 165202.
41. S. L. M. van Mensfoort, V. Shabro, R. J. de Vries, R. A. J. Janssen and R. Coehoorn, *J. Appl. Phys.*, 2010, **107**, 113710.

42. A. Massé, P.Friederich, F. Symalla, F. Liu, R. Nitsche, R. Coehoorn, W. Wenzel and P. A. Bobbert, *Phys. Rev. B*, 2016, **93**, 195209.
43. J. Cottaar, R. Coehoorn, and P. A. Bobbert, *Phys. Rev. B*, 2012, **85**, 245205.
44. A. A. Voityuk, *Phys. Chem. Chem. Phys.*, 2012, **14**, 13789.
45. A. Triosi, *Chem. Soc. Rev.*, 2011, **40**, 2347.
46. J. Y. Lee, S. Roth and Y. W. Park, *Appl. Phys. Lett.*, 2006, **88**, 252106.
47. C.-P. Hsu, *Acc. Chem. Res.*, 2009, **42**, 509.
48. N. J. Hestand and F. C. Spano, *Acc. Chem. Res.*, 2017, **50**, 341−350.
49. F. Wolf, M. T. Sirtl, S. Klenk, M. H. H. Wurzenberger, M. Armer, P. Dörflinger, P. Ganswindt, R. Guntermann, V. Dyakonov and T. Bein, *CrystEngComm*, 2023, **25**, 3142.
50. Y. Li, H. Li, C. Zhong, G. Sini and J.-L. Brédas, *npj Flexible Electronics*, 2017, **2**, doi:10.1038/s41528-017-0002-0.
51. V. Mimaite, J.V. Grazulevicius, R. Laurinaviciute, D. Volyniuk, V. Jankauskas and G. Sini, *J. Mater. Chem. C*, 2015, **3**, 11660–11674.
52. M. Bouhassoune, S.L.M. van Mensfoort, P.A. Bobbert, R. Coehoorn, *Org. Electron.*, 2009, **10**, 437.
53. F. Wuerthner and K. Meerholz, *Chem. Eur. J.*, 2010, **16**, 9366.
54. M. A. Baldo, Z. G. Soos and S. R. Forest, *Chem Phys Lett*, 2001, **347**, 297.
55. E. Ishow, C. Bellaiche, L. Bouteiller, K. Nakatani and J. A. Delaire, *J. Am. Chem. Soc.*, 2003, **125**, 15744.
56. K. Bagchi and M. D. Ediger, *J. Phys. Chem. Lett.*, 2020, **11**, 6935−6945.
57. Y. Sakai, M. Shibata and D. Yokoyama, *Appl. Phys. Express*, 2015, **8**, 096601.
58. M. Shibata, Y. Sakai and D. Yokoyama, *J. Mater. Chem. C*, 2015, **3**, 11178.
59. A. F. Voter, in *Radiation Effects in Solids*, ed. K. E. Sickafus, E. A. Kotomin and B. P. Uberuaga, Springer, Dordrecht, 2007, vol. 235, Introduction to the Kinetic Monte Carlo Method, pp. 1–23; F. Jensen, *Introduction to Computational Chemistry 2nd Edition*, John Wiley & Sons Ltd, Chichester, 2007; A. R. Leach*, Molecular Modelling Principles and Applications 2nd Edition*, Pearson Education Ltd, Essex, 2001.
60. R.H. Young, J.A. Sinicropi and J.J. Fitzgerald, *J. Phys. Chem.*, 1995, **99**, 9497.
61. F. Liu, H. van Eersel, B. Xu, J.G. Wilbers, M.P. de Jong, W.G. van der Wiel, P.A. Bobbert, R. Coehoorn, *Phys. Rev. B*, 2017, **96**, 205203.

4 Investigations of HTM Dimers

4.1 Introduction

In *Chapter 3* we demonstrated that, overall, the dipole moment quenches the mobility of disordered systems.[1] The Miller Abrahams and Marcus rate equations show the dependence of the hopping rate on the negative exponent of the energetic noise width, which may be broken down into uncorrelated and correlated disorder components.[2-5] In the systems we studied (*Chapter 3*), the uncorrelated energetic disorder did not predict the differences in mobility, as HOMO energies and their distributions were found to be similar across the group of molecules. In contrast, the effect of the correlated energetic disorder was found to be significant, although the relationship between dipole moments and experimental mobilities does not appear to be straightforward. kMC simulations showed that global ordering of dipoles only provides modest improvements in mobility and does not adequately explain the favourable experimental charge transport properties exhibited by high dipole amorphous HTMs like EDOT-Amide-TPA.[1] In high dipole materials local effects seem to play an important role in governing hole mobility. Therefore, the effect of the environment and other intermolecular interactions like H-bonding must be considered. Figures **6a-c** were generated by Dr Thomas Pope. Part of this work has been published:

B. Vella, M. Fsadni, T. Pope, M. Giza, F. J. Angus, I. Shmarov, P. L. Lalaguna, M. Cariello, C. Wilson, M. Kadodwala, T. J. Penfold, P. Docampo and G. Cooke, *J. Mater. Chem. A*, 2024 (*accepted*).

E. A. A. Alkhudhayr, D. Sirbu, M. Fsadni, B. Vella, B. T. Muhammad, P. Waddell, M. R. Probert, T. J. Penfold, T. Hallam, E. A. Gibson and P. Docampo, *ACS Appl. Energy Mater.*, 2023, **6**, 22, 11573.

4.2 Intermolecular interactions and molecular ordering in thin films

The energetic noise width is assumed to have a Gaussian distribution which scales with the dipole magnitude.[5] However, as discussed previously, electrostatic interactions influence the packing in the HTL matrix and, therefore, the energetic noise width would be overestimated in systems in which the conformational freedom of molecules is severely restricted.[6] In addition, the relative orientation of molecular hopping sites to one another may result in enhanced or suppressed dipole moment strengths. This becomes particularly important in systems which show some level of ordering at the local level, as this could provide efficient routes for charge transport through areas with lower energetic disorder and/or a reduced number of hopping sites. It is conceivable that closely bound dimers, trimers and larger aggregates, in which monomers are oriented antiferroelectrically to one another with respect to their dipole moments, may operate as singular hopping sites with an overall quenched dipole moment.

While the systems we studied are described as amorphous, in practice, fully amorphous and crystalline films represent limiting cases, which depend to varying degrees on the nature of the material, the method of processing and exposure conditions that could induce phase transitions over time.[6] Processing has been shown to control crystallinity in both polymers and single molecule HTLs. For example, while CDT-BTZ copolymer solution processed films are typically disordered, the use of solvent vapor enhanced drop casting (SVEDC) results in molecular self-assembly via π-π stacking yielding single copolymer fibres of controlled dimensions[7] Large-area homogenous thin films, required for solar cell applications, are produced efficiently by solution processing, which typically results in an amorphous HTL.[6] These films must remain stable over the device lifetime, as they undergo continuous heating and cooling cycles. Even the state-of-the-art solution processed spiro-OMeTAD DSSCs have been shown to exhibit morphologically uncontrolled crystal growth at standard operating temperatures, and more rapidly when leftover solvents and additives are present, resulting in non-homogenous films with adverse effects on device performance and stability.[8] The resulting poor charge transport behaviour may be understood in terms of changes to the potential energy landscape, due to the increased distribution of trap states within the HTL.

Efforts have been made to tune structures to suppress crystallisation and improve long-term stability of devices, such as in the spiro-based HTM Bifluo-OMeTAD.[9]. On the other hand, the use of crystal nano- and microcrystalline materials has been explored in OFETs with very high reported mobilities. Progress has also been made in designing HTMs for solar cell applications which exploit a variety of intermolecular interactions to control molecular ordering in the film.[10] Song et al. developed a series of copolymers that self-assemble to form morphologically stable fibril networks.[11] The spiro-type

dopant free HTM SFDT-TDM, developed by Wang et al., makes use of intermolecular C-H···π interactions, and was found to have higher hole mobility and long-term device photostability and store stability than doped Spiro-OMeTAD devices.[12] Cheng et al. developed dopant free HTMs with varying abilities to undergo self-assembly via π-π stacking. The resulting fibril networks have been described as a "hole transport highway", which reduce the energetic disorder and increase the mobility up to 3.43×10^{-3} V/cm^2 s, on par with doped Spiro-OMeTAD.[13]

Van der Waals and π-π stacking interactions provide an energetic driving force for the ordered packing of molecules. However, with H-bonding and electrostatic dipole-dipole interactions between high dipole molecules stronger directionality and binding strengths are achieved which can be predictably exploited to control molecular ordering in solid films.[14] Wuerthner showed that, much like H-bonding, high dipole moments (> 10 D) drive self-assembly of merocyanine dyes into antiparallel dimer aggregates with exceptionally high binding strengths.[14] The presence of such aggregates has been shown to increase the hole mobility of these materials, as the correlated dipolar disorder of the dimers is quenched.[14,15] The formation of dimers occurs even in dilute solutions and can lead to the formation of conformationally controlled supramolecules, made up of extended H-aggregate π-stacks, from bimolecular complexes up to polymers.[14,15] On the other hand, when weaker and less directional dispersion forces dominate, molecules tend to self-assemble into large oligomeric polydisperse aggregates.[14]

4.3 Effect of the environment on the energetic noise width

The effect of the environment on the correlated energetic noise width of HTMs was investigated via MD simulations with four HTMs: Fu-, Th-, Ph- and Ph-Inv-OMeTPA. A box of 200 molecules was generated with the PackMol package[16], and simulations were run using the LAMMPS package[17] with in the isothermal-isobaric (NPT) ensemble at 300 K and 1 atm of pressure until the systems equilibrated. Snapshot geometries from MD simulations were obtained, and DFT (PBE0/def2-tzvp)[18,19] calculations were performed with Orca[20], using a pairwise dispersion correction[21], and the HOMO energies and dipole moments were extracted. The values were found to fit a Gaussian distribution (Figure **2**) and standard deviations were calculated.

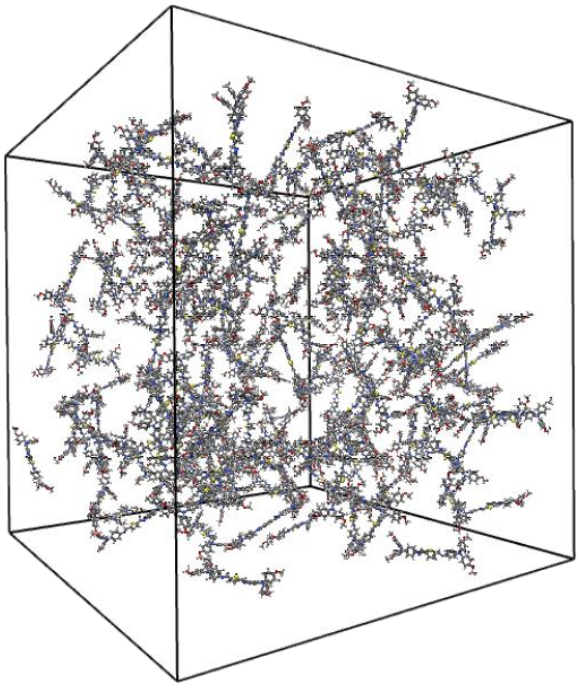

Figure 4.1 Snapshot of Th-OMeTPA MD cubic simulation box of 200 molecules, with a side length of 150 Å.

Fu-OMeTPA and Th-OMeTPA differ structurally by one atom in the core, and by 0.76 D in their calculated dipole moments. However, experimental mobility of Th-OMeTPA was reported to be two orders of magnitude higher than Fu-OMeTPA. Ph-OMeTPA has a calculated dipole that is 1.36 D lower than Ph-Inv-TPA, the structure of which differs only in terms of the linker group, and yet the two HTMs have comparable mobilities. Here again, the calculated dipole moments of the optimised molecules in vacuum do not neatly correlate with the mobility.

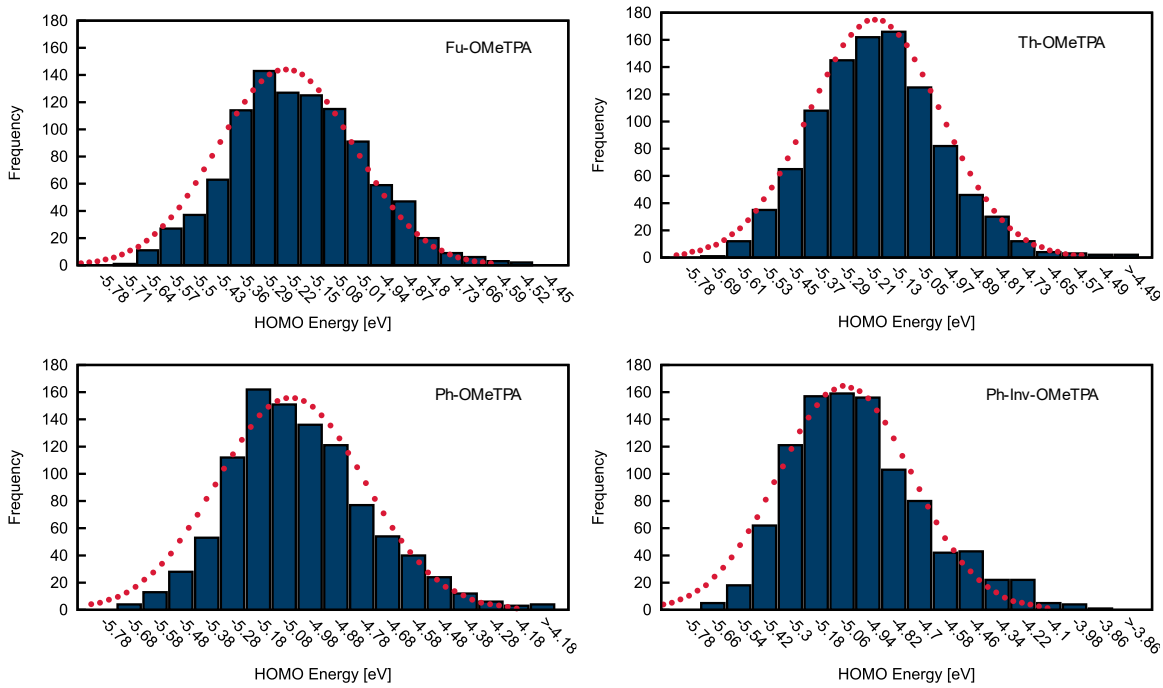

Figure 4.2 Distributions of Orca generated DFT (PBE0/def2-tzvp) HOMO energies of amide HTMs found using bespoke MD.

Table 4.1 Comparison of properties obtained from single molecule DFT calculations, and DFT averages for calculations with point charges using geometries obtained from MD bulk simulation snapshots; these include the single molecule DFT Dipole moments (*Dipole*^{DFT}) and HOMO energies (*HOMO*^{DFT}), average MD DFT dipole moments $\bar{x}_{Dipole}^{MD/DFT}$ and HOMO energies ($\bar{x}_{HOMO}^{MD/DFT}$), as well as their respective standard deviations, $\sigma_{Dipole}^{MD/DFT}$ and $\sigma_{HOMO}^{MD/DFT}$.

Molecule	***μ (cm²/Vs)***	***Dipole^{DFT} (D)***	***$\bar{x}_{Dipole}^{MD/DFT}$ (D)***	***$\sigma_{Dipole}^{MD/DFT}$ (D)***	***HOMO^{DFT} (eV)***	***$\bar{x}_{HOMO}^{MD/DFT}$ (eV)***	***$\sigma_{HOMO}^{MD/DFT}$ (eV)***
Fu-OMeTPA	5.00×10^{-7}	3.58	4.074	1.834	-4.88	-5.223	0.199
Th-OMeTPA	1.00×10^{-5}	2.82	4.079	1.781	-4.90	-5.218	0.196
Ph-OMeTPA	4.00×10^{-6}	2.46	3.769	1.681	-4.93	-5.068	0.271
Ph-Inv-OMeTPA	6.00×10^{-6}	3.82	4.380	1.914	-5.02	-5.038	0.312

Table ***4.1*** shows that while the optimised single molecule dipole moments *Dipole*^{DFT} are between 0.5 and 1.3 Debye higher than the average dipole moments calculated from the constrained MD snapshot geometries $\bar{x}_{Dipole}^{MD/DFT}$, this is less than their distribution widths and the trends in dipole strength

roughly align. The $HOMO^{DFT}$ and $\bar{x}_{HOMO}^{MD/DFT}$ values are in even closer agreement. The standard deviations of both the dipole moment and HOMO energies was found to be remarkably similar for Th-OMeTPA and Fu-OMeTPA, while Ph-OMeTPA was found to have a slightly narrower distribution for both parameters than Ph-Inv-OMeTPA. This suggests that the environment does not significantly alter the global energetic noise width. However, our kMC results (*Chapter 3* section ***3.5.3***) suggest that an overall measure of the dipole and HOMO energy distribution might be unhelpful if local effects dominate.[1] Using the same snapshots obtained from the MD simulations, we also calculated reorganisation energies for Fu-OMeTPA via DFT (PBE0/def2-tzvp) with Orca, again using a pairwise dispersion correction, with geometries optimised in the presence of point charges to approximate the effect of neighbouring molecules on the conformational freedom. However, the high level of variation between our results rendered them inconclusive.

4.4 Theoretical model dimers

As explained in the previous sections, the global ordering of dipoles does not adequately reduce the level of energetic disorder, nor does the effect of the environment on the distribution widths of HOMO energies or dipole moment strengths predict differences in the mobility of our materials. While our HTMs do not display any long-range order, the formation of strongly bound highly ordered molecular aggregates could result in a dramatic drop in the level of energetic disorder, especially at the local level, and may provide routes for efficient hole transport which may be responsible for the high mobilities measured. Dipole-dipole and H-bonding interactions are likely to provide a driving force for the formation and stabilisation of aggregates, including reduced dipole dimers.[14,15] Therefore, we took a more fine-grained approach, investigating the dipole moments and binding energies of theoretical dimers. Using DFT calculations at the PBE0/ def2-sv(p)[18,22] level with Orca, we found the optimised geometries of theoretical dimers of four HTMs, Th-, Fu-, EDOT-OMeTPA and EDOT-Amide-TPA. Theoretically optimised monomers were initially set 8 Å apart and oriented with an inverted configuration to one another, with respect to their dipole vectors, and the dimer geometries were optimised. As expected, we found that these dimers have a quenched dipole moment and binding energies that far exceed the processing or operating temperatures of devices (***Table 4.2***).

Th-, Fu- and EDOT-OMeTPA have comparable binding energies, at 0.431, 0.358 and 0.471 eV, respectively. However, the binding energy of EDOT-Amide-TPA is very high, at 0.956 eV, likely due to H-bonding via the secondary amide linker groups.[23] The drop in dipole from 8.84 to 0.024 Debye represents a very large shift and would significantly reduce the energetic disorder, provided that the

concentration of dimers or dimer units was large enough so that these do not act as charge traps. Interestingly, the binding energy of Fu-OMeTPA is higher and the $Dipole_{Dimer}^{DFT}$ is lower than in Th-OMeTPA, and yet the latter has a higher mobility which is not consistent with what we would expect. In EDOT-Amide-TPA the high dipole moment strength and H-bonding ability likely create a strong driving force for formation of the inverted dimer, as reflected in the high binding energy. However, in Fu- and Th-OMeTPA multiple pairs with different effects, not captured in this experiment, may be present in the film giving rise to the differences in mobility.

Table 4.2 Comparison of Dipole Magnitude between optimised monomer and theoretical optimised inverted dimer, and dimer binding energy from DFT (PBE0/def2-sv(p)) calculations.

Dimer	μ (cm^2/Vs)	$Dipole_{Monomer}^{DFT}$ (D)	$Dipole_{Dimer}^{DFT}$ (D)	Binding Energy (eV)
Fu-OMeTPA	5.00E-07	3.58	0.078	0.431
Th-OMeTPA	1.00E-05	2.82	0.135	0.358
EDOT-OMeTPA	5.00E-06	2.09	0.013	0.471
EDOT-AmideTPA	3.90E-05	8.84	0.024	0.956

4.5 Molecular packing in HTM crystal structures

Crystal structures were obtained for the high dipole amide HTMs, EDOT-Amide-TPA and DEDOT-Amide-TPA. In their pristine states, their conductivities are fairly low. Nevertheless, the conductivity of EDOT-Amide-TPA (3.52x10^{-9} S/cm) was found to exceed that of DEDOT-Amide-TPA (2.58 x10^{-9} S/cm).[24] On oxidation to 50%, with the Co(III) TFSI dopant FK209, their conductivities increased significantly and the conductivity of EDOT-Amide-TPA (7x10^{-6} S/cm) was over an order of magnitude greater than that of DEDOT-Amide-TPA (4x10^{-7} S/cm).[24] EDOT-Amide-TPA is a secondary amide with the ability to form both intra- and intermolecular H-bonding via its linker amide groups. DEDOT-Amide-TPA is its methylated analogue, a tertiary amide, and therefore provides a direct comparison for the effects of H-bonding capabilities on hole transport. While long-range order was not observed in their solution-processed thin films, the crystal structures of these HTMs may be considered a best-case scenario for intermolecular interaction and provide insight into the relationship between packing and charge transport behaviour.

As expected, crystalline EDOT-Amide-TPA monomers exhibits both intra- and intermolecular H-bonding. The interactions between the amide linker and the dioxythiophene moiety on the core locks the molecule into a more planar conformation, which also enables close interaction between the secondary amide moieties on neighbouring molecules. Therefore, EDOT-Amide-TPA is seen to form strands of antiparallel oriented monomers. DEDOT-Amide-TPA is unable to H-bond via the amide linker and, additionally, takes on a less planar conformation. Like EDOT-Amide-TPA, DEDOT-Amide-TPA exhibits a lamellar type of structure, however, there is close packing between both parallel and antiparallel oriented monomers.

From ^{1}H-NMR titrations, which show the concentration dependent shift in EDOT-Amide-TPA amide and adjacent aromatic proton peaks, it appears that intermolecular H-bonding already occurs in concentrated solutions.[24] Strongly bound dimers are expected to remain stable during spin-coating. Therefore, binding energy reflects the likelihood of dimer presence in the amorphous thin films. These dimers represent a single hopping site with an overall dipole moment. The combination of dipole-dipole and H-bonding interactions in EDOT-Amide-TPA likely provides stability and directionality to its reduced dipole dimers. A high concentration of these dimers in the matrix would therefore reduce the energetic noise and would be consistent with the favourable experimental charge transport properties we observe.

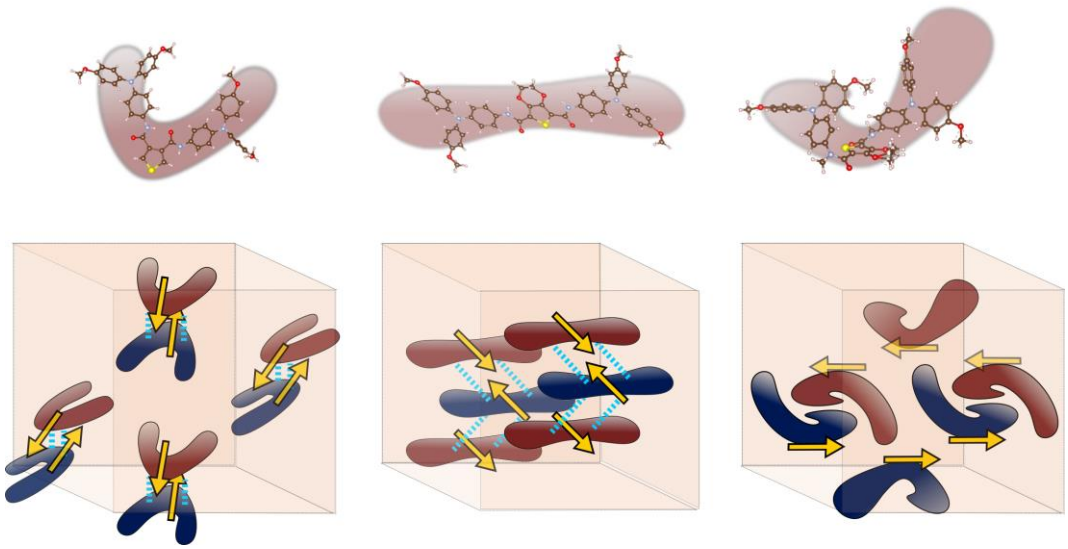

Figure 4.3 Graphical representation of the crystalline packing of TPA-BT (left), EDOT-Amide-TPA (centre) and DEDOT-Amide-TPA (right) molecules.[23-25]

4.6 Dimers in HTM crystal structures

Representative neighbouring pairs were extracted from the crystal structures of the amide HTMs, as shown in Figure ***4.4***. The coloured arrows indicate relative orientations of the molecule cores, with yellow arrows indicating antiparallel cores and red arrows indicating either parallel or orthogonal oriented cores. Table ***4.3*** gives the Debye dipole moments and binding energies of these pairs, from DFT calculations at the PBE0/def2-sv(p) level, as well as intermolecular distances and the relative orientation of their respective monomers.

Our calculations show the antiparallel dimers of these HTMs have an overall dipole moment of 0 D, and that this configuration leads to highest binding energies, between 0.8 and 0.9 eV. Therefore, once formed, these dimers are likely to remain stable during processing and under normal device operating conditions. When EDOT-Amide-TPA molecules are arranged antiparallel they exhibit a high binding energy and a quenched dipole, while a parallel arrangement results in a greatly enhanced overall dipole moment of 21 D. In DEDOT-Amide-TPA, parallel and antiparallel pairs extracted from the crystal show comparable binding energies, with just 0.2 eV higher binding energy for quenched dipole antiparallel pairs, so that once formed both arrangements are likely to be stable in the film.

Table 4.3 Properties of amide pairs extracted from X-ray diffraction[23-25], shown in Figure ***4.4*** above, with their theoretical dipole moments and binding energies, from DFT (PBE0/def2-sv(p)) calculations in vacuum carried out using Orca.

Pairs	Orientation	Dipole (D)	Binding Energy (eV)	Intermolecular Distance (Å):		
				Cores	Shortest	TPA N—N
1a	**antiparallel***	**0.0**	**0.86**	**4.0**	**2.7**	**5.0**
1b	antiparallel	0.0	0.31	15.5	2.7	10.9
1c	parallel	21.0	0.29	13.9	2.4	14.8
2a	**antiparallel**	**0.0**	**0.78**	**8.0**	**2.5**	**5.2**
2b	parallel	7.1	0.58	3.7	2.3	9.9
3a	**antiparallel***	**0.0**	**0.84**	**3.6**	**2.1**	**12.1**
3b	antiparallel	0.0	0.36	15.0	2.9	5.0
3c	antiparallel	0.0	0.29	9.7	2.7	9.0
3d	orthogonal	8.6	0.07	19.3	2.9	9.0

* Dimer exhibits H-bonding between amide linkers.

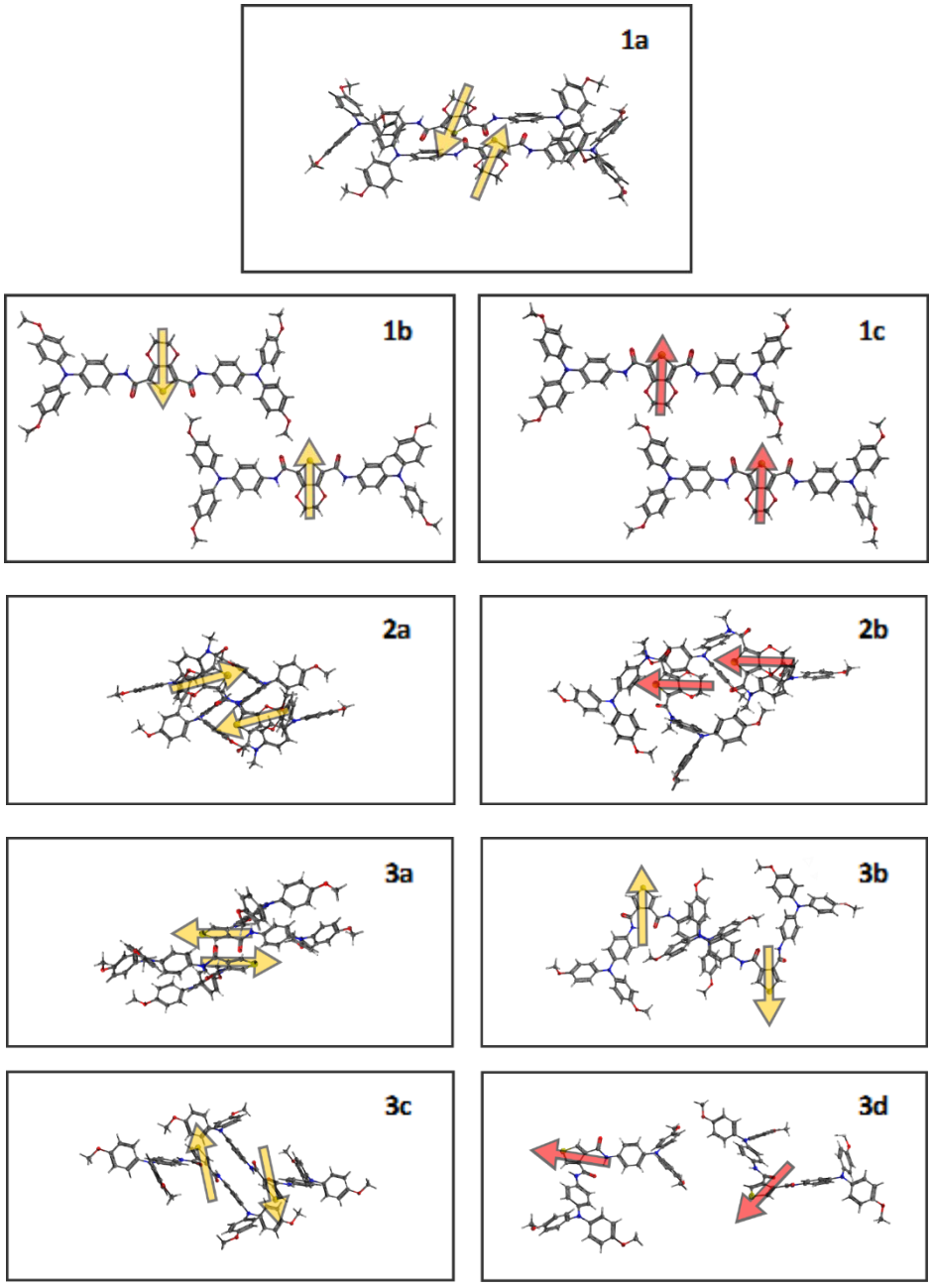

Figure 4.4 Close lying molecule pairs extracted from the crystal structures of EDOT-Amide-TPA (**1a-c**), DEDOT-Amide-TPA **(2a-b)** and TPA-BT **(3a-c)**, with arrows showing the relative orientation of their respective cores.[23-25]

We expect the proportion of quenched dipole dimers compared to dipole enhanced dimers to be greatest in the secondary amide HTM EDOT-Amide-TPA. While EDOT-Amide-TPA has the higher dipole moment, a high concentration of quenched dipole dimers could result in regions with low energetic noise width within the film. In DEDOT-Amide-TPA, the correlated energetic disorder in the film would remain high if both antiparallel and parallel oriented pairs are energetically favoured. If their concentration is low, quenched dipole dimers could in fact increase the complexity of the potential

energy landscape and act as charge traps. These findings are, therefore, consistent with the trend in the measured HTM conductivities of EDOT- and DEDOT-Amide-TPA.

Another secondary amide TPA-BT was also investigated for comparison with EDOT-Amide-TPA. It exhibits a lower conductivity than either EDOT-Amide-TPA or DEDOT-Amide-TPA in the pristine state (TPABT: 1.36416x10-9 S/cm), and it's pristine mobility (at 5.3×10^{-6} cm^2/Vs) is also lower than that of EDOT-Amide-TPA (3.9×10^{-5} cm^2/Vs).[23-25] However, upon doping the conductivity rises sharply and even at low doping concentrations TPA-BT performs better than EDOT-Amide-TPA until at 50% doping the conductivity reaches ~$4x10^{-5}$ S/cm, almost an order of magnitude greater than that of EDOT-Amide-TPA. The crystal structure of TPA-BT shows intramolecular H-bonding between the two amide linkers across the thiophene core, which locks the molecule into a planar conformation. Intermolecular H-bonding also occurs between neighbouring molecules via the amide linkers, which results in distinct dimers forming, in which the respective monomers are oriented antiparallel to one another.

Like EDOT-Amide-TPA and DEDOT-Amide-TPA, the TPA-BT antiparallel quenched dipole dimers were found to have a high binding energy (0.86 eV). Although orthogonal pairs are also formed, these have far lower binding energies. It is unclear why the trend in charge transport behaviour between the three amides investigated changes upon doping and how it relates to the packing behaviour of TPA-BT. TPA-BT has the lowest dipole moment of the three amides, which may reduce the energetic driving force for forming dimers, while doping could impact intermolecular interactions. Compared to TPA-BT, EDOT-Amide-TPA has the higher dipole moment. The disordered films of these molecules may consist of a mixture of fully disordered domains and regions of local order in the form of dimers or aggregates ordered aggregates. Assuming the number and distribution of dimers is equal, EDOT-Amide-TPA would still having an overall more complex potential energy landscape than TPA-BT and, therefore, lower mobility and conductivity.

4.7 Relaxed surface scan binding energies

Binding profiles for EDOT-Amide-TPA and DEDOT-Amide-TPA dimers were obtained by performing relaxed surface scans. EDOT-Amide-TPA monomer core-to-core distances were changed from 2.19-20 Å over 20 equidistant steps, and 2.19-1.19 Å over 10 equidistant steps. DEDOT-Amide-TPA monomer core-to-core distances were changed from 2.53 Å to 20 Å over 20 equidistant steps, and 2.53 Å to 1.53 Å over 10 equidistant steps. At each step a constrained geometry optimisation was carried out.

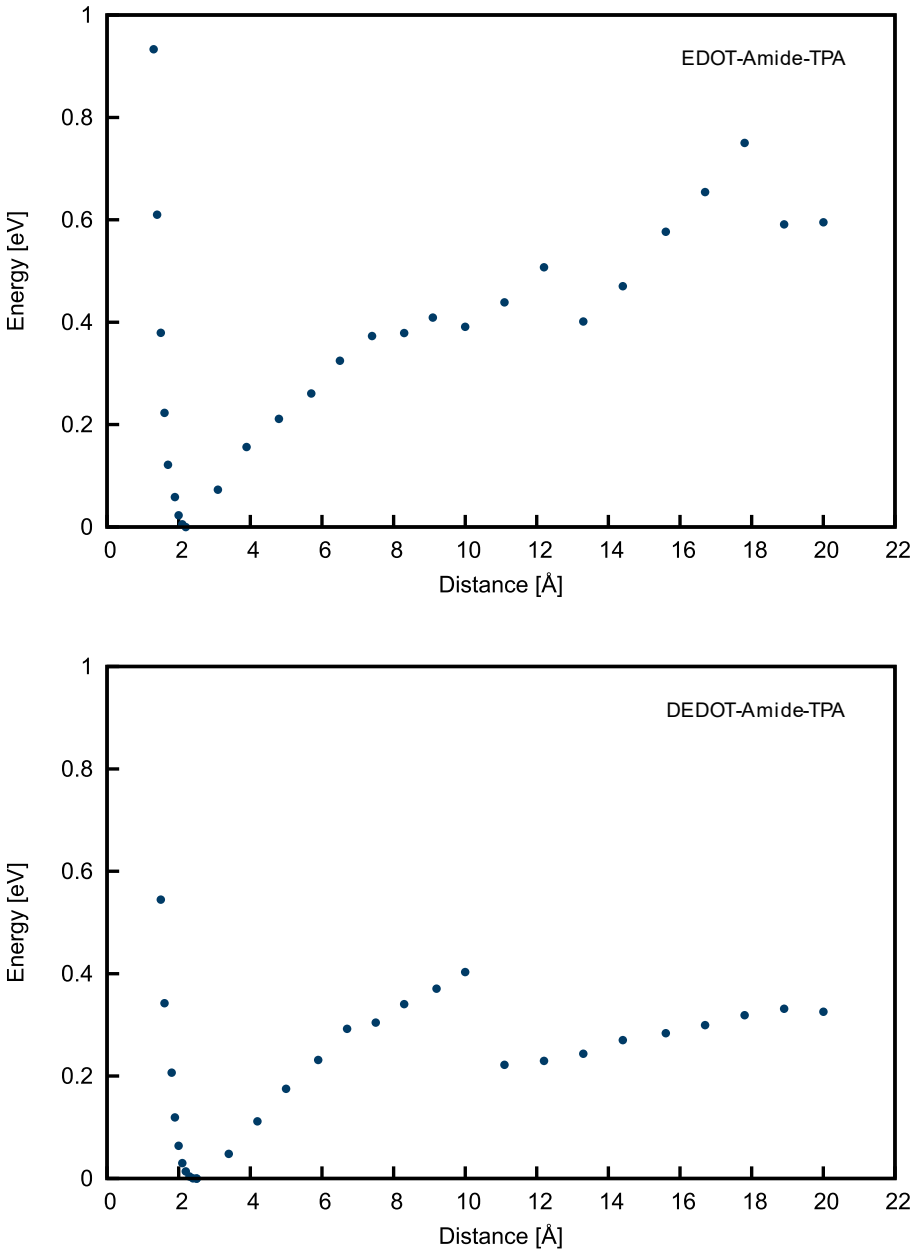

Figure 4.5 Reaction coordinate for dimers, showing the change in energy of the system as the distance between the respective monomers is increased.

These scans show a typical binding profile, where the systems have a minimum energy at an optimum intermolecular core-to-core distance, found to be 2.2 and 2.5 Å for EDOT-Amide-TPA and DEDOT-Amide-TPA respectively, that then increases dramatically as the monomers are brought closer together. As the systems are pulled apart, the energy increases and then plateaus as the intermolecular distance is increased. The binding profiles (***Figure 4.5***) do not show a smooth trend in energy change with intermolecular distance, as molecules can relax at each step in multiple ways. While the results obtained are not definitive, they do seem to indicate that the energy difference between the dimer and constituent monomer systems is higher in EDOT-Amide-TPA than in DEDOT-

Amide-TPA. The antiparallel crystal dimers (Table **3**) were found to have comparable high binding energies (EDOT-Amide-TPA 0.86 eV, DEDOT-Amide-TPA 0.78 eV). In contrast, the binding profiles suggest overall lower binding energies, as the relative orientations of the molecules during the surface scans were only fixed with respect to their core-to-core distances and monomer configurations were allowed to relax. The difference between the two HTMs, consistent with the trends discussed in section ***4.6*** above, indicate that there is a greater energetic advantage for EDOT-Amide-TPA to form dimers than DEDOT-Amide-TPA, which could serve as a driving force for dimerisation resulting in a higher proportion of dimers.

4.8 Dimer population

The formation of dimers in EDOT-Amide-TPA and DEDOT-Amide-TPA was explored via MD using the LAMMPS package, with force fields generated from QM Hessians obtained from DFT(PBE0/def2-sv(p)) calculations.[17] Simulations were performed over 1.14 x 10^7 timesteps, where each timestep was 0.01 fs, in which the systems containing 500 molecules underwent repeated heating and cooling cycles, between 300 and 1000 K under constant pressure. Heating cycles allow the system to overcome energetic barriers, so that more of the conformational space of the system can be accessed over the simulation run time. At the same time, the energy provided (1000 K = 0.09 eV) is not sufficient to break up any strongly bound dimers that form over the heating and cooling cycles. Intermolecular distances of all the molecules in the system were found, and those $\leq 5\text{Å}$ were identified as potential dimers. At the end of the simulation, the EDOT-Amide-TPA system was found to contain ~60 dimers, double the number of dimers found in the DEDOT-Amide-TPA system.

This mirrors the difference in binding energies found from the relaxed surface scans and may reflect the higher driving force for dimer formation in EDOT-Amide-TPA due to H-bonding. While these results are not conclusive and the formation of dimers under simulation conditions was found to be a rare event, the actual percentage of dimers formed could be much higher over larger timescales. This is especially true since, as we have seen from our binding energies, once dimers are formed, they are unlikely to break apart. If the potential energy difference between the dimer system and the monomer system is taken to represent the activation energy E_a required to break the dimer apart, then the rate at which this occurs is given by the Arrhenius equation, $k = Ae^{-\frac{E_a}{RT}}$, and is vanishingly small for both EDOT-Amide-TPA and DEDOT-Amide-TPA at below 373 K.

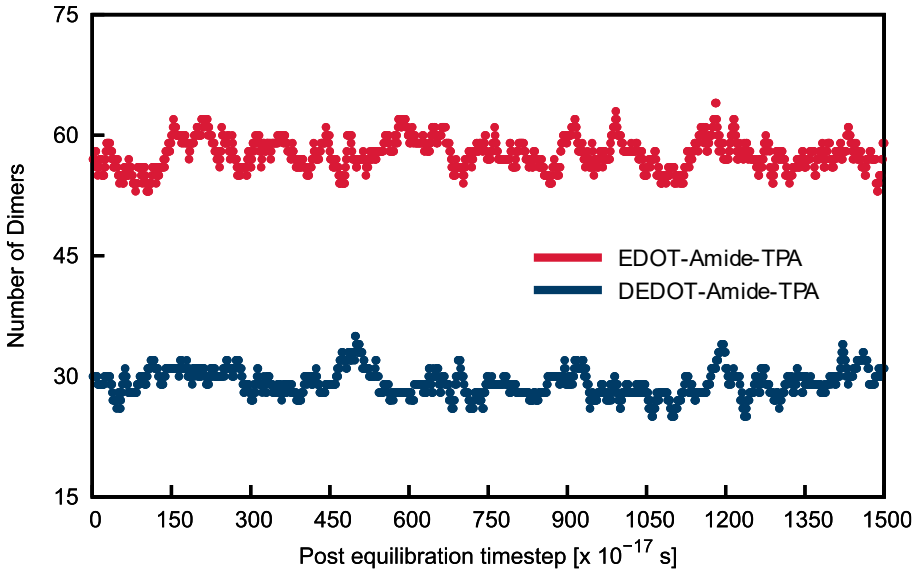

Figure 4.6 Number of dimers present in MD simulations of EDOT-and DEDOT-Amide-TPA systems consisting of 500 molecules, calculated for a snapshot of post equilibration timesteps.

4.9 KMC dimers simulations

The effect of dipole quenched dimers on the hole mobility of an otherwise disordered high dipole material was investigated using kinetic Monte Carlo (kMC) simulations, with code details given in *Chapter 2* (***2.4***). The HTM was represented as a cubic lattice of 200^3 hopping sites set 10 Å apart. The dipole moment on each site was initially given a magnitude of 5 Debye and oriented randomly as described previously (*Chapter 2*, section ***2.4***). For systems with non-zero dimer populations, neighbouring pairs were chosen at random from uniform distributions, and their dipole moments reset to 0 Debye, as follows. First, all sites were placed onto a 1-dimensional array of size N (where $N = N_x \cdot N_y \cdot N_z$). Next, a random number was drawn from a uniform distribution in the range $1{:}\,N$. The nearest index to that number was flagged as "part of a pair". If the same site was chosen more than once, another site was chosen until all the "part of a pair" sites were selected. This procedure was repeated until all "part of a pair" sites in the system were assigned. Once complete, a random neighbouring site was drawn from a uniform distribution for each site flagged "part of a pair". Finally, the dipole moment for each pair was set to zero. The Marcus hopping rate[2] for systems with different percentage dimer populations were found over a range of field strengths. Other parameters, given in Table ***4.4***, including the uncorrelated noise and reorganisation energy were kept

constant in order to definitively probe the effect of the percentage dimer population on the hole mobility.

Table 4.4 Parameter settings used in kMC simulations

Parameter	Description	Value	Units
E_{HOMO}	HOMO energy	0.0	eV
E_F	Fermi energy	0.0	eV
ρ_0	Initial charge density	10^{-5}	nm^{-1}
L	Lattice spacing	1	nm
γ	Inverse charge localisation	2.0	nm^{-1}
ω_0	Hopping attempt frequency	10^{12}	s^{-1}
ϵ_R	Relative permittivity	3.0	ϵ_0
d_M	Monomer Dipole	5.0	D
d_D	Dimer Dipole	0.0	D
N	System Dimensions	200	grid points

The dependence of the hole mobility, μ_h, on the applied electric field, E_{Field}, was found for systems with dimer populations ranging between zero and 42%. Figure ***4.7*** shows that when the data is fitted to a Poole-Frenkel-type equation ($\mu_h \propto e^{\beta\sqrt{E_{Field}}}$), we observe expected behaviour at electric field strengths of 4.0 - 9.5 x 10^5 V/cm, which can be used to extrapolate to the zero-field mobility. At typical experimental field strengths of 5 x 10^5 V/cm, the mobility increases logarithmically with the percentage dimer population, from 7±1 x 10^{-7} cm^2/Vs in a 0% dimer system to 2±0.5 x 10^{-6} cm^2/Vs in a 42% dimer system. In both the zero field and high field case, the mobility gradients are similar suggesting the dimer population results in a global increase in mobility independent of the effect of the strength of the applied electric field.

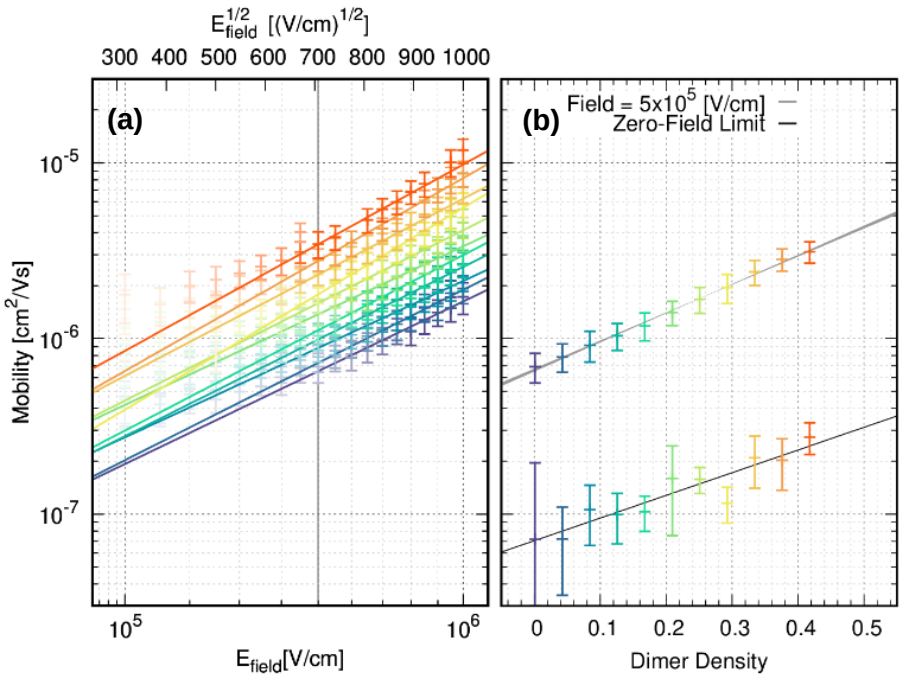

Figure 4.7 **(a)** Mobility against field at different dimer densities, and **(b)** mobility against dimer density at a field strength of 5 x 10^5 V/cm and at zero field, for systems with dimer densities ranging from 0% (indigo) to 42% (red).

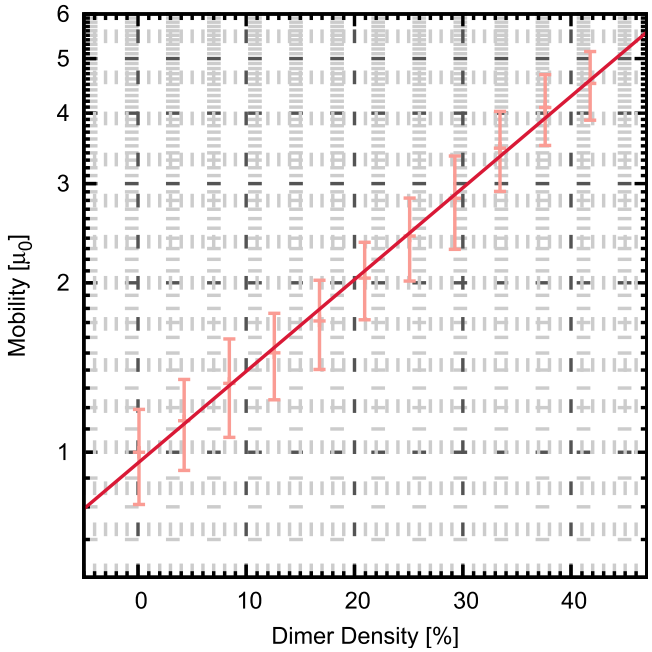

Figure 4.8 Normalised mobility as a function of the density of dimers in the system.

Figure ***4.8*** shows the trend in the average normalised mobility as calculated by kMC, with error bars indicating the standard deviation. We see that increasing the dimer population in systems to just 30% results in an almost three-fold increase in the normalised mobility. If there is a large enough energetic driving force for stable dimers to form, the dimer population in an otherwise amorphous film could indeed be quite high. While monomer dipoles remain high, the presence of quenched dimers serve to reduce the correlated noise width and could provide efficient hopping routes for holes to move through the material.

As we saw earlier, the dipole moment enters into the exponential term of the hopping rate equation.[2] Therefore, while other parameters, such as the electronic coupling and lattice parameter also influence the mobility, the effect of the dipole is likely to be dominant. The ability of high dipole disordered HTMs, such as EDOT-Amide-TPA and TPA-BT, to form stable H-bonded dipole-quenched dimers, is consistent with their enhanced experimental charge transport properties when compared with other high dipole materials such as DEDOT-Amide-TPA that are unable to H-bond. It is worth noting that the kMC simulations were run for fully disordered systems. Therefore, introducing some degree of dipole ordering would further increase the mobility.[1]

4.10 Conclusions

The hopping rate has an exponential negative dependence on the energetic noise width. While the energetic noise width is generally assumed to scale with the dipole moment strength, in our molecules the experimental mobility was found to increase with the theoretical dipole moment. KMC calculations showed that while the global ordering of dipoles does not account for this unexpected trend, in high dipole systems local effects dominate as charges percolate through a small portion of the system via energetically accessible routes. Therefore, the effect of the environment and intermolecular interactions, like H-bonding, on the properties of hopping sites must be taken into account. In fact, controlling intermolecular interactions is a key feature of HTM design, with examples in the literature showing improvements in mobility both when aggregation is suppressed on the one hand, and when self-assembly of molecules into stable ordered domains is controlled, on the other.

The level of correlated and uncorrelated disorder may be overestimated in systems where the conformational freedom of molecules is restricted, as would be the case in a thin film, leading to an underestimation in predicted mobilities. The distribution of HOMO energies and dipole moment strengths in some of the materials presented in *Chapter 3*, Fu-, Th-, Ph-Inv and Ph-OMeTPA, was explored more thoroughly via MD simulations of their thin films to account for the effect of the environment. However, as was the case for their single molecule results in *Chapter 3*, no significant relationship was found between the global distribution width and the experimental mobilities. Results for reorganisations based on MD generated conformations were inconclusive.

The propensity of high dipole molecules to form aggregates such as dimers via non-covalent interactions such as H-bonding within otherwise amorphous films, may account for the larger than expected mobilities measured. Dimers could reduce the energetic disorder and provide favourable pathways for hole transport. With this in mind, the relationship between the solid-state packing and charge transport properties of three amide-based HTMs were investigated. Crystal structures of our secondary and tertiary amide HTMs highlight differences in packing due to H-bonding. EDOT-Amide-TPA molecules were found adopt a planar conformation and pack closely via H-bonding, in strands of antiparallel oriented monomers. Dimers arranged in this way were found to have a high binding energy and a quenched dipole moment. Dipole-quenched H-bonded dimers in EDOT-Amide-TPA were found to be energetically favoured in contrast with those of the control molecule, DEDOT-Amide-TPA which is unable to H-bond. Our MD simulations show that, indeed, the EDOT-Amide-TPA system formed double the number of dimers in the DEDOT-Amide-TPA system, and the actual percentage of dimers forming is likely to be higher over longer timescales since these are unlikely to break apart once formed. From kMC simulations of fully disordered high dipole systems, we find that the mobility

increases sharply as the dimer population is increased, although, as we saw in *Chapter 3*, the overall mobility remained quite low. Nevertheless, dimer formation together with some level of global ordering of dipole moments may explain the larger than expected mobilities of high dipole amorphous HTMs like EDOT-Amide-TPA. Therefore, H-bonding and dipole-dipole interactions may be used together as a design feature, to control the energetic disorder in their thin films, and allow us to exploit the easy synthesis of simple polar HTMs.

References:

1. T. Pope, Y. Giret, M. Fsadni, P. Docampo, C. Groves and T. Penfold, *Org. Electron.*, 2023, **115**, 106760.
2. R. A. Marcus, *Annu. Rev. Phys. Chem.*, 1964, **15**, 155.
3. A. Miller and E. Abrahams, *Phys. Rev.*, 1960, **120**, 745.
4. R. Coehoorn and P. A. Bobbert, *Phys. Status Solidi A*, 2012, **209**, 2354.
5. P. Borsenberger and H. Bässler*, J. Chem. Phys.*, 1991, **95**, 5327; 120. A. Dieckmann, H. Bässler and P. Borsenberger, *J. Chem. Phys.*, 1993, **99**, 8136; P. Friederich, V. Meded, A. Poschlad, T. Neumann, V. Rodin, V. Stehr, F. Symalla, D. Danilov, G. Lüdemann, R. F. Fink, I. Kondov, F. von Wrochem and W. Wenzel, *Adv. Funct. Mater.*, 2016, **26**, 5757.
6. P. Friederich, A. Fediai, S. Kaiser, M. Konrad, N. Jung and W. Wenzel, *Adv. Mater.*, 2019, **31**, 1808256.
7. S. Wang, M. Kappl, I. Liebewirth, M. Müller, K. Kirchhoff, W. Pisula and K. Müllen, *Adv. Mater.*, 2012, **24**, 417-420.
8. T. Malinauskas, D. Tomkute-Luksiene, R. Sens, M. Daskeviciene, R. Send, H. Wonneberger, V. Jankauskas, I. Bruder and V. Getautis, *ACS Appl. Mater. Interfaces*, 2015, **7**, 11107–11116.
9. T. Qin, W. Huang, J.-E. Kim, D. Vak, C. Forsyth, C. R. McNeill and Y.-B. Cheng, *Nano Energy*, 2017, **31**, 210-217.
10. H. N. Tsao, D. Cho, J. W. Andreasen, A. Rouhanipour, D. W. Breiby, W. Pisula and K. Müllen, *Adv. Mater.*, 2009, **21**, 209; H. N. Tsao, D. Cho, I. Park, M. R. Hansen, A. Mavrinskiy, D. Y. Yoon, R. Graf, W. Pisula, H. W. Spiess and K. Müllen, *J. Am. Chem. Soc.*, 2011, **133**, 2605.
11. J. Song, L. Ye, C. Li, J. Xu, S. Chandrabose, K. Weng, Y. Cai, Y. Xie, P. O'Reilly, K. Chen, J. Zhou, Y. Zhou, J. M. Hodgkiss, F. Liu and Y. Sun, *Adv. Sci.*, 2020, **7**, 2001986.
12. J. Wang, X. Wu, Y. Liu, T. Qin, K. Zhang, N. Li, J. Zhao, R. Ye, Z. Fan, Z. Chi and Z. Zhu, *Adv. Energy Mater.*, 2021, **11**, 2100967.
13. Q. Cheng, H. Chen, F. Yang, Z. Chen, W. Chen, H. Yang, Y. Shen, X.-M. Ou, Y. Wu, Y. Li and Y. Li, *Angew. Chem. Int. Ed.*, 2022, **61**, e202210613.
14. F. Wuerthner, *Acc. Chem. Res.*, 2016, **49**, 868−876
15. F. Würthner and K. Meerholz, *Chem. Eur. J.*, 2010,**16**, 9366−9373.
16. L. Martínez, R. Andrade, E. G. Birgin, and J. M. Martínez, *J. Comput. Chem.*, 2009, **30**, 2157.
17. A. P. Thompson, H. M. Aktulga, R. Berger, D. S. Bolintineanu, W. M. Brown, P. S. Crozier, P. J. in't Veld, A. Kohlmeyer, S. G. Moore, T. D. Nguyen, R. Shan, M. J. Stevens, J. Tranchida, C. Trot and S. J. Plimpton, *Comput. Phys. Comm.*, 2022, **271**, 10817.

18. J. P. Perdew,K. Burke and M. Ernzerhof, *Phys. Rev. Lett.*, 1996, **77**, 3865; C. Adamo and V. Barone, *J. Chem. Phys.*, 1999, **110**, 6158.
19. F. Weigend and R. Ahlrichs, *Phys. Chem. Chem. Phys.*, 2005, **7**, 3297; F. Weigend, *Phys. Chem. Chem. Phys.*, 2006, **8**, 1057.
20. F. Neese, *Wiley Interdiscip. Rev. Comput. Mol. Sci.*, 2012, **2**, 73; F. Neese, *Wiley Interdiscip. Rev. Comput. Mol. Sci.*, 2017, **8**, e1327.
21. S. Grimme, *J. Comput. Chem.*, 2006, **27**, 1787; S. Grimme, S. Ehrlich and L. Goerigk, *J. Comput. Chem.*, 2011, **32**, 1456.
22. F. Weigend and R. Ahlrichs, *Phys. Chem. Chem. Phys.*, 2005, **7**, 3297.
23. F. Wolf, M. T. Sirtl, S. Klenk, M. H. H. Wurzenberger, M. Armer, P. Dörflinger, P. Ganswindt, R. Guntermann, V. Dyakonov and Thomas Bein, *CrystEngComm*, 2023, **25**, 3142-3149; M. L. Petrus, K. Schutt, M. T. Sirtl, E. M. Hutter, A. C. Closs,J. M. Ball, J. C. Bijleveld, A. Petrozza, T. Bein, T. J. Dingemans,T. J. Savenije, H. Snaith and P. Docampo, *Adv. Energy Mater.*, 2018, **8**, 1801605.
24. B. Vella, M. Fsadni, T. Pope, M. Giza, F. J. Angus, I. Shmarov, P. L. Lalaguna, M. Cariello, C. Wilson, M. Kadodwala, T. J. Penfold, P. Docampo and G. Cooke, *J. Mater. Chem. A*, 2024 (*accepted*).
25. E. A. A. Alkhudhayr, D. Sirbu, M. Fsadni, B. Vella, B. T. Muhammad, P. Waddell, M. R. Probert, T. J. Penfold, T. Hallam, E. A. Gibson and P. Docampo, *ACS Appl. Energy Mater.*, 2023, **6**, 22, 11573.

5 Synthesis and Characterisation of HTMs

5.1 Introduction

In the previous chapters we have shown that out of the single molecule properties we investigated, the dipole moment plays a significant role in determining the mobility.[1] A high dipole moment may provide a driving force for the ordering of molecules at the local level, giving rise to quenched dipole aggregates, including dimers, that provide energy efficient routes for hole transport through an otherwise disordered material.[2,3] Preliminary studies with amide HTMs indicate that the ability to H-bond may regulate packing behaviour. ^{1}H NMR studies indicate that intermolecular H-bonding occurs in concentrated solutions of the secondary amides, EDOT-Amide-TPA and DEDOT-Amide TPA, with theoretical studies showing that dipole quenched hydrogen-bonded dimers are unlikely to break apart under standard device processing and operating conditions.[2] Therefore, designing HTMs with tuned intermolecular dipole-dipole and hydrogen-bonding interactions to regulate the ordering of molecules in solution processed films could improve the charge transport characteristics and stability of their devices.

To investigate the effect of the dipole moment and H-bonding on mobility, we designed a series of high dipole materials containing secondary and tertiary amide linkers as well as a urea-linked molecule. These are asymmetric donor-acceptor (D-A) type molecules, which are not fully conjugated due to the partial double bond character of the linkers. The TPA donor side unit common to all the molecules is prepared via a well-established literature procedure[4], while the functionalised cores were commercially available. The secondary and tertiary thiophene amides are asymmetric analogues of TPA-BT, which was found to have superior charge transport properties to EDOT-Amide-TPA and is competitive with the state-of-the-art spiro-OMeTAD in terms of cost, performance and stability.[2,5] The anisole unit, was chosen to provide further simple and low-cost amide-, and urea-linked HTM examples.

Asymmetric molecules were chosen for their simplicity and efficient synthesis, with the TPA moeity acting as a good donor unit[6] which helps to increase solubility and reduce excessive aggregation[7]. As we saw in *Chapter 1*, small molecule organic HTMs for PSCs tend to have a linear D-A-D or starburst

structure, with few examples of simple D-A molecules. Various literature examples show that D-A HTMs tend to perform worse than their D-A-D counterparts with lower mobilities, possibly due to the smaller area of the HOMO and weaker intermolecular interactions, and lower glass transition temperatures which may be attributed to a lower molecular weight[8,9] However, some D-A HTMs-based PSCs have been shown to yield high efficiencies.[10,11]

Characterisation of TPA-BT was performed by Benjamin Vella at the University of Glasgow, who also carried out some of the electrochemical and optical characterisations of molecules (***Figures 5.7***, ***5.8*** *and* ***5.9(a)***). High resolution atomic mass spectroscopy (HRAM) was performed by the EPSRC UK National Mass Spectrometry Facility (NMSF) at Swansea University. X-ray crystallography and structure elucidation of TPA-BT was performed by Dr Paul Waddell at Newcastle University. Experimental details are provided in section ***5.6***, below. Part of this work has been published:

B. Vella, M. Fsadni, T. Pope, M. Giza, F. J. Angus, I. Shmarov, P. L. Lalaguna, M. Cariello, C. Wilson, M. Kadodwala, T. J. Penfold, P. Docampo and G. Cooke, *J. Mater. Chem. A*, 2024 (*accepted*).

E. A. A. Alkhudhayr, D. Sirbu, M. Fsadni, B. Vella, B. T. Muhammad, P. Waddell, M. R. Probert, T. J. Penfold, T. Hallam, E. A. Gibson and P. Docampo, *ACS Appl. Energy Mater.*, 2023, **6**, 22, 11573.

5.2 HTM series

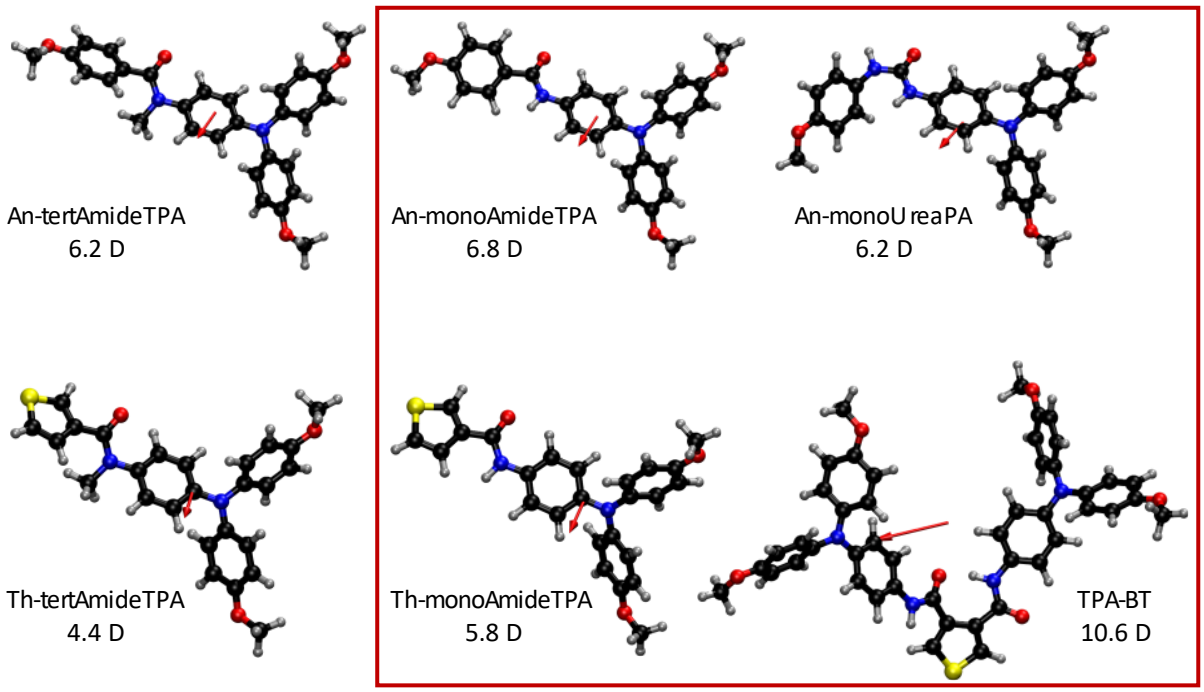

Figure 5.1 HTM series with different H-bonding capabilities and their Debye dipole moment magnitudes and directions (red arrow), with synthesised compounds in red box.

A series of molecules was designed to test the effect of the dipole moment and packing behaviour on the charge transport properties of HTMs. The series of HTMs contain secondary, tertiary amide and urea linker moieties within their structure, giving them different abilities to H-bond. The secondary amide and urea analogue linker nitrogens allow the molecules interact via simple and bifurcated intermolecular H-bonding, in contrast with the nitrogen linkers on the tertiary amide HTMs.

The molecules were investigated by DFT using Orca (v. 5)[12] to extract key properties. HTM geometries were initially optimised using PBE0/def2-sv(p)[13], before dipole moments and frontier orbital energies were recalculated with the C-PCM implemented to approximate solvation effects in dichloromethane. The calculated dipole moments of the three asymmetric molecules were found to be high (4.4-6.8 D) when compared with spiro-OMeTAD (3.26 D) and some of the molecules explored previously in *Chapter 1*, although they are significantly lower than both amide HTMs TPA-BT (10.6 D) and EDOT-Amide-TPA (13.4 D). The high dipole moment may provide an additional driving force for molecules to align antiferroelectrically to one another with respect to the direction of their respective dipole

moments.[3] The similar dipole moment strengths across the anisole series allows us to better investigate the effect of H-bonding. While the asymmetric analogue of TPA-BT, and An-monoAmideTPA allows us to compare the effect of the dipole moment strength. Comparing larger TPA-BT with two TPA units that can act as potential hopping sites, with its asymmetric counterpart Th-monoAmideTPA could also give valuable insights.

Four out of the six planned molecules were synthesised, as will be described in section ***5.3*** below, and preliminary conductivity, UV-visible absorption, fluorescence emission and cyclic voltammetry (CV) measurements were obtained for An-monoUreaTPA, Th- and An-monoAmideTPA. The tertiary amide analogues were not synthesised due to time constraints, although this might be achieved by reaction of the secondary amides with lithium diisopropylamide (LDA) and the mild methylating agent trimethyl phosphate.[14]

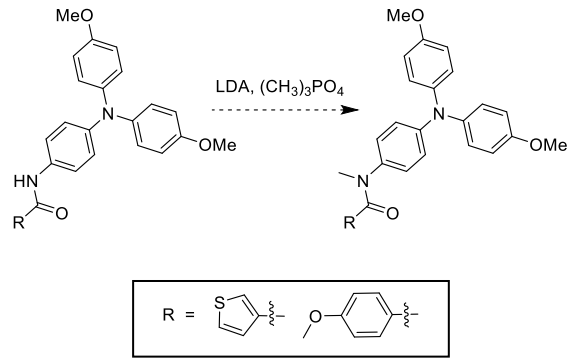

Scheme 5.1 Synthesis of asymmetric tertiary amide HTMs

5.3 Synthesis of HTMs

The aim was to generate a series that would enable further investigations into the role of H-bonding, packing and the dipole moment on charge transport characteristics. It is expected that H-bonding and strong dipole-dipole interactions would provide an energetic driving force for molecules to form strongly bound quenched dipole dimers. Therefore, we would expect to see the urea- and amide-linked HTMs to exhibit higher mobilities and conductivities than their tertiary amide counterparts, due to a reduction in the energetic disorder of the material. Taking advantage of the simplicity of condensation chemistry four novel materials, three amides, including two asymmetric amides, and an asymmetric urea molecule were successfully synthesised. TPA-BT is a symmetric secondary amide, while Th-monoAmideTPA is its asymmetric analogue. An-monoAmideTPA differs from Th-monoAmideTPA by its core, and An-monoUreaTPA is its urea analogue. All four molecules contain the

para-substituted OMe-TPA side units for which 4-Amino-4',4''-dimethoxytriphenylamine was synthesised via a modified literature procedure.[4] In the synthesis of TPA-BT, the dicarbonyl dichloride functionalised thiophene core was synthesised in one step via a literature procedure.[15] The synthesis of the asymmetric molecules was simplified by using commercially available functionalised cores.

5.3.1 Synthesis of functionalised TPA side unit

4,4'-Dimethoxy-4''-nitrotriphenylamine was synthesised via a modified ligand-free Ullman-type nucleophilic aromatic substitution reaction from commercial 4-iodoanisole with 4-nitroaniline, in the presence of metallic copper, potassium carbonate and 18-crown-6 as phase transfer catalyst.[16] The reduction of the nitro compound, by means of hydrazine monohydrate in the presence of Pd/C in refluxing tetrahydrofuran, afforded 4-amino-4',4''-dimethoxytriphenylamine which was used immediately in the subsequent condensation reactions due to its known air sensitivity.[4]

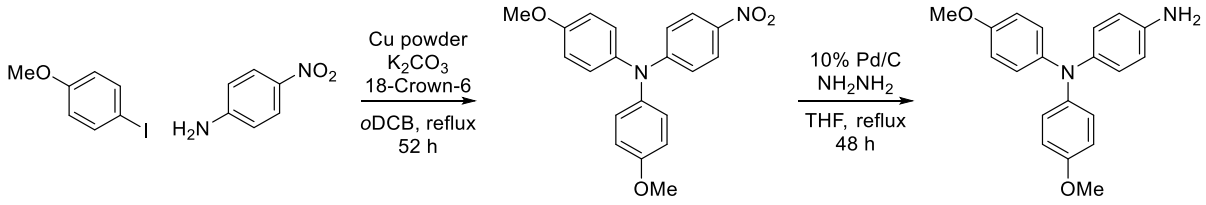

Scheme 5.2 Synthesis of functionalised TPA side unit

5.3.2 Synthesis of TPA-BT

TPABT was synthesised by the one-pot nucleophilic addition/elimination reaction of thiophene-3,4-dicarbonyl dichloride and 4-amino-4',4''-dimethoxytriphenylamine, illustrated in scheme ***5.3***, the presence of an excess of triethylamine to capture eliminated HCl. After refluxing for 15 minutes the product already began to form as a precipitate and the amine starting material appeared to be consumed by TLC. The reaction was allowed to proceed further at room temperature to ensure completion and the crude precipitate was readily filtered off. Column chromatography and recrystallisation of the crude was performed to ensure the product was of high purity, resulting in a significant drop in mass from 6.95 g to 2.47 g, representing a yield of 22%, likely due to the removal of approximately 4 g of the solid ammonium salt by-product which is known to be insoluble in tetrahydrofuran and petroleum ether.

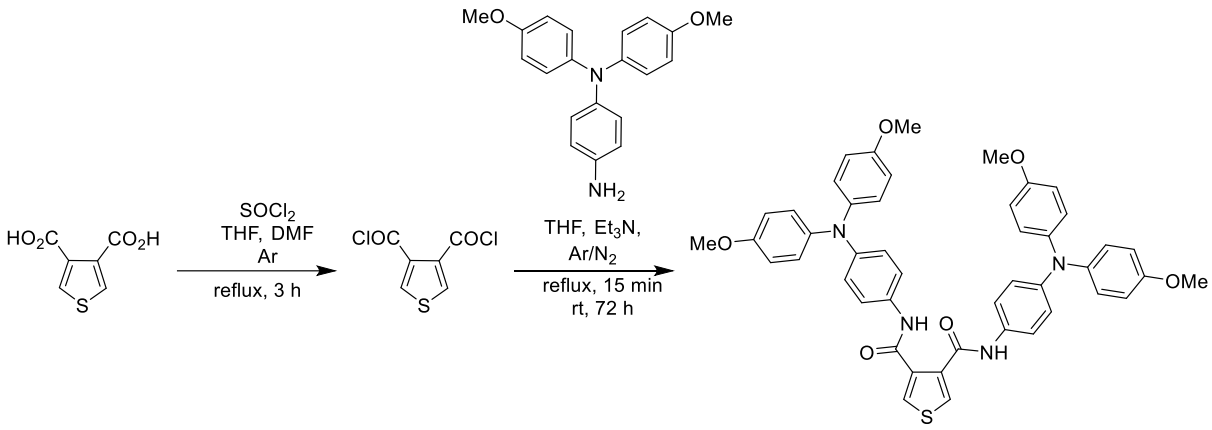

Scheme 5.3 Synthesis of TPA-BT

^{1}H NMR spectroscopy of the product showed the appearance of a new singlet compared to the starting materials at 10.33 ppm, which is attributed to protons on the newly formed amide group. The peak of the amide protons has an integration ratio of 1:6 with the singlet at 3.80 ppm, assigned to the 12 equivalent protons on the four triphenylamine methoxy groups. The product was further confirmed by high-resolution mass spectrometry, which showed the protonated parent ion (*m/z* = 777) with the expected isotope mass distribution pattern.

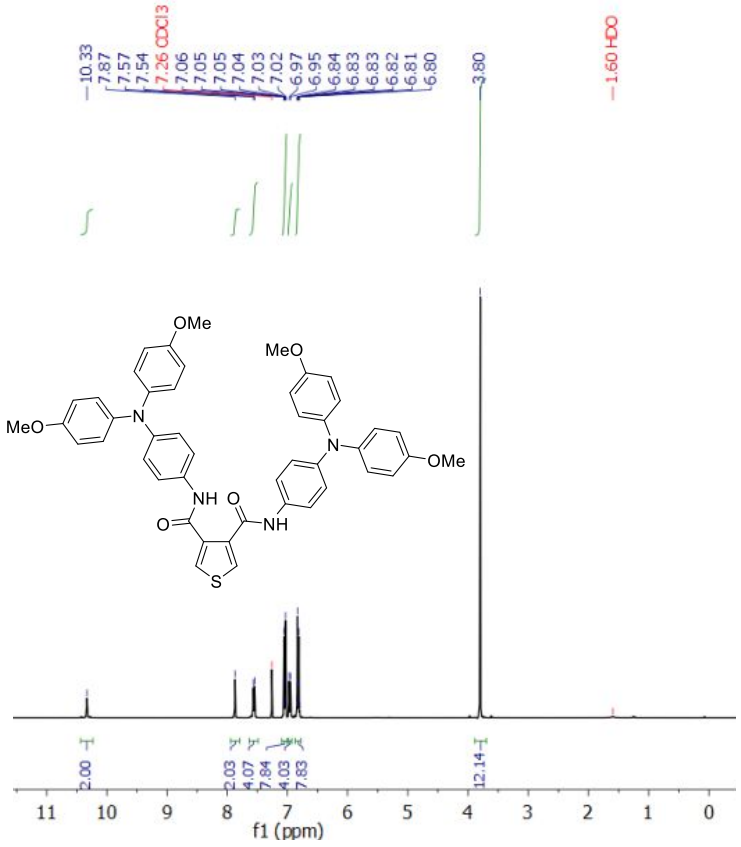

Figure 5.2 ^{1}H NMR (400 MHz, $CDCl_3$) spectrum of TPA-BT

5.3.3 Synthesis of asymmetric amide analogues

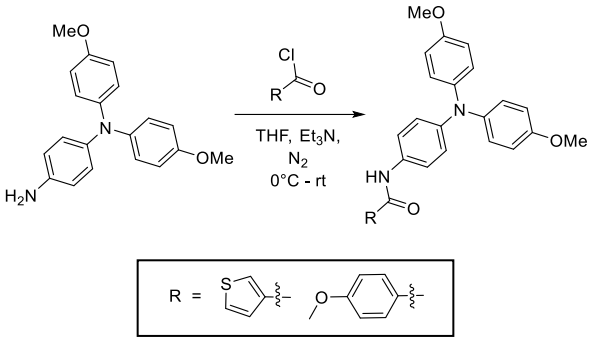

Scheme 5.4 Synthesis of the asymmetric amides, Th-monoAmideTPA and An-monoAmideTPA.

The synthesis of the asymmetric TPA-BT analogue Th-monoAmideTPA and An-monoAmideTPA proceeds via the same mechanism described above, starting with commercial thiophene-3-carbonyl chloride and 4-methoxybenzoyl chloride, respectively. However, the reactions were performed at a lower temperature which may contribute to the significantly higher yields obtained when compared to TPA-BT. In the case of TPA-BT, the reaction is performed at a higher temperature to ensure the double condensation product forms. The second addition/elimination reaction likely proceeds more slowly since intramolecular H-bonding between the acyl chloride carbonyl oxygen and newly formed amide proton across the thiophene core is expected to stabilise the monosubstituted intermediate. In addition to this, the large TPA side unit may hinder further addition of a second bulky 4-amine-4',4''-dimethoxytriphenylamine molecule and the triethylamine required for elimination of the proton and chloride moieties. As the mono substituted product is insoluble in THF, reflux and vigorous stirring also ensure reaction goes to completion. However, at higher temperature, side reactions are likely to occur as the diacyl chloride and TPA units are moisture and air sensitive. The crude product was quenched with brine and extracted with ethyl acetate, which allows for the facile separation from the triethylammonium chloride side-product. After column chromatography and a second bicarbonate and brine wash the products were isolated. Th-monoAmideTPA was collected as a pale yellow semi-solid with 91% yield, while An-monoAmideTPA was a pale brown semi-solid with 87% yield.

^{1}H NMR spectroscopy of the products again showed the appearance of a new peak downfield compared to the starting materials, which can be attributed to proton on the newly formed amide group. In Th-monoAmideTPA this is a singlet at 9.93 ppm, and in An-monoAmideTPA this is a multiplet at 10.01 ppm. The two equivalent triphenylamine methoxy groups on each amide appear as singlets at 3.73 and 3.72 ppm for Th- and An-monoAmideTPA, respectively, and have an integral of 6 each.

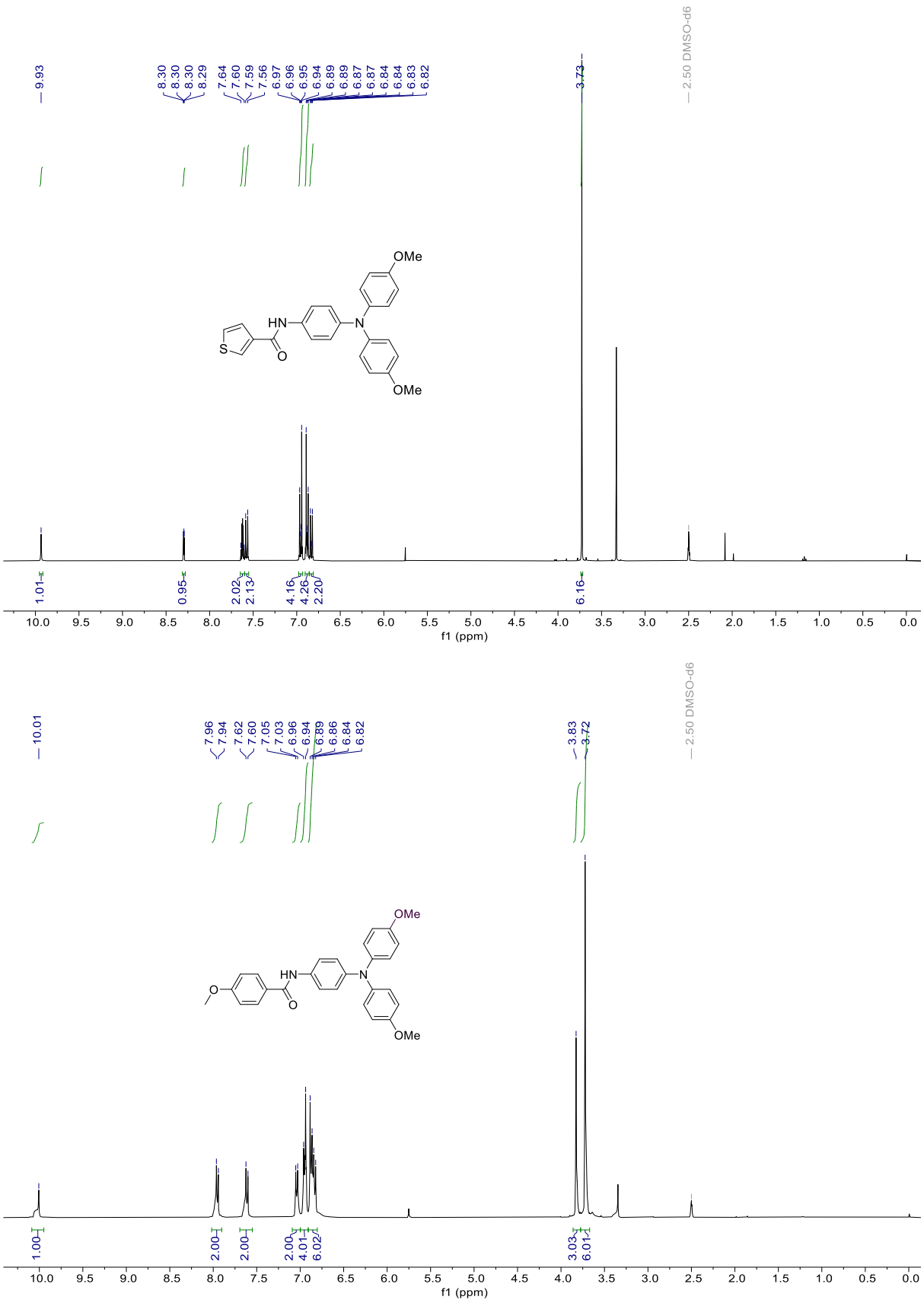

Figure 5.3 ^{1}H NMR (400 MHz, DMSO-d_6) spectra of Th-monoAmideTPA (top) and OMe-Ph - monoAmideTPA (bottom)

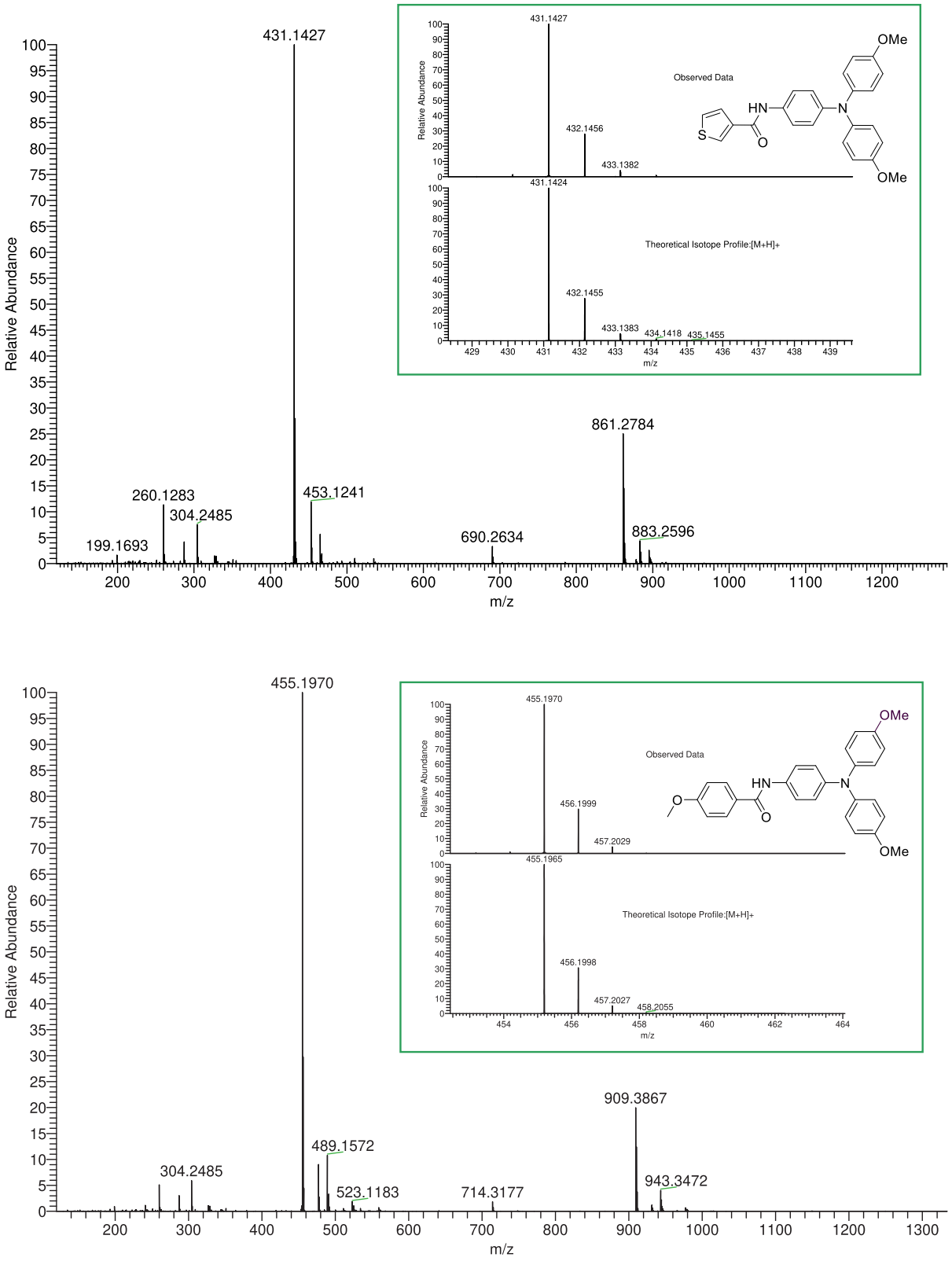

Figure 5.4 FTMS (nESI$^+$) of Th-monoAmideTPA (top) and OMe-Ph-monoAmideTPA (bottom).

An-monoAmideTPA has an additional singlet at 3.83 with an integral of 3, which is designated to the benzoyl core methoxy protons. High-resolution mass spectrometry of the products found the protonated parent ions, *m/z* = 431.1 and *m/z* = 455.2, in highest relative abundance with their expected isotope mass distribution patterns, confirming the successful synthesis of Th-monoAmideTPA and An-monoAmideTPA, respectively.

5.3.4 Synthesis of asymmetric urea analogue

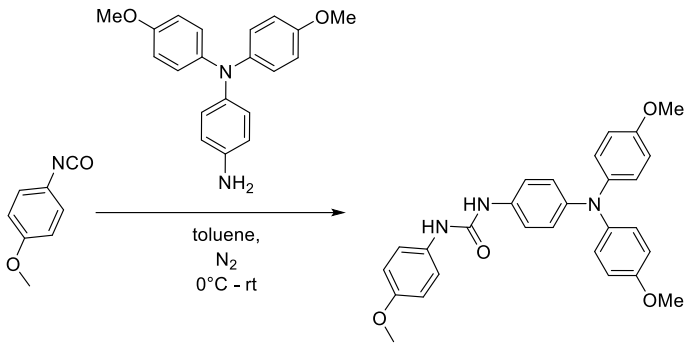

Scheme 5.5 Synthesis of the asymmetric urea compound An-monoUreaTPA

The urea analogue An-monoUreaTPA was synthesised from 4-amino-4',4''-dimethoxytriphenylamine and 4-methoxyphenyl isocyanate, as illustrated in scheme ***5.5***. The electron poor isocyanate carbon readily undergoes nucleophilic attack by amines at low temperatures, giving rise to the urea addition product. [17] An-monoUreaTPA precipitated out of the toluene solution and was isolated in high purity by ^{1}H NMR and 77% yield by simple filtration.

The product was further confirmed by solid state high-resolution mass spectrometry (ASAP+), which showed the protonated parent ion (m/z = 470.2) with the expected isotope mass distribution pattern. Although a "soft" ionisation method was applied, the parent ion has a low relative abundance with the highest peak m/z = 321.2 possibly due to protonated 4-amino-4',4''-dimethoxytriphenylamine resulting from fragmentation at the urea linker group.

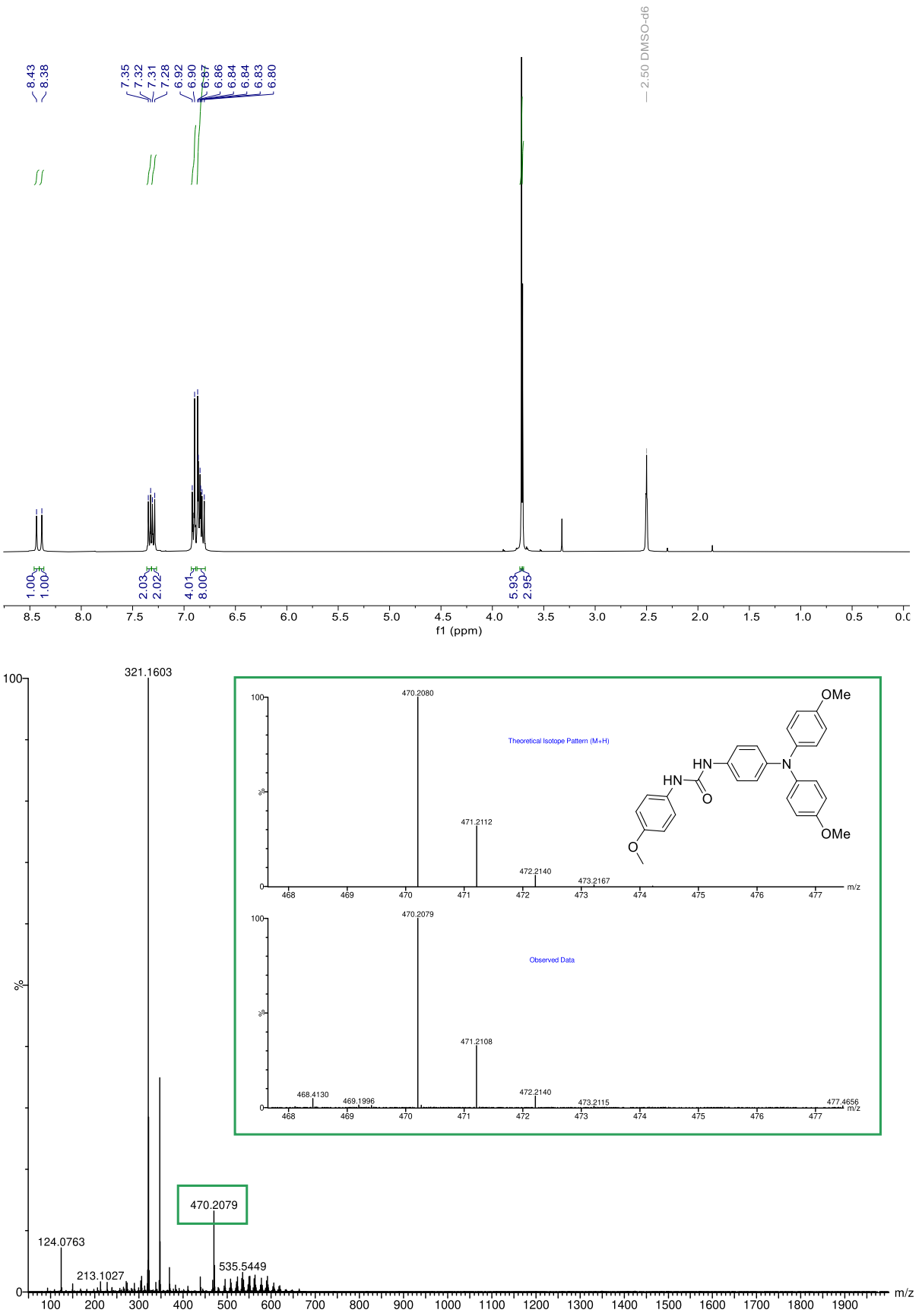

Figure 5.5 An-monoUreaTPA ^{1}H NMR (400 MHz, DMSO-d_6) (top) and TOF-MS (ASAP+) (bottom) spectra.

5.4 Preliminary electrochemical and optical characterisation of HTMs

As discussed in *Chapter 1*, a high conductivity is an essential property for high performing HTMs and is proportional to the charge carrier mobility. To gain insights into the charge transport properties of our materials, lateral conductivity measurements on thin films were performed with increasing concentrations of the p-dopant FK209. Further properties were investigated to look into the potential of our molecules as HTMs for PSCs. High transparency of the HTM ensures that light can pass through the HTL to the absorbing perovskite layer and prevents parasitic losses. Therefore, the UV-visible absorption spectra of our HTMs with different concentrations of the dopant FK209 were measured. Alignment of the HTM HOMO energy level with the perovskite valence band is required to ensure efficient hole extraction, while the LUMO energy level must be higher than the perovskite conduction band in order to act as an electron blocking layer. Therefore, frontier orbital energies were estimated both theoretically, via DFT (PBE0/def2-sv(p)) calculations, and experimentally, from cyclic voltammery and optical spectra..

5.4.1. Conductivity

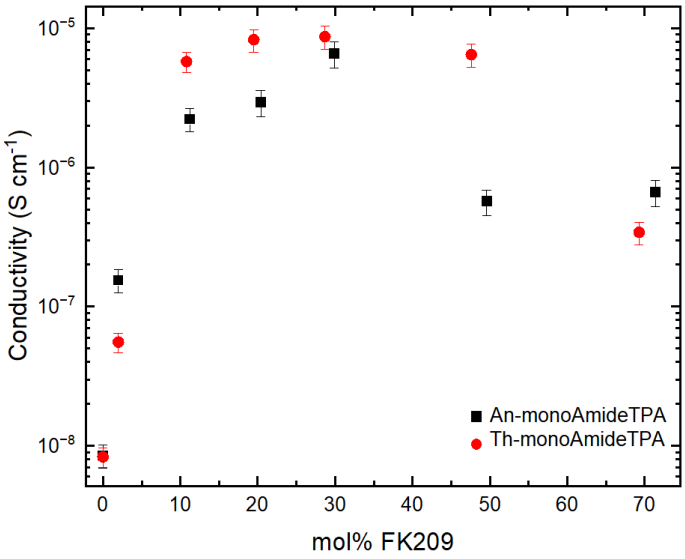

Figure 5.6 Calculated conductivities of our HTMs against extent of doping with FK209.

To gain insights into the charge transport properties of our materials, lateral conductivity measurements on thin films were performed. Thin films of our HTMs with increasing amounts of FK209, were prepared by solution spin-coating onto patterned ITO substrates. Like many organic HTMs, including EDOT-Amide-TPA and TPA-BT,[4,5] the conductivities of An- and Th-monoAmideTPA are very low in their pristine state. The p-type cobalt complex dopant, tris(2-(1*H*-pyrazol-1-yl)-4-*t*-

butylpyridine)cobalt(III) tri[hexafluorophosphate] (FK209) has been shown to undergo a redox reaction with spiro-OMeTAD, in which Co(III) is reduced to Co(II) with the concomitant oxidation of the HTM to its mono-cation radical species Spiro-OMeTAD$^{\bullet+}$.[18,19] Our amide HTMs are thought to be doped by FK209 in a similar fashion.[2] Figure ***5.7*** shows that upon doping, the conductivity of both materials increases sharply, up to three orders of magnitude at 30% FK209 concentration. Th-monoAmideTPA performs slightly better than An-monoAmideTPA, $8.7 \pm 1.61 \times 10^{-6}$ and $6.6 \pm 1.39 \times 10^{-6}$ S/cm respectively, with the conductivities of both materials falling in between those of TPA-BT and EDOT-Amide-TPA at the same doping concentration.[4] At concentrations of 50% FK209 and higher we see a less favourable trade-off as the presence of the oxidant interferes with the conductivity of the material, although the performance remains higher than the pristine HTM. While these materials were initially designed to further investigate the structure-property relationships of our HTMs, the preliminary conductivity results are promising as asymmetric amides appear to be comparatively easier produce in high yield and purity.

5.4.2. UV-visible absorption

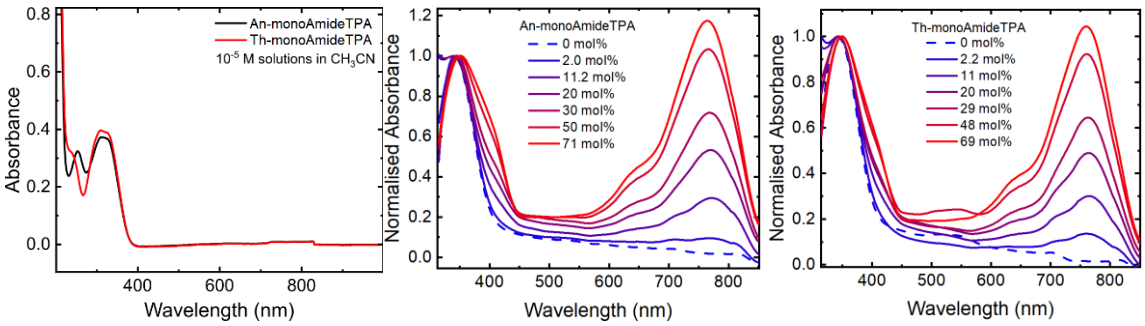

Figure 5.7 UV-Visible absorption spectra (slit width = 2 nm) of our HTMs with different concentrations of the dopant FK209.

Parasitic absorption by the HTM reduces the light harvesting ability of the perovskite layer. Therefore, the UV-vis absorption spectra of 1 x 10^{-5} M HTM solutions in acetonitrile were recorded, to asses their suitability as HTMs. An- and Th-monoAmideTPA have very similar absorption profiles with a peak at around 345nm which drops off rapidly at 400 nm, being transparent in the visible and near-IR region. Upon oxidation with FK209, this first absorption peak broadens and a second peak is observed at around 765 nm with a shoulder at 640 nm which corresponds to the oxidised radical cation species.[19] Of the FK209 doped HTMs, the asymmetric amides and TPA-BT are more transparent than Spiro-

OMeTAD.[2] However, the region with the lowest absorbance is shifted, with An- and Th-monoAmideTPA being fairly transparent between 450-600 nm when doped with ~30% FK209, while FK209 doped TPA-BT is transparent between 350 and 500 nm.[2]

5.4.3. Frontier orbital energies

As discussed in *Chapter 1*, the alignment of HTM energy levels with the perovskite absorber layer is crucial for efficient charge extraction and the avoidance of charge accumulation and recombination at the HTM/perovskite interface. Theoretical frontier orbital energies were obtained from DFT calculations (PBE0/def2-sv(p)).

Table 5.1 Dipole moments and Frontier Orbital energies of synthesised HTMs where E_{HOMO}^{calc} is based on $E_{HOMO}^{DFT,DCM}$ with correction factor (−0.206 eV) applied (see *Chapter 3* section ***3.4.2.***).

Molecule	$E_{HOMO}^{DFT,DCM}$ ***(eV)***	E_{HOMO}^{calc} ***(eV)***	$E_{LUMO}^{DFT,DCM}$ ***(eV)***	***Dipole (D)***
TPA-BT	−5.03	−5.23	−1.34	10.6
Th-monoAmideTPA	−5.07	−5.27	−1.18	5.8
An-monoAmideTPA	−5.05	−5.26	−1.11	6.8
An-monoUreaTPA	−5.01	−5.22	−0.59	6.2

As shown in table ***5.1***, the calculated DFT $E_{HOMO}^{calc}$are fairly consistent across the group. The electrochemical behaviour of An-monoUreaTPA, Th- and An-monoAmideTPA was further investigated using cyclic voltammetry (**Figure *5.9(d)***). We observed reversible oxidations for all three materials starting at 0.065 V versus Ferrocene (Fc) and redox potentials of 0.13±0.01 V vs Fc. The HOMO energies were then estimated using the formal potential of the Fc+/Fc redox positioned at −5.07 eV versus vacuum[5] and found to be -5.20±0.01 eV for all, close to E_{HOMO}^{calc}which range between −5.27 and −5.22 eV. The similarly between the three reflects the structural similarly between the compounds. The HOMO in all three HTMs is mainly localised over the TPA moiety, and the difference in the adjacent resonance stabilised amide and urea linker moieties does not seem to have much of an effect.

The E_{0-0} energy was then determined optically, from the intersection of the normalised UV-visible absorption and fluorescence emission spectra, and E_{LUMO} was estimated from $E_{HOMO} + E_{0-0}$ (**Table 5.2**). We see more of a difference in the E_{LUMO}, ranging between -1.76±0.01 eV for An-monoUreaTPA and -1.49±0.01 eV Th-monoAmideTPA, reflecting the structural differences of the acceptor moiety of the three HTMs. There is far less agreement between $E_{LUMO}^{DFT,DCM}$ and E_{LUMO} as there is between E_{HOMO}^{calc} and E_{HOMO}, and interestingly the order in the energies is reverse between $E_{LUMO}^{DFT,DCM}$ and E_{LUMO}.

Nevertheless, both sets of results show that the LUMOs of all three asymmetric compounds are significantly higher in energy than the conduction band of standard perovskite absorber $MAPbI_3$ (3.9 eV), which would result in good charge blocking in devices. The HOMO energies are suitably aligned with the valence band of the perovskite (5.4 eV) to allow for efficient hole extraction. Therefore, overall the three molecules investigated have Frontier orbital energies that make them suitable as HTMs in standard PSCs.

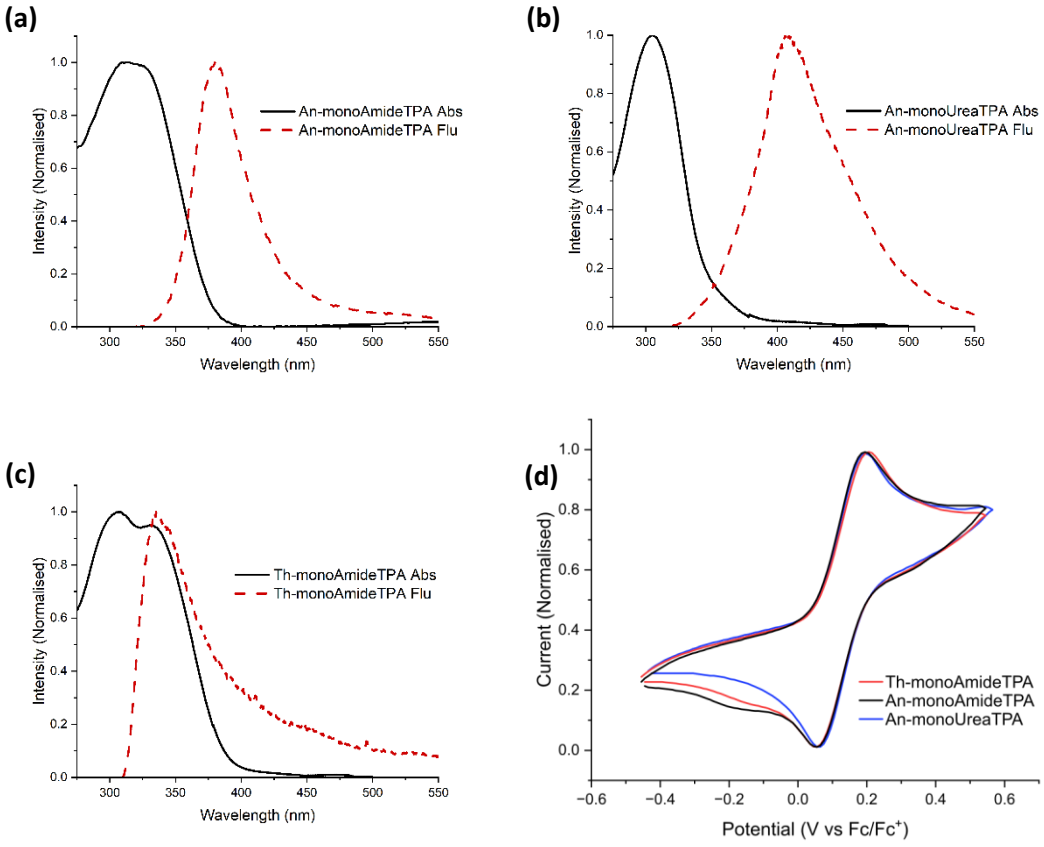

Figure 5.8 **(a-c)** Normalised UV-visible absorption (solid lines) spectra of 3 µM, solutions in anhydrous dichloromethane (slit width = 2 nm). **(a-c)** Normalised fluorescence emission spectra of 5 µM solutions in anhydrous dichloromethane; An-monoAmideTPA $\lambda_{ex} = 309$ nm, An-monoUreaTPA $\lambda_{ex} = 305$ nm, Th-monoAmideTPA $\lambda_{ex} = 290$ nm. **(d)** An-monoUreaTPA, Th- and An-monoAmideTPA normalised cyclic voltammograms of 5mM HTM solutions in anhydrous dichloromethane under N_2 with 0.1 M $TBAPF_6$ as electrolyte, measured at a scan rate of 100 mVs^{-1} against a ferrocene (Fc) external reference.

Table 5.2 Optical and redox properties of Th- and An-monoAmideTPA and An-monoUreaTPA in dichloromethane

Molecule	λ_{abs}^{max} ***(nm)***	λ_{em}^{max} ***(nm)***	E_{0-0} [a] ***(eV)***	$E_{1/2}$ ***(V vs Fc)***	E_{HOMO} [b] ***(eV)***	E_{LUMO} [b] ***(eV)***
Th-monoAmideTPA	307	335	3.71	0.13±0.01	-5.20±0.01	-1.49±0.01
An-monoAmideTPA	309	380	3.52	0.13±0.01	-5.20±0.01	-1.68±0.01
An-monoUreaTPA	305	406	3.44	0.13±0.01	-5.20±0.01	-1.76±0.01

[a] E_{0-0} energy was calculated using the equation $E_{0-0} = 1240/\lambda_{0-0}$, where $\lambda_{0-0}$is the intersection wavelength between the normalised absorption and emission spectra for the lowest energy band. [b]Calculated from -5.07 eV - E_{0-0} [HTM$^+$|HTM] + eV.[5] [c]Estimated from $E_{HOMO} + E_{0-0}$.

5.5 Conclusions

To test the effect of the dipole moment and packing capabilities on charge transport properties of HTMs, a series of simple asymmetric molecules was designed with different H-bonding capabilities, consisting of secondary, tertiary amide and urea linkers. From an initial DFT (PBE0/def2-sv(p)) screening of our molecules we found that the frontier orbital energies suitable for their use as HTMs with PSCs. Additionally, we found the dipole moments of these molecules to be high. As discussed in previous chapters, this may provide an additional driving force for molecules to align antiferroelectrically to one another with respect to the direction of their respective dipole moments.[3] In molecules able to H-bond, this would hopefully result in a higher proportion of strongly bound quenched dipole dimers in solution, prior to deposition. The similar dipole moment strengths across the anisole series would allow us to better investigate the effect of H-bonding, while the asymmetric analogue of TPA-BT, and An-monoAmideTPA allows us to compare the effect of the dipole moment strength. Future work will focus on inverstigating the charge transport and film properties of these and similar materials further. TPA-BT, Th-monoAmideTPA, An-monoAmideTPA and An-monoUreaTPA were successfully synthesised, as confirmed by NMR spectroscopy and mass spectrometry. Preliminary conductivity, UV-vis absorption, fluoresence emissionand cyclic voltammetry (CV) measurements were obtained. UV-vis absorption spectra show that An- and Th-monoAmideTPA are fairly transparent between 450-600 nm when doped with ~30% FK209. Lateral conductivity measurements on pristine and FK209-doped thin films, showed that the conductivity of both materials increases by up to three orders of magnitude upon doping with 30 mol% FK209. Th-monoAmideTPA performs slightly better than An-monoAmideTPA, and the conductivities are comparable to TPA-BT and EDOT-Amide-TPA at the same doping concentrations. The HOMO energies of our molecules, obtained from cyclic voltammetry and DFT calculations, indicate good alignment with the valence

band of $MAPbI_3$ perovskite, suggesting these materials could be suitable HTMs for PSCs. Although initially designed to test structure-property relationships, these promising initial results warrants further exploration of these simple high-yielding materials as HTMs in their own right.

5.6 Experimental details

5.6.1 General information

Room temperature was between 20 and 25 °C. Where anhydrous conditions were used, glassware was previously dried at 120 °C for >16 h.

5.6.2 Chemical reagents and solvents

All chemicals were purchased from commercial sources and used as received, unless otherwise stated. Where specified, anhydrous solvents were used. In all other instances, solvents used were of HPLC grade and acquired from Fischer Scientific. Petroleum ether refers to the petroleum fraction boiling in the range 40-60 °C. Solvents for spectroscopic studies were of the highest purity available.

5.6.3 Chromatography

Thin layer chromatography (TLC) was carried out using silica gel-coated aluminium plates (Kieselgel 60 F254, 0.2 mm) acquired from Merck. Developed TLC plates were visualised using ultraviolet light (254 nm/365 nm) and potassium permanganate stain. Where specified, automated column chromatography was performed on a Biotage® Selekt flash chromatography purification system containing an integrated UV absorption detector. The UV absorption of the eluting fractions was monitored at 254 nm. Biotage® Sfär Silica 60 µm flash chromatography cartridges were used, and crude samples were dry loaded onto silica. Normal phase conditions were used and gradient elutions were performed with the solvent mixtures specified.

5.6.4 Analytical techniques

^{1}H NMR spectra were recorded on Bruker Avance II 400 MHz spectrometers at room temperature. ^{1}H-decoupled ^{13}C NMR spectra were recorded on a Bruker Avance III spectrometer at 75 MHz, and Bruker Avance II spectrometers at 101 MHz, at room temperature. Chemical shifts are listed upfield in parts per million (δ) and residual solvent peaks were used as an internal standard. ^{1}H peak integrations, multiplicities (s = singlet, d = doublet, app d = apparent doublet, dd = doublets of doublets, and m = multiplet), and coupling constants (J, in Hz) are specified where possible.

High resolution atomic mass spectroscopy (HRAM) was performed by the EPSRC UK National Mass Spectrometry Facility (NMSF) at Swansea University. Amides were analysed by standard FTMS using nano-electrospray ionisation(nESI) in positive mode, on ThermoScientific LTQ Orbitrap XL^{TM} mass spectrometer. An-monoUreaTPA was analysed on a Waters Xevo G2-S Q-ToF Mass Spectrometer using atmospheric-pressure chemical ionisation with an atmospheric solids analysis probe (APCI/ASAP).

At Newcastle University, the FT-IR spectrum of TPA-BT was recorded with a PerkinElmer 467 FT-IR Spectrum Two infrared spectrometer. For FT-IR of An-monoUreaTPA, An- and Th-monoAmideTPA, 1 mg of each sample was pulverised with 150 mg of KBr, transferred to KBr die, evacuated, and pressed under vacuum for 60 s at 10 Tonnes on a laboratory press. FT-IR spectra were then recorded with a Bruker Vertex 80 MIR spectrometer, with the aperture set to 6 nm, and corrected against the KBr and air blank.

X-ray crystallography and structure elucidation of TPA-BT was performed by Dr Paul Waddell at Newcastle University. Crystal structure data were collected on a Xcalibur, Atlas, Gemini ultra diffractometer equipped with an fine-focus sealed X-ray tube (λ CuKα = 1.54184 Å). The software package CrysAlisPro (Rigaku OD, 2015) was used for cell refinement, data collection, data reduction and to correct intensities for absorption. Intensities were corrected for absorption via an analytical numeric absorption correction method using a multifaceted crystal model based on expressions derived by R.C. Clark & J.S. Reid.[20] Using Olex2[21], the structure was solved using XT[22] and refined by XL[23].

5.6.5 Optoelectronic experiments

For conductivity measurements, patterned indium-tin oxide substrates (ITO) on glass were prepared for conductivity measurements by etching channels across which the conductivity of our materials could be measured with a Rofin EasyMark IV F20 laser etcher. Two different channel lengths were used for the patterned substrates: a ‘long’ pattern with a length of 157.3 cm for measuring conductivities of pristine samples and those with a low oxidised content, and a ‘short’ pattern with a length of 37.2 cm for measuring more highly oxidised samples. The resistance across the channel was measured for all the blank slides, and any short circuits were discarded. Thin films of our HTMs were deposited onto the patterned substrates from solution spin-coating in an N2 environment. Solutions

of the dopant FK209 in acetonitrile (145.3 mg/mL), and the amides in chlorobenzene (An-monoAmideTPA 14.2 mg/mL; Th-monoAmideTPA 14.9 mg/mL) were prepared. The dopant solution was and added directly to samples of each HTM solution to yield mixtures containing between 0 and 70 mol% of the dopant relative to the HTM. All solutions were handled under a nitrogen atmosphere and filtered before spin-coating onto the patterned substrates. The current-voltage behaviour of our HTMs was measured using a pulsed voltage setup. For conductivity calculations, the film thicknesses were measured using a DekTak XT contact profiler equipped with a 2 µm stylus tip. Three separate valleys were etched into a thin film of each HTM on glass using a metal ruler and a cotton bud wetted with dichloromethane. The film thickness was then measured as the height difference across the etched valley. Three separate measurements across each valley allowed calculation of the film thickness as an average of 9 measurements across each film, as well as the standard deviation.

At the University of Glasgow, the UV-visible absorption spectra were recorded on a Shimadzu UV-3600 UV-Vis-NIR spectrophotometer, using a slit width of 2 nm. The fluorescence emission spectrum of An-monoAmideTPA was carried out using a Shimadzu RF-5301PC spectrofluorometer. At Newcastle University, UV- visible absorption spectra were recorded on a Perkin Elmer 1050+ UV-Vis-NIR spectrophotometer, using a slit width of 2 nm. Fluorescence emission spectra were recorded using a F-4500 Hitachi Fluorescence spectrophotometer, using 5 nm emission bandwidth and a 10 nm excitation bandwidth.

Cyclic voltammetry experiments were performed using a glassy carbon working electrode, a platinum wire counter electrode, against a saturated calomel reference electrode (SCE) ferrocene (Fc) as an external reference. Experiments were performed in anhydrous and degassed dichloromethane 5 mM solutions of the HTM, with 0.5 M tetrabutylammonium hexafluorophosphate ($tBuNPF_6$) as electrolyte, and a scan rate of 100 mV s^{-1}. HOMO levels were calculated as stated in the literature with the formal potential of the Fc^+/Fc redox positioned at −5.07 eV versus vacuum.[5]

5.6.6 Synthesis of HTMs

4,4'-Dimethoxy-4''-nitrotriphenylamine[4]

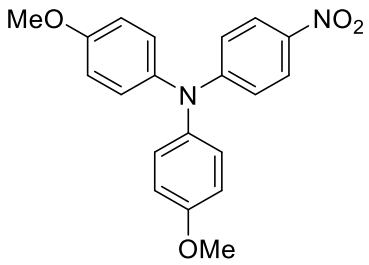

4-Nitroaniline (5.00 g, 36 mmol, 1eq), 4-iodoanisole (17.84 g, 76 mmol, 2.1 eq), copper powder (2.26 g, 36 mmol, 1 eq), potassium carbonate (10.51 g, 76 mmol, 2.1 eq), and 18-crown-6 (0.411 g, 1.6 mmol, 0.4 eq) were dissolved in anhydrous 1,2-dichlorobenzene (20 mL). The reaction mixture was degassed for 15 minutes before stirring vigorously under reflux (180 °C). After 16 hours, the reaction mixture appeared to contain a mixture of products by TLC [R_f = 0.42, 0.24 (30% diethyl ether/petroleum ether)]. Further 4-iodoanisole (17.84 g, 21.6 mmol, 0.6 eq) was added, and the reaction mixture degassed for 15 minutes. The mixture was again stirred vigorously under reflux (180 °C) for further 36 hours. The reaction mixture was cooled to room temperature and filtered. The eluent was partially concentrated *in vacuo* to afford a dark red viscous liquid. Petroleum ether (350 ml) and ethanol (10 ml) was added, and the resulting mixture was sonicated before cooling at −18°C for 4 hours. The resulting precipitate was filtered off and recrystallised from propan-2-ol to afford the title compound (10.64 g, 30 mmol, 84% yield) as dark red crystals. R_f = 0.45 [30% diethyl ether/petroleum ether (v/v)]; ^{1}H NMR ($CDCl_3$, 400MHz) δ: 8.00 (app d, J = 9.4 Hz, 2H), 7.13 (app d, J = 9.0 Hz, 4H), 6.91 (app d, J = 9.0 Hz, 4H), 6.75 (app d, J = 9.4 Hz, 2H), 3.82 (s, 6H) ppm.

4-Amino-4',4''-dimethoxytriphenylamine[4]

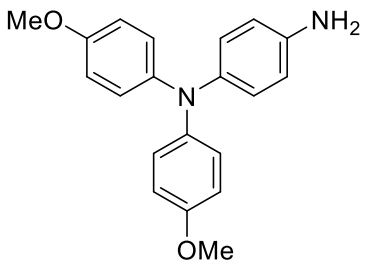

To a solution of 4,4'-dimethoxy-4''-nitrotriphenylamine (700 mg, 2.00 mmol, 1 eq) and 10% palladium on carbon (70 mg, 10% w/w) in anhydrous tetrahydrofuran (15 ml), hydrazine monohydrate (0.68 ml, 14.98 mmol, 7 eq) was added in one portion. The reaction mixture was degassed for 15 minutes, then stirred at reflux (66 °C) with vigorous stirring under an argon atmosphere for 48 hours, until the solution decolourised, and TLC showed complete consumption of the nitro starting material. The reaction mixture was cooled to room temperature and filtered over celite, eluting with ethyl acetate. The eluent was concentrated *in vacuo* to give the title compound (600 mg, 1.87 mmol, 94% crude yield) as a pale lilac crystalline solid. R_f = 0.25 [30% ethyl acetate/petroleum ether (v/v)]; ^{1}H NMR ($CDCl_3$, 400MHz) δ : 6.95 (app d, *J* = 9.0 Hz, 4H), 6.87 (app d, *J* = 8.7 Hz, 2H), 6.76 (app d, *J* = 9.0 Hz, 4H), 6.60 (app d, *J* = 8.7 Hz, 2H), 3.77 (s, 6H) ppm.

Thiophene-3,4-dicarbonyl dichloride[2,5]

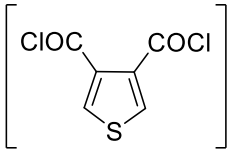

To thiophene-3,4-dicarboxylic acid (2.48 g, 14.43 mmol, 1 eq) in anhydrous tetrahydrofuran (20 ml) was added anhydrous *N*,*N*-dimethylformamide (0.112 ml, 1.44 mmol, 0.1 eq), and the suspension was degassed for 15 minutes. Thionyl chloride (2.42 ml, 33.19 mmol, 2.3 eq) was added dropwise, and the resulting yellow solution was heated under reflux (80 °C) under an argon atmosphere. After 3 hours, the reaction mixture was cooled to room temperature before concentrating *in vacuo* to afford the

title compound (3.02 g crude yield, quant) as a viscous brown liquid. The entire yield was used in the next step without further purification.

N_3,N_4-bis(4-(bis(4-methoxyphenyl)amino)phenyl)thiophene-3,4-dicarboxamide (TPA-BT)[2,5]

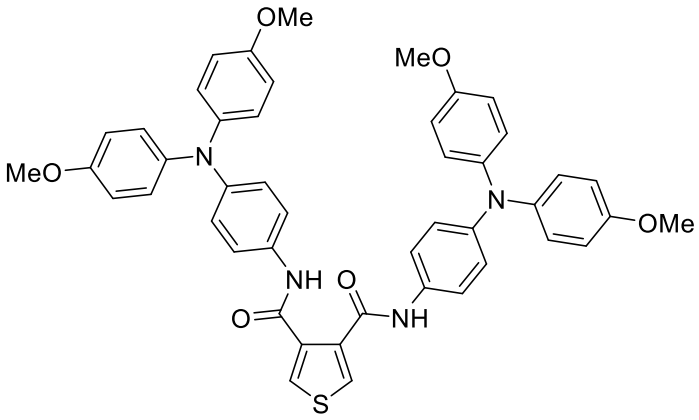

To a solution of thiophene-3,4-dicarbonyl dichloride (3.02 g crude yield) and 4-amino-4',4''-dimethoxytriphenylamine (9.706 g, 30.29 mmol, 2.1 eq) in anhydrous tetrahydrofuran (20 mL), triethylamine (4.62 mL, 33.18 mmol, 2.3 eq) was added dropwise to give a dark red solution which was degassed for 15 minutes. The reaction mixture was heated under reflux (66 °C) for 15 minutes and left stirring at room temperature for 72 hours under an argon atmosphere. An excess of petroleum ether (500 ml) was added, and the resulting yellow-brown suspension cooled at −18°C overnight. The precipitate was filtered before purifying by column chromatography (10% acetone/DCM). The amorphous solid obtained was recrystallised from ethanol to afford the title compound (2.47 g, 3.18 mmol, 22% yield over 2 steps) as a pale yellow crystalline solid. R_f = 0.36 [50% ethyl acetate/petroleum ether (v/v)]; ^{1}H NMR (400 MHz, DMSO-d_6) δ : 10.33 (s, 2H), 7.87 (s, 2H), 7.56 (d, J = 8.9 Hz, 4H), 7.04 (m, 8H), 6.96 (d, J = 8.9 Hz, 4H), 6.82 (m, 8H), 3.80 (s, 12H) ppm; ^{13}C NMR (101 MHz, DMSO-d_6) δ : 162.63, 155.81, 145.85, 141.27, 135.77, 132.60, 131.38, 126.24, 121.83, 121.59, 114.83, 55.66 ppm; FTIR: v(cm^{-1}): 3238, 3100, 3039, 2948, 2834. 1608, 1557, 1538, 1501, 1463, 1441, 1429, 1368, 1310, 1284, 1240, 1188, 1178, 1104, 1035, 943, 911, 892, 569, 824, 782, 728, 679, 639, 617, 572, 525, 479; FTMS (nESI$^+$) *m/z*: found = 777.2747 [M-H]$^+$, calculated for $C_{46}H_{41}N_4O_6S$: 777.2741; Melting point 232 – 234 °C.

N-(4-(bis(4-methoxyphenyl)amino)phenyl)thiophene-3-carboxamide (Th-monoAmideTPA)

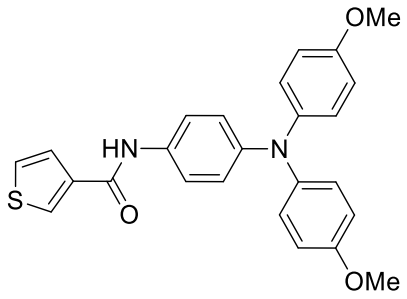

To a stirred solution of 4-amine-4',4''-dimethoxytriphenylamine (0.913 g crude yield, 2.85 mmol, 1 eq) in 40 ml of anhydrous tetrahydrofuran at 0 °C under a nitrogen atmosphere, was added thiophene-3-carbonyl chloride (0.823 g, 5.61 mmol, 2 eq) in 25 ml of anhydrous tetrahydrofuran dropwise over 5 minutes. The reaction mixture was then stirred for a further 5 minutes to give an orange solution, before triethylamine (0.253 g, 2.50 mmol, 0.9 eq) was added and a pale precipitate formed. The reaction mixture was stirred at room temperature for 72 hours. The reaction mixture was quenched with brine (100 ml), the phases separated, and the aqueous layer extracted with ethyl acetate (3 × 100 ml). The combined organic extracts were dried over magnesium sulfate, filtered, and concentrated *in vacuo* to give a turquoise semi-solid. The crude product was purified by Biotage® Selekt flash column chromatography (0-100% ethyl acetate/petroleum ether). Product fractions were concentrated *in vacuo*, redissolved in dichloromethane (100 ml) and washed with saturated aqueous bicarbonate (50 ml) and brine (50 ml). The organic phase was dried over sodium sulfate, filtered and concentrated *in vacuo* to give the title compound (1.112 g, 2.58 mmol, 91% yield) as a pale yellow foamy semi-solid. R_f = 0.29 [30% ethyl acetate/petroleum ether (v/v)]; ^{1}H NMR (400 MHz, DMSO-d6) *δ* 9.93 (s, 1H), 8.30 (dd, *J* = 2.8, 1.5 Hz, 1H), 7.65-7.61 (m, 2H), 7.58 (dd, *J* = 6.9, 2.1 Hz, 2H), 6.96 (dd, *J* = 6.2, 2.2 Hz, 4H), 6.88 (dd, *J* = 6.6, 2.5 Hz, 4H), 6.83 (dd, *J* = 6.9, 2.1 Hz, 2H), 3.73 (s, 6H) ppm; ^{13}C NMR (75 MHz, DMSO-d6) *δ*: 160.48, 155.17, 144.18, 140.72, 137.94, 132.56, 129.31, 127.14, 126.81, 125.58, 121.55, 121.27, 114.85, 55.22, 40.36, 40.08, 39.80, 39.52, 39.24, 38.97, 38.69 ppm; FTIR: ν(cm^{-1}): 3288, 3100, 3038, 2996, 2930, 2904, 2832, 1640, 1598, 1504, 1412, 1311, 1240, 1178, 1104, 1034, 914, 866, 826, 779, 739, 653, 575, 521, 416; FTMS (nESI$^+$) *m/z* (relative intensity): found = 431.1427 [M-H]$^+$, calculated for $C_{25}H_{23}N_2O_3S$: 431.1424; 431.1 [M-H]$^+$ (100), 432.1 [M-H]$^+$ (29), 861.3 [2M-H]$^+$ (25), 862.3 [2M-H]$^+$ (14.5), 453.1 [M-Na]$^+$ (12), 260.1 (11), 304.2 (8), 465.1 [M-Cl]$^+$ (6), 883.3 [2M-Na]$^+$ (5), 690.3 (4), 433.1 [M-H]$^+$ (4), 863.3 [2M-H]$^+$ (3), 199.1 (3).

N-(4-(bis(4-methoxyphenyl)amino)phenyl)-4-methoxybenzamide (An-monoAmideTPA)

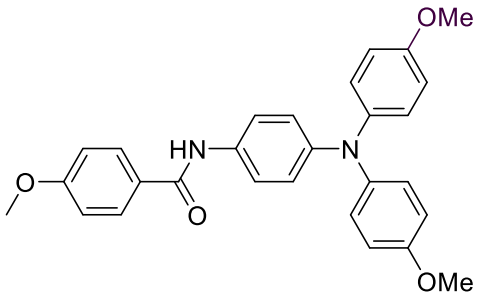

To a stirred solution of 4-amine-4',4''-dimethoxytriphenylamine (0.799 g crude yield, 2.28 mmol, 1 eq) in 30 ml of anhydrous tetrahydrofuran at 0 °C under a nitrogen atmosphere, was added 4-methoxybenzoyl chloride (0.972 g, 5.70 mmol, 2.5 eq) in 10 ml of anhydrous tetrahydrofuran dropwise over 5 minutes. The reaction mixture was then stirred for a further 5 minutes before triethylamine (0.254 g, 2.50 mmol, 1.1 eq) was added and a pale precipitate formed. The reaction mixture was stirred at room temperature 8 for days. The reaction mixture was a pale blue suspension after 16 hours, before changing colour to a pale-yellow suspension. The reaction mixture was quenched with brine (100 ml) and saturated aqueous sodium bicarbonate (100 ml). The phases were separated, and the aqueous layer extracted with ethyl acetate (3 × 50 ml). The combined organic extracts were dried over magnesium sulfate, filtered, and concentrated *in vacuo* to give a deep green foamy semi-solid. The crude product was purified by Biotage® Selekt flash column chromatography (0-100% ethyl acetate/petroleum ether; 0-50% methanol/ethyl acetate). Product fractions were concentrated *in vacuo*, redissolved in dichloromethane (100 ml) and washed with saturated aqueous bicarbonate (50 ml) and brine (50 ml). The organic phase was dried over sodium sulfate, filtered and concentrated *in vacuo* to give the title compound (0.906 mg, 1.99 mmol, 87% yield) as a pale brown semi-solid. R_f = 0.40 [35% ethyl acetate/petroleum ether (v/v)]; ^{1}H NMR (400 MHz, DMSO-d6) δ: 10.01 (m, 1H), 7.95 (d, J = 8.8 Hz, 2H), 7.61 (d, J = 9.0 Hz, 2H), 7.04 (d, J = 8.9 Hz, 2H), 6.99-6.93 (m, 4H), 6.92-6.82 (m, 6H), 3.83 (s, 3H), 3.72 (s, 6H) ppm; ^{13}C NMR (75 MHz, DMSO-d6) δ: 164.48, 161.78, 155.12, 144.03, 140.80, 133.06, 129.49, 127.06, 125.50, 121.61, 121.43, 114.85, 113.55, 55.42, 55.23 ppm; FTIR: ν(cm^{-1}): 3284, 3041, 3000, 2933, 2835, 2045, 1898, 1645, 1607, 1504, 1462, 1406, 1312, 1239, 1177, 1104, 1032, 903, 825, 762, 717, 682, 629, 609, 574, 518, 419; FTMS (nESI$^+$) *m/z* (relative intensity): found = 455.1970 [M-H]$^+$, calculated for $C_{28}H_{27}O_4N_2$: 455.1965; 455.2 [M-H]$^+$ (100), 456.2 [M-H]$^+$ (30), 909.4 [2M-H]$^+$ (20), 910.4 [2M-H]$^+$ (12), 489.2 [M-Cl]$^+$ (11), 477.2 [M-Na]$^+$ (10), 304.2 (6), 456.2 [M-H]$^+$ (4), 911.4 [2M-H]$^+$ (3), 943.3472 (3), 523.1 (2), 714.3 (2), 931.3681 [2M-Na]$^+$ (1).

1-(4-(bis(4-methoxyphenyl)amino)phenyl)-3-(4-methoxyphenyl)urea (An-monoUreaTPA)

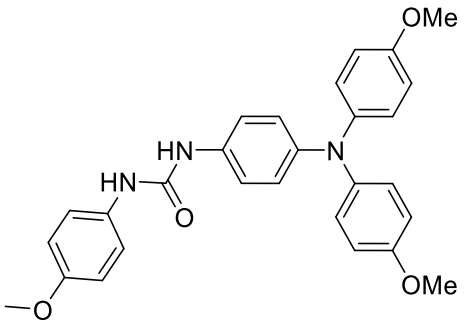

To a stirred solution of 4-amine-4',4''-dimethoxytriphenylamine (0.600 g crude yield, 1.87 mmol, 1 eq) in 15 ml of anhydrous toluene at 0 °C under a nitrogen atmosphere, was added 4-methoxyphenyl isocyanate (0.307 g, 2.1 mmol, 1.1 eq) in 5 ml of anhydrous toluene. The reaction mixture turned cloudy after 30 minutes and was kept stirring under a nitrogen atmosphere for 72 hours. The precipitate was filtered off to give the title compound to afford the title compound (679 g, 1.45 mmol, 77% yield) as a pale grey solid. R_f = 0.46 [50% ethyl acetate/petroleum ether (v/v)]; ^{1}H NMR (400 MHz, DMSO-d6) *δ*: 8.43 (s, 1H), 8.38 (s, 1H), 7.34 (d, *J* = 8.9 Hz, 2H), 7.30 (d, *J* = 9.0 Hz, 2H), 6.92-6.80 (m, 12H), 3.72 (s, 6H), 3.71 (s, 3H) ppm; ^{13}C NMR (75 MHz, DMSO-d6) *δ*: 154.83, 154.34, 152.78, 142.53, 141.06, 134.06, 132.86, 124.95, 122.71, 119.85, 119.55, 114.76, 113.96, 55.15, 55.21 ppm; FTIR: ν(cm^{-1}): 3368, 3314, 3041, 3003, 2955, 2908, 2834, 2055, 1874, 1663, 1601, 1547, 1503, 1466, 1440, 1412, 1300, 1284, 1243, 1171, 1103, 1033, 915, 828, 782, 753, 726, 651, 596, 578, 523; TOF MS (ASAP+) *m/z* (relative intensity): found = 470.2079 $[M-H]^+$, calculated for $C_{28}H_{28}O_4N_3$: 470.2080; 321.2 (100), 347.1 (35), 322.2 (28), 470.2 $[M-H]^+$ (15), 124.1 (8), 471.2 $[M-H]^+$ (5), 535.5 (5), 369.4 (5), 535.5 $[M-2Na]^{2+}$ (4), 213.1 (2).

References

1. T. Pope, Y. Giret, M. Fsadni, P. Docampo, C. Groves and T. Penfold, *Org. Electron.*, 2023, **115**, 106760.
2. B. Vella, M. Fsadni, T. Pope, M. Giza, F. J. Angus, I. Shmarov, P. L. Lalaguna, M. Cariello, C. Wilson, M. Kadodwala, T. J. Penfold, P. Docampo and G. Cooke, *J. Mater. Chem. A*, 2024 (*accepted*).
3. F. Wuerhtner, *Acc. Chem. Res.*, 2016, **49**, 868−876; 15. F. Würthner and K. Meerholz, *Chem. - Eur. J.*, 2010, **16**, 9366−9373.
4. M. L. Petrus, T. Bein, T. J. Dingemans, and P. Docampo, *J. Mater. Chem. A*, 2015, **3**, 12159; M. L. Petrus, A. Music, A. C. Closs, J. C. Bijleveld, M. T. Sirtl, Y. Hu, T. J. Dingemans, T. Bein and P. Docampo, *J. Mater. Chem. A*, 2017, **5**, 25200.
5. E. Alkhudhayr, D. Sirbu, M. Fsadni, B. Vella, B. Muhammad, P. Waddell, M. R. Probert, Michael T. J. Penfold, T. Hallam, E. Gibson and P. Docampo, *ACS Appl. Energy Mater.*, 2023, **6**, 11573−11582.
6. G.-W. Kim, H. Choi, M. Kim, J. Lee, S. Y. Son and T. Park, *Adv. Energy Mater.*, 2020, **10**, 1903403.
7. C.-G. Zhan, J. A. Nichols and D. A. Dixon, *J. Phys. Chem. A*, 2003, **107**, 4184.
8. J. Salunke, X. Guo,. Lin, J. R. Vale, N. R. Candeias, M. Nyman, S. Dahlström, R. Österbacka, A. Priimagi, J. Chang and P. Vivo, *ACS Appl. Energy Mater.*, 2019, **2**, 3021
9. B. Xu, E. Sheibani, P. Liu, J. Zhang, H. Tian, N. Vlachopoulos, G. Boschloo, L. Kloo, A. Hagfeldt and L. Sun, *Adv. Mater.*, 2014, **26**, 6629.
10. H. Liu, B. He, H. Lu, R. Tang, F. Wu, C. Zhong, S. Li, J. Wang and L. Zhu, *Sustain. Energy Fuels*, 2022, **6**, 371.
11. N. Arora, C. Wetzel, M. Ibrahim Dar, A. Mishra, P. Yadav, C. Steck, S. M. Zakeeruddin, P. Bäuerle and M. Grätzel, *ACS Applied Materials & Interfaces*, 2017, **9**, 44423.
12. F. Neese, *Wiley Interdiscip. Rev. Comput. Mol. Sci.*, 2012, **2**, 73; F. Neese, *Wiley Interdiscip. Rev. Comput. Mol. Sci.*, 2018, **8**, e1327.
13. J. P. Perdew,K. Burke and M. Ernzerhof, *Phys. Rev. Lett.*, 1996, **77**, 3865; C. Adamo and V. Barone, *J. Chem. Phys.*, 1999, **110**, 6158; 24. F. Weigend and R. Ahlrichs, *Phys. Chem. Chem. Phys.*, 2005, **7**, 3297.
14. A. Banerjee, T. Hattori and H. Yamamoto, *Synthesis*, 2023, **55**, 315.
15. E. Joyce, P. Kavanagh, D. Leech, J. Karpinska, P. McArdle, F. Aldabbagh, *Tetrahedron Lett*., 2012, **53**, 3788 – 3791.
16. C.-W. Chang, G.-S. Liou, *J. Mater. Chem.*, 2008, **18**, 5638 – 5646

17. S. M. Graham and L. M. Ohrtman, *J. Heterocycl. Chem.*, 1998, **35**, 887.
18. W. Zhang, F. Zhang, B. Xu, Y. Li, L. Wang, B. Zhang, Y. Guo, J. M. Gardner, L. Sun and L. Kloo, *ACS Appl. Mater. Interfaces*, 2020, **12**, 33751–33758.
19. J. Burschka, F. Kessler, M. K. Nazeeruddin, M. Graetzel, *Chem. Mater.*, 2013, **25**, 2986–2990.
20. R. C. Clark and J. S. Reid, *Acta Crystallogr.*, 1995, A**51**, 887−897.
21. O. V. Dolomanov, L. J. Bourhis, R. J. Gildea, J. A. K. Howard and H. Puschmann, *J. Appl. Crystallogr.*, 2009, **42**, 339-341.
22. G. M. Sheldrick, *Acta Crystallogr.*, 2008, A**64**, 112-122.
23. G. M. Sheldrick, *Acta Crystallogr.*, 2015, A**71**, 3-8.

6 Conclusions and Outlook

6.1. Summary

In this thesis I combined theoretical and experimental work to rationalise the structure-property relationships of amorphous organic small molecule HTMs, particularly those with high dipole moments and high mobilities. The aim was to establish whether trends in key theoretical parameters could be used as a screening tool for to aid the design of novel HTMs with improved charge transport properties.

Key Marcus rate hopping parameters, including the reorganisation energy, electronic coupling and dipole moment were found for a group of amide-, hydrazone-, and azomenthine-linker TPA-based amorphous small molecule organic HTMs. Results from QM calculations show that while it is difficult to predict experimental mobilities from single molecule properties alone, our best performing HTMs also have high dipole moments. This is rather surprising since the energetic noise width scales with the dipole moment strength, quenching mobility for larger dipole moments. An in-house kinetic Monte Carlo algorithm, CharTED-KMC, was used to probe the effect of the dipole and dipole ordering on the hole mobility of representative systems. While increasing the dipole moment strength does indeed quench the mobility in fully disordered systems, this effect is reduced somewhat when the ordering of dipoles is increased. In addition, at higher dipole moment charges travel through the system via energetically favourable routes suggesting that local interactions play an important role. It is possible that high dipoles, in conjunction with other intermolecular interactions like H-bonding, create a driving force for the ordering of molecules in solution and during film formation, resulting in a higher proportion of favourable dipole-dipole interactions between sites. While overall less of the system is energetically accessible to charge hopping than in a fully ordered system, favourable site interactions in high dipole materials could provide energetically efficient routes for charge transport, akin to fibril networks, offsetting the overall increased energetic disorder in the material due to the dipole moment strength.

To understand the effect of the environment and intermolecular interactions, like H-bonding, on charge hopping further MD and kMC simulations were performed. MD simulations of representative

thin films found no significant relationship between the distribution width of HOMO energies and dipole moment strength, and experimental mobilities. The crystal structures of secondary and tertiary amide HTMs reveal differences in packing due to H-bonding, with EDOT-Amide-TPA forming strands of antiparallel oriented monomers. While these materials are described as amorphous, this is because they do not show any long-range order using conventional measuring techniques. Nevertheless, these materials could still have some short-range order, including dimers at the most basic level. A high proportion of antiparallel dimers would result quenched dipole sites that could provide favourable pathways for hole transport by reducing the energetic disorder on a local level.[1] Dimers arranged in this way were found to have a quenched dipole moment. Dipole-quenched H-bonded dimers in EDOT-Amide-TPA were found to have a high binding energy. By contrast, in the methylated analogue DEDOT-Amide-TPA, which is unable to H-bond, the binding energy of dipole-quenched dimers is much smaller. This would suggest that the proportion of dipole quenched dimers relative to other pairs might be higher in EDOT-Amide-TPA than DEDOT-Amide-TPA which could explain its higher charge transport properties. Indeed, MD show that double the number of dimers form over the timescales of the simulations. kMC simulations were performed for fully disordered high dipole systems with a range of quenched-dipole dimer populations. We find that although the overall mobility remained quite low, increasing the dimer population enhances the mobility. Therefore, quenched-dimer formation together with some level of global ordering of dipole moments may explain the larger than expected mobilities of high dipole amorphous HTMs like EDOT-Amide-TPA.

Therefore, high dipole molecules that contain sites for intermolecular hydrogen bonding give rise to amorphous films with higher than expected levels of global and local ordering, resulting in improved hole mobilities. This can be exploited to increase the range of tuneable and easy to synthesise molecules we can explore for HTM applications.

In Chapter 5 we present a series of simple high dipole asymmetric molecules with different H-bonding capabilities, consisting of secondary, tertiary amide and urea linkers. These were designed to aid investigations into the effect of the dipole moment and H-bonding on mobility. The theoretical frontier orbital energies suggest that these would be suitable for use within PSCs. Part of the series, TPA-BT, Th-monoAmideTPA, An-monoAmideTPA and An-monoUreaTPA, was successfully synthesised. Preliminary optoelectronic properties obtained for both Th- and An-monoAmideTPA were found to be promising and we hope to explore these and other simple high-yielding materials further in future work.

6.2. Outlook and Future Work

The computational methods used have limitations, primarily due to the simplifications made with the intention of facilitating rapid molecular screening. In density functional theory (DFT) calculations, relaxed single-molecule geometries were used to extract hopping parameters. However, these geometries may fail to represent the range of constrained conformations and relative orientations of molecules present in their amorphous thin films. A more accurate approach would involve sampling a range of molecules and dimers from the film, which could be obtained from molecular dynamics (MD) simulations, although doing so would significantly increase computational demands. Additionally, the presence of solvent and dopant molecules may have a significant effect. The conductor-like polarizable continuum model, CPCM, gives an approximation of the environment by surrounding molecules with a uniform dielectric medium characterized by its permittivity (dielectric constant). While still lacking explicit detail of the molecule's film environment, tailoring the dielectric constant to individual molecules would improve precision. Using a more advanced basis set, such as def2-TZVP instead of def2-sv(p), and accounting for basis set superposition error (BSSE) would further enhance the accuracy of calculations. Classical MD simulations used to model the amorphous film were performed over a very short timescale, 0.1 ns overall using a timestep of 0.01 fs and 11.4 million simulation steps, and with a small box of between 200 and 500 molecules. The simulation falls well short of the tens of seconds timescale for solution processing procedures, like spin coating. Temperature cycling was used to sample more of the conformational space over the simulation run time, although it is unclear whether this is sufficient to make up for the time difference between the real and simulated process. The short timescale also limits the accuracy of the simulation by failing to sample slow processes, like diffusion. On the other hand, increasing the simulation run time and the system size increases the computational cost reducing its appropriateness as a screening tool. The presence of solvent molecules, used for solution processing of thin films was also not accounted for. The accuracy of MD is also dependent on the inputs, assumptions and simulation conditions used. Algorithms for temperature and pressure control may introduce artifacts if not applied correctly, and errors in assumptions like cutoff distances for van der Waals interactions could lead to inaccuracies. The approach also neglects the effects of domain structures within the film and the specific environment at the film interface, both of which can influence film formation and charge transport behaviour. Ab initio MD simulations had similar limitations, including short runtimes of 5 ps and environmental effects, including the presence of solvents. Kinetic Monte Carlo (kMC) simulations are suitable for modelling rare events like hopping transport, but rely on accurate inputs, and the choice of an appropriate of rate equation. Without suitable inputs from experimental or ab initio data, the

simulations lose validity. Lattice-based models, such as the one used in our studies, may also oversimplify spatial effects and fail to capture the complexity of real systems in which site properties may vary significantly and interdependently. Finally, relatively short timescales and small systems were sampled. However, scaling kMC to large systems or long timescales rapidly increases the computational cost. Rather than starting with simplified property screening at the outset, multiscale modelling on a small group of representative molecules could help narrow down the properties to screen for that would have the greatest impact on charge transport. MD simulations could be used to model film formation, using coarse-grained (CG) methods to account for processes such as solvent evaporation and processing conditions, like temperature and solvent additives. Backmapping could be used to restore atomistic detail, quantum mechanical calculations on samples of molecules could be used to generate a range of molecular properties from the simulated films which could also be used as inputs for kMC simulations to predict mobility. Although this approach is more computationally expensive it would improve both the accuracy and predictive power of theoretical studies, which could be validated experimentally.

As discussed above, relaxed single molecule properties obtained by DFT have limited applicability to the actual trends in properties for conformationally restricted molecules in thin films. For instance, dihedral rotations have a large impact on HOMO energies which may lead to an over or underestimation of the size and distribution width of the uncorrelated energetic disorder within a material. The degrees of freedom of molecules in a thin film and intermolecular interactions, also have an impact on other key hopping parameters like the correlated disorder, which may obfuscate structure-property trends. This also becomes problematic, when the results of simple single molecule property calculations are used as simulation inputs. Therefore, it is difficult to generate significant trends that give us more information that what is already provided by the rate equation used. However, obtaining accurate mobilities that could be used for screening novel compounds is computationally demanding. In our kMC studies, the effect of the various hopping parameters was probed by keeping other variables, like the lattice parameter, fixed. However, parameters and their distribution in the system are highly interlinked. For example, in systems with high dipoles and high ordering, the overall distances and coupling strengths between sites with favourable and unfavourable dipole-dipole interactions is expected to be different, even though molecules are locked into their position in the solid. The assignment of site properties becomes even more complicated when other intermolecular interactions, like H-bonding, are considered. Nevertheless, we were able to get a better understanding of the significance of dipole ordering on the mobility of high dipole systems. Similarly, it may be useful to tune other site and system properties more carefully to reflect the interplay of the various hopping parameters, to gain further insights into structure-property trends.

The crystal structures of our molecules gave insight into the thermodynamically stable orientation of molecules. The degree of crystallinity in our amorphous films could be investigated by using new techniques in X-ray diffractometry.[2] Advanced X-ray powder diffractometry used for analysing pharmaceutical systems, such as coupling X-ray total scattering with the pair distribution function, may be used to study the local structure of materials and probe short- and medium-range order that may be present in samples of the deposited amorphous and disordered films.[2] From ^{1}H NMR studies it appears that our amide HTMs interact by intermolecular H-bonding when in concentrated solutions, such as those used for solution processing.[3] and further insights could be gained from 2D NMR and isothermal titration calorimetry (ITC) experiments. To probe the formation of dimers in these compounds, solvent-dependent titration and dilution experiments using UV-visible absorption and NMR spectroscopy could be carried out. These would help to understand aggregation behaviour, comparing results from increasing the concentration of HTM solutions with the with dissolution of possible aggregates present in deposited film. Aggregation is expected to result in a shift in the UV-visible absorption band, with hypsochromic shifts consistent with the formation of H-aggregates. The solubilities of these higher dipole materials in different solvents could also give important insights, with high solubilities in low polarity solvents suggesting the formation of dipole quenched aggregates.[5] MD binding energies were obtained by increasing the distance between molecular pairs, however, computing the trajectory of monomers forming a dimer would be more representative and may give better insights into the conformations of kinetically controlled dimers. Additionally, basis set superposition error was not accounted for in the calculations and, therefore, results may be inaccurate. It is interesting that in our kMC experiments even low 0 D dimer populations increased the mobility of high dipole disordered systems. We know that uncontrolled aggregate formation and crystallisation in materials negatively affect charge transport properties, both due to the affect the contact between the perovskite layer and the HTM but also because these ordered regions act as energy trap states.[4] On the other hand, controlled aggregates may have similar benefits to polymeric HTMs. It would be interesting to understand the point at which increased order, in the form of higher dimer densities, or trimers, oligomers and larger ordered domains, results in a quenching of mobility in these high dipole systems.

To explore the relationship between the dipole moment strength, H-bonding ability and mobility, work will be carried out to complete the synthesis and characterisation of the HTM series presented in *Chapter 5*. This includes measuring the mobilities and conductivities of thin films of the pristine and doped HTMs prepared by solution spin coating, for comparison with EDOT-Amide-TPA and DEDOT-Amide-TPA. Mobilities are to be measured in the space-charge limited current domain in a FTO/HTM/Ag sandwich, while conductivity measurements are to be carried out on the HTMs

deposited onto patterned ITO substrates. Dopants studies FK209 or LiTFSI, would give further insights. Both electrons and ions may contribute to the total conductivity at room temperature, while at low temperatures ions are frozen and electron motion dominates.[6] Therefore, temperature-dependent conductivity measurements of the doped films, would help elucidate the contribution of ionic motion to the conductivity over a range of temperatures, as well as the activation energy for ionic motion. Crystal structure data, film morphologies and NMR experiments would give insight into the packing of molecules, which could be compared against charge their transport properties.

While the series was designed to probe structure-property relationships, their potential as HTMs for PSCs could be explored further. The high polarity of these materials might provide an additional advantage through enhanced interactions with the perovskite layer. Furthermore, this property offers the possible induction of giant surface potentials (GSP) through the preferential orientation of molecules during film formation, an effect which has been exploited successfully in organic electronics.[7] The low molecular weights of the molecules in the series may result in low thermal stability of their PSCs. However, the methoxy groups on the 4',4''-dimethoxytriphenylamine (TPA) donor unit could be easily modified with long alkoxy chains to prevent excessive aggregation.[8]

References

1. M. A. Baldo, Z. G. Soos and S. R. Forrest, *Chem. Phys. Lett.*, 2001, **347**, 297.
2. S. Thakral, M. W. Terban, N. K. Thakral, R. Suryanarayanan, *Adv. Drug Deliv. Rev.*, 2016, **100**, 183.
3. B. Vella, M. Fsadni, T. Pope, M. Giza, F. J. Angus, I. Shmarov, P. L. Lalaguna, M. Cariello, C. Wilson, M. Kadodwala, T. J. Penfold, P. Docampo and G. Cooke, *J. Mater. Chem. A*, 2024 (*accepted*).
4. T. Malinauskas, D. Tomkute-Luksiene, R. Sens, M. Daskeviciene, R. Send, H. Wonneberger, V. Jankauskas, I. Bruder and V. Getautis, *ACS Appl. Mater. Interfaces*, 2015, **7**, 11107.
5. F. Wuerthner, *Acc. Chem. Res.*, 2016, **49**, 868−876.
6. J. Cao, S. X. Tao, P.A. Bobbert, C.-P. Wong and N. Zhao, *Adv. Mater.*, 2018, **30**, 1707350.
7. E. Ito, Y. Washizu, N. Hayashi, H. Ishii, N. Matsuie, K. Tsuboi, Y. Ouchi, Y. Harima, K. Yamashita and K. Seki, *J. Appl. Phys.*, 2002, **92**, 7306.
8. N. Arora, C. Wetzel, M. Ibrahim Dar, A. Mishra, P. Yadav, C. Steck, S. M. Zakeeruddin, P. Bäuerle and M. Grätzel, *ACS Appl. Mater. Interfaces,* 2017, **9**, 44423.